To the Graduate Council:

I am submitting herewith a thesis written by Bradley James McKeage entitled "Experimental Study of a New Screen for Turbulence Attenuation at Higher Reynold Numbers". I have examined the final copy of this thesis for form and content and recommend that it be accepted in partial fulfillment of the requirements for the degree of Master of Science, with a major in Aerospace Engineering.

A. Vakili, Major Professor

We have read this thesis and
recommend its acceptance:

Accepted for the Council:

Associate Vice Chancellor and
Dean of the Graduate School

EXPERIMENTAL STUDY OF A NEW SCREEN FOR TURBULENCE ATTENUATION AT HIGHER REYNOLD NUMBERS

A Thesis Presented for the

Master of Science

Degree

The University of Tennessee, Knoxville

Bradley James McKeage

May 1997

ACKNOWLEDGEMENTS

I gratefully acknowledge the love and dedicated support always provided by my family. I particularly thank my wife, Cheri, and sons, Kevin and Mitchell, who give me the strength and motivation to achieve.

I must also pay tribute to the entire UTSI staff, who's support and guidance have been instrumental in my post graduate successes. I am especially thankful to Dr. Vakili, my advisor, for his unrivaled enthusiasm, considerable experience, unquestionable knowledge and dedicated tutelage which he so effortlessly and sincerely extended. The special efforts contributed by Dr. Lo and Dr. Wu as committee members for my thesis are also greatly appreciated. Special mention goes to Ricky Meeker, who's technical excellence and engineering practicality ultimately made this research achievable. Jim Goodman's support was also invaluable.

"Per Ardua Ad Astra"

DEDICATION

With sincere honor and love I dedicate this effort to the memory of my greatest supporter and mentor - my father.

ABSTRACT

The purpose of this research effort was to perform a preliminary investigation into the nature of the flow field generated by a cylindrical rod screen model, modified with a helical wrap, in a steady , axial cross flow. Testing was conducted in a buildup in test model complexity starting with single rods, then with single grid test articles (75% porosity) and finally with single screens (56% porosity). Identical models without the helical wrap modification were used to provide the baseline downstream flow fields for direct comparison purposes. First flow visualization using a laser/dye technique was conducted to better understand the complicated flow structure behind the baseline and modified test articles. Initially, the screen's primary component (ie. single cylindrical rod) was evaluated using various helical wrap patterns in an attempt to optimize the wrap design for turbulence reduction manipulation. Minimized coherent structure in the shedding vortices behind the cylinders was the optimization criteria dictating the final wrap selection. The 1 inch helical wrap (double) was ultimately selected based on the flow visualization results. Next the single wrap modification was evaluated with the single grid configuration at a Reynolds number of 500. The downstream flow fields were then characterized at three axial locations (20, 100 and 192 rod diameters) downstream of the baseline and modified single screens. Axial and lateral flow velocities were measured using a single component hot film anemometer at two distinct Reynold numbers (75 and 600). Statistical analysis of the gathered axial velocities, turbulence intensities and velocity dynamics (frequency spectra) was used to formulate a direct preliminary comparison between the test models at these flow conditions. Qualitative results from the flow visualization showed dramatic reductions in the organized flow structure and coherence behind the modified test articles. The quantitative results, however, were less definitive and not as conclusive. Low Reynolds number (75) data were invalidated due to unmanageable temperature gradients in the water tunnel created by severe environmental temperature fluctuations during testing. The high Reynolds number (600) data revealed the same general trends observed during single grid testing, however these trends were less pronounced. The non-uniform nature of the hand

modified test articles and the associated flow field impacts were unknown and potentially significant. Non-the-less, repeatable trends supporting the flow visualization were documented. As a result, a basis for future follow-on research has been established by demonstrating potential reductions in organized flow structures and coherence behind screens using this helical wrap modification.

TABLE OF CONTENTS

CHAPTER		PAGE
1.	INTRODUCTION	1
2.	BACKGROUND AND THEORETICAL CONSIDERATIONS	3
	Literature Review and Theoretical Considerations	3
3.	FLOW VISUALIZATION TESTS	9
	Experimental Objectives	9
	Experimental Set-up and Method	9
	Flow Visualization Study - Results and Discussion	18
4.	FLOWFIELD MEASUREMENT TESTS	25
	Experimental Objectives	25
	Experimental Set-up and Method	25
	Flow Measurement Study - Results and Discussion	33
5.	CONCLUSIONS AND RECOMMENDATIONS	52
LIST OF REFERENCES		55
APPENDICES		59
	APPENDIX A: Hot Film Calibrations	60
	APPENDIX B: Water Tunnel Calibration	68
	APPENDIX C: Single Grid Results	70
	APPENDIX D: Single Screen Results	80
VITA		120

LIST OF FIGURES

FIGURE		PAGE
2-1.	Cylindrical Rod Splitter Plates	5
3-1.	Baseline (top) and Modified (bottom) Single Rods	10
3-2.	Single (Top) and Double (Bottom) Helical Wrap Pattern	10
3-3.	Single Grids (Baseline and 1 inch Single wrap)	11
3-4.	Baseline (Top) and Modified (Bottom) Screens	12
3-5.	UTSI Water Tunnel	13
3-6.	UTSI Water Tunnel Layout Schematic	13
3-7.	Water Tunnel 4 Watt Argon Ion Laser Set-up	14
3-8.	Flow Visualization Setup Schematic	15
3-9.	Dye Probe Design	16
3-10.	Dye Injection Locations on Single Grids and Screens with upstream view orientation	17
3-11.	Baseline Single Rod Side View	19
3-12.	Single Rod 1" Single Wrap Side View	19
3-13.	Baseline Single Rod	20
3-14.	Modified Single Rod	20
3-15.	Side View 1" Double Wrap	21
3-16.	Top View 1" Double Wrap	21
3-17.	Single Grid Dye Injection Point 1 (Baseline left, Modified right)	22
3-18.	Single Grid Dye Injection Point 2 (Baseline left, Modified right)	22
3-19.	Single Grid Dye Injection Point 3 (Baseline left, Modified right)	22
3-20.	Single Screen, Dye Injection Location 1 (Baseline left, Modified right)	23
3-21.	Single Screen, Dye Injection Location 2 (Baseline left, Modified right)	23
3-22.	Single Screen, Dye Injection Location 3 (Baseline left, Modified right)	24

FIGURE PAGE

4-1. Probe Oscillation Sensitivity and Free-Stream Turbulence Data.....27

4-2. Single Grid Test Model in Water Tunnel.....29

4-3. Test Point Locations behind the Grid Models.....29

4-4. Single Screen Test Set-up Side View.....31

4-5. Hot Film Probe Mount and Traversing System.....31

4-6. Single Screen Set-up Schematic.....32

4-7. Screen Test Point Area as seen through upstream view.....33

4-8. Axial Velocity Profiles at Center Location 20d downstream of Single Grids..34

4-9. Single Grid Test Point Axial Velocity Statistical Comparison.....35

4-10. Single Grid Average Statistical Comparison.....36

4-11. 3-D Velocity Profiles in the vertical plane 5 inches downstream of Single Grids.....36

4-12. 3-D Turbulence Intensity Profiles in the vertical plane 5 inches downstream of Single Grids.....37

4-13. Single Grid Frequency Plots for Test Point 5.....38

4-14. Typical Axial Velocity Profiles 20 Diameters Downstream of Single Screens Re=600 (Test Point 2).....39

4-15. Typical Lateral Velocity Profiles 20 Diameters Downstream of Single Screens Re=600 (TP 2).....40

4-16. Axial and Lateral Velocity Statistics for all Single Screen Data at 20 Diameters Downstream.....41

4-17. Single Screen Axial Turbulence Intensity Traces Location 2, 20 Diameters Downstream.....42

4-18 Figure 4-18. Single Screen Lateral Turbulence Intensity Traces Location 2, 100 Diameters Downstream.....42

4-19. Single Screen Average TI Statistical Comparison at 20d (top left), 100d (top right), and 192d (bottom) Downstream.....43

4-20. Turbulence Intensity Plots showing the effect of lower mean velocity behind the modified screen.....44

FIGURE		PAGE
4-21.	Axial Velocity Surface Plot 20 Diameters downstream of Single Screens	45
4-22.	Axial Turbulence Intensity Surface Plot 20 Diameters downstream of Single Screens	46
4-23.	Axial Velocity Frequency Spectrum Plots 20 Diameters Downstream of Screens (0 to 200 Hz left, 1-20 Hz right)	47
4-24.	Lateral Velocity Frequency Spectrum Plots 20 Diameters Downstream of Screens (0 to 20 Htz)	47
4-25.	Axial Turbulence Intensity Profiles downstream of Single Screens	48
4-26.	Lateral Turbulence Intensity Profiles downstream of Single Screens	49
A-1.	Hot Film Sensor Velocity Components	62
A-2.	IFA100 Hot Film Calibration Set-up with Tow Tank	64
A-3.	IFA100 Hot Film Calibration Curve with King's Law Non-Linear Curve Fit	65
A-4.	IFA100 Hot Film Calibration Polynomial Curve Fit	66
A-5.	IFA300 Hot Film Calibration Curves for Single Screen Tests	67
B-1.	Water Tunnel Calibration Curves (Linear Curve Fit on Top and 2nd Order Polynomial Curve Fit on Bottom)	69
C-1.	Single Grid Location 01 Velocity and Frequency Spectra Plots	71
C-2.	Single Grid Location 02 Velocity and Frequency Spectra Plots	72
C-3.	Single Grid Location 03 Velocity and Frequency Spectra Plots	73
C-4.	Single Grid Location 04 Velocity and Frequency Spectra Plots	74
C-5.	Single Grid Location 05 Velocity and Frequency Spectra Plots	75
C-6.	Single Grid Location 06 Velocity and Frequency Spectra Plots	76
C-7.	Single Grid Location 07 Velocity and Frequency Spectra Plots	77
C-8.	Single Grid Location 08 Velocity and Frequency Spectra Plots	78
C-9.	Single Grid Location 09 Velocity and Frequency Spectra Plots	79
D-1.	Single Screen Location 01, 20 Diameters Downstream Axial Velocity and Frequency Spectra Plots	81

FIGURE PAGE

D-2. Single Screen Location 02, 20 Diameters Downstream Axial Velocity and Frequency Spectra Plots....82

D-3. Single Screen Location 03, 20 Diameters Downstream Axial Velocity and Frequency Spectra Plots....83

D-4. Single Screen Location 04, 20 Diameters Downstream Axial Velocity and Frequency Spectra Plots....84

D-5. Single Screen Location 05, 20 Diameters Downstream Axial Velocity and Frequency Spectra Plots....85

D-6. Single Screen Location 01, 20 Diameters Downstream Lateral Velocity and Frequency Spectra Plots....86

D-7. Single Screen Location 02, 20 Diameters Downstream Lateral Velocity and Frequency Spectra Plots....87

D-8. Single Screen Location 03, 20 Diameters Downstream Lateral Velocity and Frequency Spectra Plots....88

D-9. Single Screen Location 04, 20 Diameters Downstream Lateral Velocity and Frequency Spectra Plots....89

D-10. Single Screen Location 05, 20 Diameters Downstream Lateral Velocity and Frequency Spectra Plots....90

D-11. Single Screen Location 01, 20 Diameters Downstream Axial and Lateral Velocity Turbulence Intensity Plots....91

D-12. Single Screen Location 02, 20 Diameters Downstream Axial and Lateral Velocity Turbulence Intensity Plots....92

D-13. Single Screen Location 03, 20 Diameters Downstream Axial and Lateral Velocity Turbulence Intensity Plots....93

D-14. Single Screen Location 04, 20 Diameters Downstream Axial and Lateral Velocity Turbulence Intensity Plots....94

D-15. Single Screen Location 05, 20 Diameters Downstream Axial and Lateral Velocity Turbulence Intensity Plots....95

D-16. Single Screen Location 01, 100 Diameters Downstream Axial and Lateral Velocity Plots....96

D-17. Single Screen Location 02, 100 Diameters Downstream Axial and Lateral Velocity Plots....97

FIGURE PAGE

D-18. Single Screen Location 03, 100 Diameters Downstream Axial and Lateral Velocity Plots....98

D-19. Single Screen Location 04, 100 Diameters Downstream Axial and Lateral Velocity Plots.... 99

D-20. Single Screen Location 05, 100 Diameters Downstream Axial and Lateral Velocity Plots....100

D-21. Single Screen Location 01, 100 Diameters Downstream Axial and Lateral Velocity Turbulence Intensity Plots....101

D-22. Single Screen Location 02, 100 Diameters Downstream Axial and Lateral Velocity Turbulence Intensity Plots....102

D-23. Single Screen Location 03, 100 Diameters Downstream Axial and Lateral Velocity Turbulence Intensity Plots....103

D-24. Single Screen Location 04, 100 Diameters Downstream Axial and Lateral Velocity Turbulence Intensity Plots....104

D-25. Single Screen Location 05, 100 Diameters Downstream Axial and Lateral Velocity Turbulence Intensity Plots....105

D-26. Single Screen Location 01, 192 Diameters Downstream Axial and Lateral Velocity Plots....106

D-27. Single Screen Location 02, 192 Diameters Downstream Axial and Lateral Velocity Plots....107

D-28. Single Screen Location 03, 192 Diameters Downstream Axial and Lateral Velocity Plots....108

D-29. Single Screen Location 04, 192 Diameters Downstream Axial and Lateral Velocity Plots....109

D-30. Single Screen Location 05, 192 Diameters Downstream Axial and Lateral Velocity Plots....110

D-31. Single Screen Location 01, 192 Diameters Downstream Axial and Lateral Velocity Turbulence Intensity Plots....111

D-32. Single Screen Location 02, 192 Diameters Downstream Axial and Lateral Velocity Turbulence Intensity Plots....112

D-33. Single Screen Location 03, 192 Diameters Downstream Axial and Lateral Velocity Turbulence Intensity Plots....113

FIGURE PAGE

D-34. Single Screen Location 04, 192 Diameters Downstream Axial and Lateral Velocity Turbulence Intensity Plots.....114

D-35. Single Screen Location 05, 192 Diameters Downstream Axial and Lateral Velocity Turbulence Intensity Plots.....115

D-36. Single Screens 100 and 192 Diameters Downstream Axial and Lateral Velocity Statistics.....116

D-37. Single Screens 100 and 192 Diameters Downstream Axial and Lateral Velocity Turbulence Intensity Statistics.....117

D-38. Single Screens 100 and 192 Diameters Downstream Axial Velocity Surface Plots.....118

D-39. Single Screens 100 and 192 Diameters Downstream Axial Velocity Turbulence Intensity Surface Plots.....119

LIST OF TABLES

TABLE		PAGE
3-1.	Single Rod Test Configurations	18
4-1.	Probe Oscillation and Free Stream Turbulence Survey	28
4-2.	Single Grid Test Point 5 Statistical Summary	35
4-3.	Screen, Single Point Axial Velocity Statistical Summary	40
4-4.	Screen, Single Point Lateral Velocity Statistical Summary	40

LIST OF SYMBOLS

ρ_∞ free stream density

μ_∞ free stream fluid coefficient of viscosity

$\overline{U}_\infty$ free stream average axial velocity

T_∞ free stream temperature of the fluid

D_{ds} distance downstream

D_{hw} distance between subsequent helical wraps

D_g distance between grid rods

d_g diameter of the grid rods

d_{hw} diameter of the helical wrap

σ_{ds} turbulence downstream of the grid

σ_∞ free stream turbulence

ε_g surface roughness effect of the helical wrap

Hz Hertz or cycles per second

f_g vortex shedding frequency

β grid and screen porosity (ratio of grid or screen open area to total area)

$K = \dfrac{\Delta P}{1/2\rho U^2}$ Pressure loss coefficient

$\mathrm{Re}_d = \dfrac{\rho_\infty \overline{U}_\infty d_g}{\mu_\infty}$ Reynolds number based on grid/screen rod diameter

$St_d = \dfrac{f_g d_g}{U_\infty}$ Strouhal number

$\frac{\mu_\infty}{\rho_\infty} = \nu_\infty$ Kinematic Viscosity

V_∞ Free Stream Velocity

N Number of samples

$\overline{U} = \frac{1}{N}\sum_{i=1}^{N} u$ Average Velocity

$U' = \frac{1}{N-1}\sum_{i=1}^{N}\left(\overline{U} - u_i\right)^2$ Variance

$\sigma = \sqrt{\frac{1}{N-1}\sum_{i=1}^{N}\left(\overline{U} - u_i\right)^2}$ Standard Deviation

$TI = \frac{\sigma}{\overline{U}}$ Turbulence Intensity

$TI_{Baseline} = \frac{\sqrt{(\overline{U}_{Baseline} - u_i)^2}}{\overline{U}_{Baseline}}$ Turbulence Intensity downstream of Baseline Screen

$TI_{Modified} = \frac{\sqrt{(\overline{U}_{Modified} - u_i)^2}}{\overline{U}_{Baseline}}$ Turbulence Intensity downstream of Modified Screen for direct comparison purposes ("comparison corrected")

$\overline{U}_{Baseline}$ Average Velocity at downstream location of Baseline Screen

$\overline{U}_{Modified}$ Average Velocity at downstream location of Baseline Screen

V_N Velocity normal to the sensor and parallel to the supports

V_T Velocity tangential to the sensor

V_{BN} Velocity normal to the sensor and supports

E^2 Hot Film Sensor Voltage Squared

2-D two dimensional

3-D three dimensional

20 D the 20 diameter (based on the grid and rod ¼ inch) downstream location

Chapter 1

INTRODUCTION

Turbulence Reduction Systems (TRS) such as honey combs and wire mesh screens in wind/water tunnel applications are designed for maximum attenuation of the flow non-uniformities, flow unsteadiness, and turbulence levels. In high Reynold number facilities with pressurized circuits, the low stilling chamber Reynold numbers desired for TRS operation, can not be readily attained. To meet flow uniformity and low turbulence requirements in the test sections in such facilities, a new type of wire mesh screen design may allow for comparable turbulence management at somewhat higher stilling chamber Reynold numbers. This new design, although more complex to manufacture, may prove inherently more effective in reducing flow non-uniformities and downstream turbulence levels. This thesis presents preliminary experimental results on the operation of this new wire mesh screen. The design employs a helical wrap modification to existing screens and takes advantage of the enhanced three dimensionality of the flow created by the wrap.

The need for low free-stream turbulence in wind tunnels and water tunnels has increased with technological enhancements in aerodynamic and hydrodynamic drag reduction designs. In many ground testing investigations it is imperative to tailor the free-stream flow for axial velocity uniformity, flow angularity, and turbulence level. Free-stream turbulence effects can also be significant in laminar flow studies and transition flow studies where very low turbulence levels would be ideal and minimization is certainly essential. Frequently it is also quite difficult to separate Reynold's number effects from significant free-stream turbulence effects.

This research has been undertaken to explore the physics behind this enhanced screen design. Particularly, the flow fields immediately downstream of the modified and baseline test articles are investigated qualitatively and quantitatively to address the turbulence attenuation capabilities of the new design. Because the upstream turbulence is relatively small

scale (as compared to the test articles), the overall flow turbulence reduction is not important nor relevant in this investigation. The general flow characteristics, however, downstream of the test articles, including screen generated turbulence structure and downstream flow coherence, are critical and as such are thoroughly investigated and compared.

This study is an experimental investigation into the effects on downstream flow coherence, structure and turbulence transition created by adding a helical wrap pattern to cylindrical rods, single grids and small screens. Modified test articles were compared to baseline models (without the added wrap) which were subjected to identical flows. Preliminary tests were conducted for two flow conditions (Reynold numbers of 75 and 600). The water tunnel was selected over the wind tunnel for this investigation because of its enhanced flow visualization capabilities. The kinematic viscosity of air (approximately one order of magnitude larger than that of water) would allow for the use larger, more easily measured flow velocities for the same test Reynolds numbers. The measurement of flow fluctuations at these larger velocities would likely be more easily measured and future testing should consider these test medium over the water tunnel

This research was designed primarily as a proof of concept study to document the advantages of this TRS modification technique as a precursor to more detailed, follow-on research. Qualitative flow visualization tests were initially conducted, followed with quantitative flow field measurements. After a presentation of the background information associated with this research in Chapter 1, these two areas of study are presented in Chapters 3 and 4, each in turn. Finally, conclusions and recommendations are presented in Chapter 5.

Chapter 2

BACKGROUND AND THEORETICAL CONSIDERATIONS

Literature Review and Theoretical Considerations

General

A thorough review of existing work in the field of turbulence attenuation systems revealed a wide scope of efforts to eliminate turbulence in test facilities. Traditionally, screens, grids or perforated plates, and honeycombs have been used to straighten the flow (create more axially uniform flow) and reduce large-scale free-stream turbulence and flow swirling. *Prandtl* [1] was the first in 1933 to recognize the benefits of using a wire mesh screen to reduce wind tunnel velocity non-uniformities. The primary smoothing mechanism was the higher drag associated with higher velocity flow. The fundamentals of the theory of turbulence are addressed in classic works by *Batchelor* [2], *Bradshaw* [3] and *Townsend.*[4]. Excellent reviews of existing theories and experimental data are provided by *Corrsin* [5] and by *Laws and Livesey* [6]. Substantial efforts have been made to determine simple empirical formula to predict the turbulence reduction effectiveness of screens. Many researchers have studied the influence of the pressure loss coefficient $\frac{\Delta P}{1/2\rho U^2}$ (referred to as K) across the screen and most have concluded that this is the key parameter in turbulence reduction. Screens are typically characterized using this pressure loss coefficient. *Dryden and Schubauer* [7] developed a simple formula for the turbulence reduction factor using this parameter. A thorough collection of most of the developed formula for turbulence reduction prediction are summarized in a paper by *Aljabari* [8].

As already mentioned, the design of flow straighteners and Turbulence Reduction Systems (TRS) such as honey combs and wire mesh screens in wind tunnel applications are based on maximum attenuation of the flow non-uniformities and unsteadiness. In high Reynolds number facilities with pressurized circuits, the desired low stilling chamber Reynolds

number can not be readily attained. In such situations, in order to meet flow uniformity and low turbulence requirements in the test section, two possibilities exist. The first option involves using the current screen technology and designing the stilling chamber for operation at very low flow speeds (sub-critical Reynolds numbers based on the fine wire diameters). This typically results in relatively large stilling chambers and proportionately higher manufacture and operation costs. An alternate approach is to utilize a new type of wire mesh design (discussed in this paper), which achieves comparable turbulence reduction when compared to existing screen design, however, at a higher Re. This would allow the operation of such facilities using either smaller (higher velocity) stilling chambers or larger, stronger screens. The bending or warping of low Reynold number screens in the large stilling chambers were highlighted in a related paper by *J. Watmuff* [9] as sources of significant flow velocity and turbulence non-uniformities. Accordingly, a higher Reynolds number screen would enhance flow parameter uniformity by allowing the use of larger, stronger screens which are less susceptible to bending and warping.

At Reynold numbers typically larger than forty (based on cylinder diameter), circular cylinders in uniform cross-flow develop unstable wakes. The wake is convectively unstable and rolls into large scale coherent rotational flow, which for higher Reynolds numbers is called the Von-Karman vortex street which is composed of positive and negative vorticity regions formed in a coherent and concentrated manner. Depending on the flow, these vortices or eddies develop higher frequency instabilities and eventually decay into isotropic turbulence. The design of TRS systems in any wind tunnel is based not only on eliminating turbulence generated in the flow circuit from the many potential sources including: Fans, Heaters, Coolers, Turning Vanes etc., but also on the nature of the turbulence generated by the TRS itself. This self generated turbulence must decay within a short distance downstream of the TRS. This determines the test section flow turbulence level and therefore can determine the optimum flow quality in the tunnel. The flow decay properties downstream of the modified test articles are therefore important in this research.

Motivation for New Screen Design

Practically all existing theories of turbulence reduction ignore the velocity

fluctuations and complex flow which occur immediately downstream of screens operating in the critical range (Re>40). More recently, *Butler* and *Farrell* [10] have demonstrated the importance of three dimensional behavior effecting turbulence in viscous shear flows. The nature of perturbations in shear flows have been incompletely explained by traditional 2-D nonlinear instability theory. In their paper, the critical importance of considering the three dimensional behavior of vortices (vortex tilting and interaction) shows promise in better predicting flow instability and transition to turbulence in various flow types (ie, Couette, Poissielle, etc.). It has been long known that a finely tuned helical wrap pattern reduces the drag on a cylindrical rod. This fact has been leveraged to advantage in industrial applications where smoke stacks routinely employ this structural enhancement technique to reduce aerodynamic drag.

Research conducted previously by *Cornish* [11] has also suggested that a modified grid or screen employing helical external wrapping of each cylindrical rod in the pattern, can reduce or eliminate the turbulence-generating vortices that are shed as the flow passes through the screen (around the cylindrical rods). He surmises that increasing the core-wise flow in the vortices will help reduce structured, oscillatory shedding of the vortices. Cornish sights a primary technique using splitter plates for inducing this core-wise flow which makes the flow more three dimensional in structure and helps dissipate the periodic shedding vortices. In essence the splitter plates turn the vortices 90 degrees which induces an additional core-wise flow velocity component which draws fluid out of the transverse vortices rolling up behind the cylinder. As a result, this prevents the growth in the transverse direction of the shedding vortices. The result is a stable, non oscillatory horseshoe vortex behind the cylinder as shown in Figure 2-1 [11].

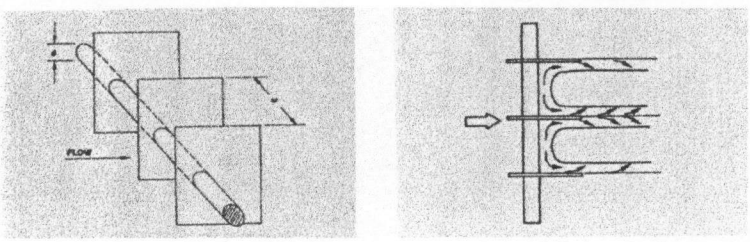


Figure 2-1. Cylindrical Rod Splitter Plates

This same basic principle is utilized, to a much smaller degree, with the helical wrap, however, an additional component of core-wise velocity which follows the trajectory of the helical wrap (very three dimensional) is superimposed on the flow. The wrap initially acts somewhat like the splitter plates and effectively adds substantial three dimensionality to the flow. This enhanced and dynamic 3-D core-wise flow interacts to form very complicated and periodic, but substantially less structured flow downstream. This subsequently breaks down the coherent 2-D, transverse oriented, shedding vortex structures making the flow less coherent and effectively reducing the structured energy in the flow. It is critical to note that the intent in this research is not to eliminate the oscillatory nature of the shedding vortices, but rather to reduce the overall structured energy in the shedding vortices. The goal is to promote 3-D interactions and mixing of the shedding vortices by way of the helical wrap. The potential merits of this new approach for wind/water tunnel free stream turbulence manipulation and subsequent reduction and control have prompted this initial investigation.

Experimental Considerations - Dimensional Analysis/ Similitude

Fluid dynamicists rely on carefully designed experiments to gain insight into complicated fluids problems which cannot be solved analytically. Typically, aerodynamic experiments are conducted on scaled down versions of the prototypes to minimize test apparatus sizes and test expenses. To ensure that experimental results properly reflect the full scale flow performance, geometric and dynamic similarity between the prototype and the scaled down version are essential. Dimensional analysis also allows for the consolidation of the numerous variables governing the complex flow into a reduced, more manageable number of dimensionless parameters. Equating these non-dimensional parameters permits the direct comparison of experimental data obtained using a scaled down prototype with the full scale model.

In the general case, the relationship between the downstream turbulence intensity behind a helically wrapped, cylindrical rod screen and the independent parameters can be described by the following function:

$$f_1\left(\rho_\infty, \mu_\infty, \overline{U}_\infty, T_\infty, D_{ds}, D_{hw}, D_g, d_g, d_{hw}, \sigma_{ds}, \sigma_\infty, \varepsilon_g, f_g, \beta\right) = 0$$

where

ρ_∞ is the free stream density

μ_∞ is the free stream fluid coefficient of viscosity

$\overline{U}_\infty$ is the free stream average axial velocity

T_∞ is the free stream temperature of the fluid

D_{ds} is the distance downstream

D_{hw} is the distance between subsequent helical wraps

D_g is the distance between grid rods

d_g is the diameter of the grid rods

d_{hw} is the diameter of the helical wrap

σ_{ds} is the turbulence downstream of the grid

σ_∞ is the free stream turbulence

ε_g is the surface roughness effect of the helical wrap

f_g is the vortex shedding frequency

β is the porosity (ratio of grid or screen open area to total area)

This representation is for an incompressible fluid which is a good assumption for low velocity flows in water. The temperature effects are considered negligible in water and the helical wrap diameter effects are also considered small. The surface roughness is ignored as the effects are minimal when compared to the geometry of the wrapped grid. With these assumptions and using three primary dimensions[M,L,T] the dimensional analysis results in:

$$f_2\left(\frac{\rho_\infty \overline{U}_\infty d_g}{\mu_\infty}, \frac{D_{ds}}{d_g}, \frac{D_{hw}}{d_g}, \frac{D_g}{d_g}, \frac{\sigma_{ds}}{U_\infty}, \frac{\sigma_\infty}{U_\infty}, \frac{f_g d_g}{U_\infty}, \beta\right) = 0$$

which reduces to

$$f_3\left(\mathrm{Re}_d, \frac{D_{ds}}{d_g}, \frac{D_{hw}}{d_g}, \frac{D_g}{d_g}, \frac{\sigma_{ds}}{\overline{U}_\infty}, \frac{\sigma_\infty}{\overline{U}_\infty}, St_d, \beta\right) = 0$$

recalling that $\mathrm{Re}_d = \dfrac{\rho_\infty \overline{U}_\infty d_g}{\mu_\infty}$, and

$$\text{the Strouhal number } St_d = \frac{f_g d_g}{U_\infty}$$

In this investigation, the grid characteristics and the wrap characteristics (independent parameters) were fixed and accordingly the dimensional analysis results in:

$$f_4\left(\mathrm{Re}_d, \frac{\sigma_{ds}}{\overline{U}}, \frac{\sigma_\infty}{\overline{U}_\infty}, St_d, \beta\right) = 0$$

Therefore, the downstream turbulence intensity is a function of the Reynolds number, Strouhal number, the initial free stream turbulence intensity and the porosity. For the purposes of this initial investigation, the upstream turbulence was not manipulated nor scaled as a controlled input. This study was primarily concerned with studying the coherence and physical structure (St_d indirectly) of the flow downstream of the baseline and modified test articles. A limited parametric study was attempted by varying the Re_d and by the fact that the grid and screen test article porosity's were inherently different. Preliminary results of this research effort were presented in two AIAA papers by *McKeage* and *Vakili* [12 and 13].

Chapter 3

FLOW VISUALIZATION TESTS

Experimental Objectives

The primary objective of the flow visualization testing was to qualitatively select the optimum helical wrap characteristics for follow-on quantitative turbulence reduction effectiveness testing for the grid and screen test articles. A secondary, and no less important, objective was to qualitatively characterize the complex downstream flows in order to better understand the physics governing the flow characteristics behind the baseline and modified test articles.

Experimental Set-up and Method

The Test Articles

In order to characterize the flow field behind the modified test articles to determine the resulting turbulence reduction effectiveness, several test models were manufactured for evaluation. Flow visualizations downstream of single rods, single grids and single screens were conducted at a single Reynolds number (Re_d) of approximately 75 (with respect to wire diameter). This lower Re_d (still in the super-critical regime and representative of the Re_d of 600 flow) allowed for more effective recording and analysis of the flow visualization.

Single Rods. Single ¼ inch diameter cylindrical rods (each typically 10 to 12 inches long) were evaluated with and without the 22 gauge (.022 inches)helical wire wrap. The baseline and 1 inch single wrap rods are shown in Figure 3-1 for a side by side comparison. The single and double helical wrap patterns evaluated are detailed in Figure 3-2. The pitch length used to characterize the wrap corresponded to the length per 360° of wire wrap.

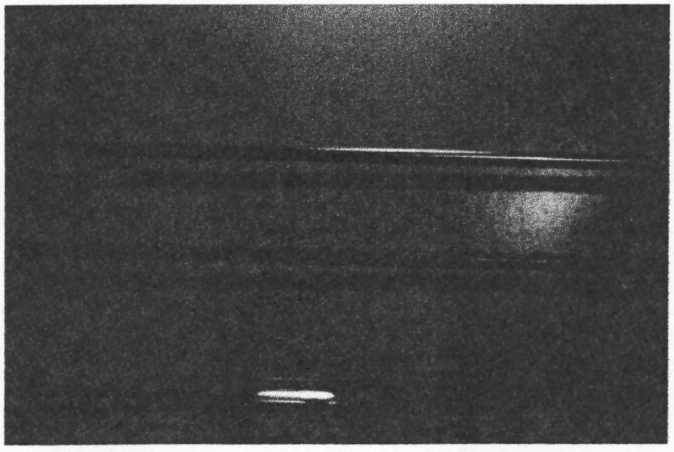


Figure 3-1. Baseline (top) and Modified (bottom) Single Rods

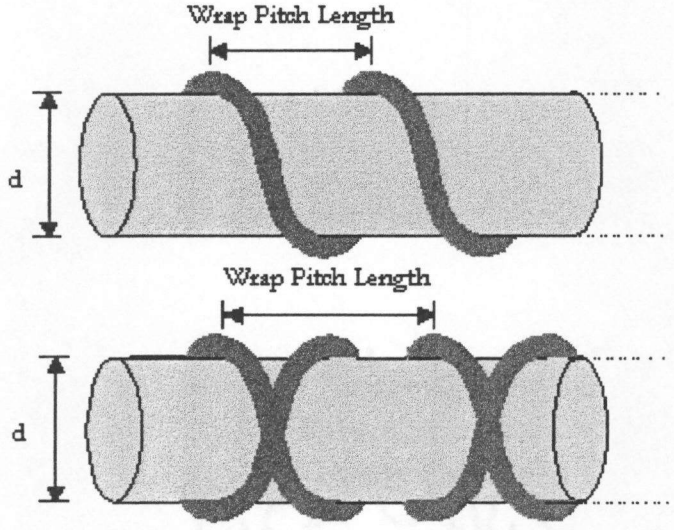


Figure 3-2. Single (Top) and Double (Bottom) Helical Wrap Pattern

The 1" wrapped cylindrical rod was wrapped with a criss-crossed 1 inch wrap (180° out of phase) such that the two wraps crossed at the forward and rearward cylinder surfaces at locations perpendicular to the free stream flow. The motivation for considering the double wrap configuration was the potential benefit of the discrete flow separation points created at

the cross locations of the two wraps. The rationale was that these out of phase helical wraps would further add incoherence to the flow structures, particularly on the shedding vortex structures.

Single Grids. The single grids were constructed of four equal length ¼ inch rods (each 4 ½ inches long) welded in an overlapped configuration with a centered mesh opening which measured 1 and 7/8 inches between rod centers. The single grids were evaluated in the baseline and 1 inch single and double wrap configurations as shown in Figure 3-3.

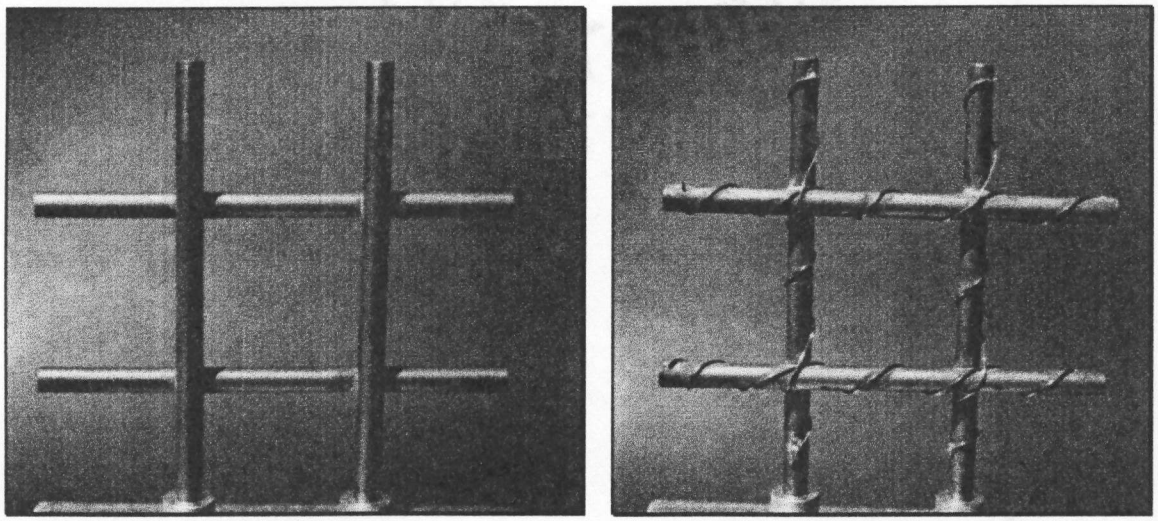


Figure 3-3. Single Grids (Baseline and 1 inch Single wrap)

The single grid porosity (β) was calculated to be 75.1% which is significantly higher than the single screen porosity calculated below.

Single Screens. The screens were 12 inch by 12 inch mesh screens with ¾ inch openings constructed with ¼ inch diameter stainless steel wire interlaced in a regular weave. The screen porosity was calculated to be 56.3%. These screens were commercially available and were classified as 1 x 1 mesh per linear inch screens. The modified screen was hand wrapped with 22 gauge copper wire using the double, reversed helical wrap pattern. The baseline and modified screens are shown in Figure 3-4.

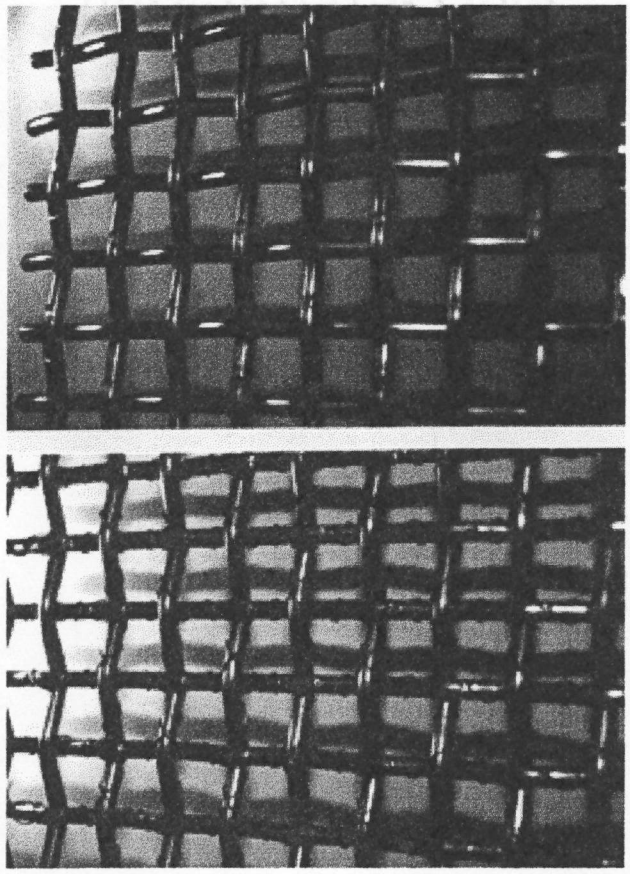


Figure 3-4. Baseline (Top) and Modified (Bottom) Screens

The Test Facility

All flow visualization tests were conducted in the University of Tennessee Space Institute (UTSI) Water Tunnel. The UTSI Water Tunnel (shown in Figure 3-5) is a closed circuit system driven by a propeller powered with a 1 horsepower electric motor which drives a 10 inch diameter two bladed propeller. Approximately half of the closed system circuit is enclosed inside a heated building with the remaining part of the circuit completely outdoor and exposed to environmental conditions. The test section volume measures 12" x 18" x 60" with an open upper surface and a single plexiglass wall to permit full side viewing of the flow. The tunnel layout is illustrated in Figure 3-6. The tunnel was rated for flow velocities ranging from 0.25 inches/sec to 12 inches/sec.

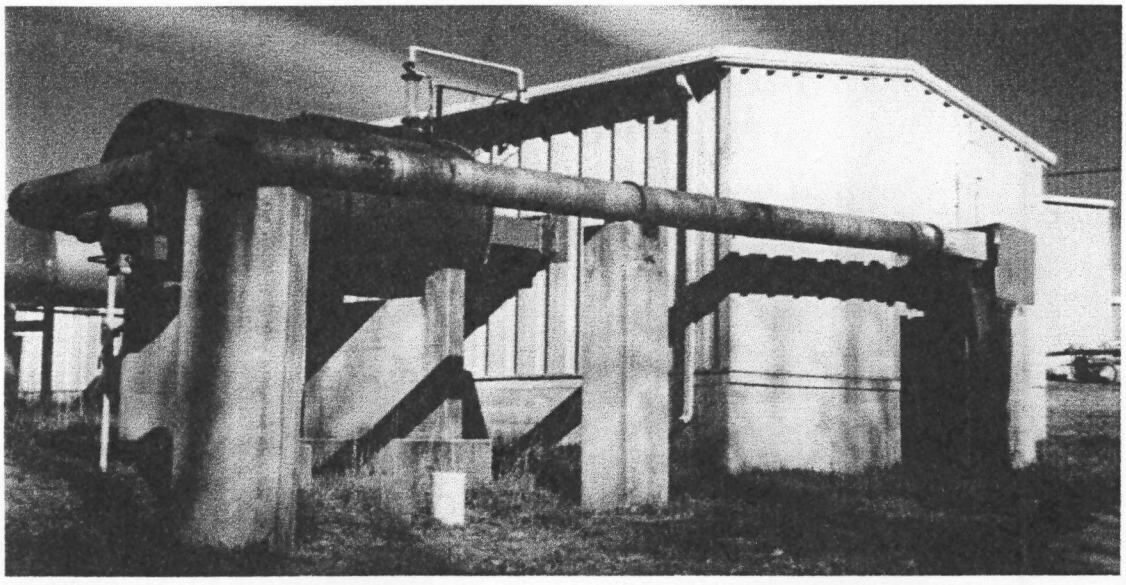
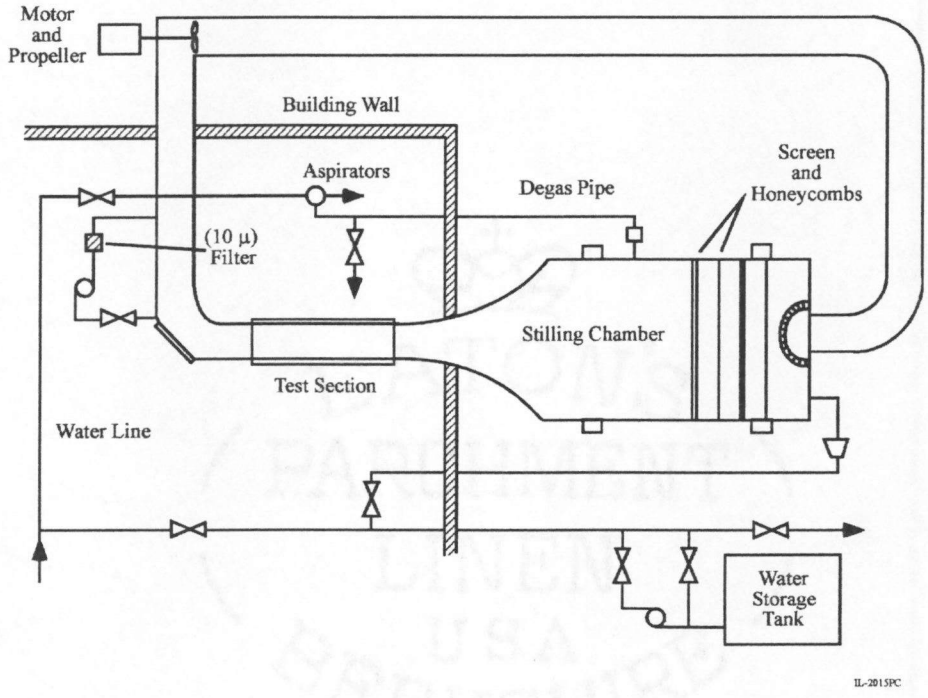


Figure 3-5. UTSI Water Tunnel



Schematic Layout of the UTSI Water Tunnel Circuit

Figure 3-6. UTSI Water Tunnel Layout Schematic

Prior to collecting data in the water tunnel, the free-stream turbulence level was determined at the selected Re_d. At the same time the probe oscillation sensitivity, due to probe stem insertion into the flow, was assessed at three different vertical locations in the water tunnel (at the data collection location). The results of these free-stream surveys showed a turbulence intensity of approximately 1.5% and are further discussed in Chapter 4.

The Experimental Set-up

Visualization of the flow behind the test items was obtained by injecting laser sensitive dye into a flow plane illuminated with a sheet of Argon Ion laser light aligned vertically with the free-stream flow. Two-dimensional images of the dynamic flow characteristics of dye particles continuously injected at a single point source were obtained. The test set-up is shown in Figure 3-7 (indoor water tunnel test section) with a layout schematic shown in Figure 3-8.

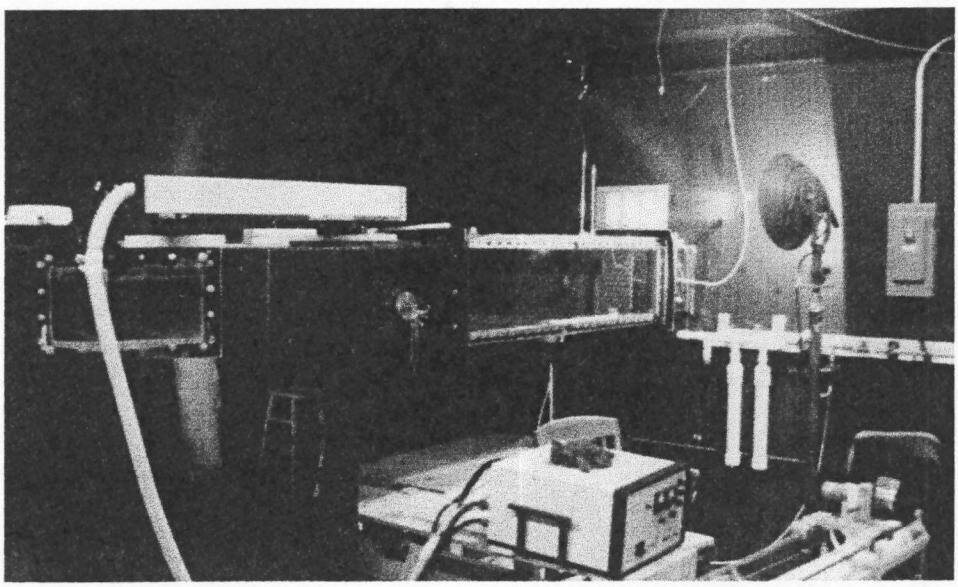


Figure 3-7. Water Tunnel 4 Watt Argon Ion Laser Set-up

The flow characteristics were recorded using a VHS video camera to aid in qualitative analysis and flow field comparisons between the baseline and modified grids. Still images taken from these video recordings are included in this thesis to further illustrate the flow

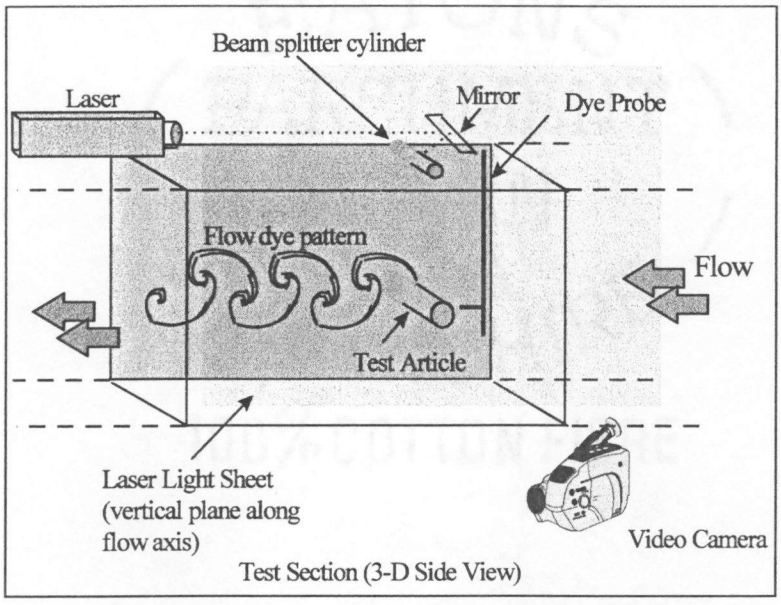


Figure 3-8. Flow Visualization Setup Schematic

characteristics and substantiate wrap selection decisions. Flows behind the following test configurations were systematically visualized:

a) single 0.25 inch diameter cylindrical rod in various configurations including;
   i. the baseline unwrapped configuration;
   ii. with various single helical wrap configurations;
   iii. and with a 1 inch double, inverse wrap configuration;
b) single grid pattern of 0.25 inch rods in in the baseline (unwrapped) and both single and double wrapped configurations using a 1" pitch length for the helical wrap; and
c) a single screen pattern in the baseline (unwrapped) and double wrapped configurations using a 1" pitch length for the helical wrap.

Test Reynolds Number

All flow visualization tests were conducted at the same free-stream flow conditions (Digital Metering setting of 0.43 volts for the water tunnel flow control). The corresponding free stream velocity for this flow setting was measured at approximately 0.43

inches per second which corresponded under local conditions to a Reynolds number (based on rod diameter 0.25 inches) of 75.

$$\mathrm{Re}_d = \frac{\rho_\infty \overline{U}_\infty d_g}{\mu_\infty} = 75$$

For H_2O at room temperature:

$$\text{Kinematic Viscosity } \frac{\mu_\infty}{\rho_\infty} = \nu_\infty = 1.55 \text{ X } 10^{-3} \text{ inches}^2/\text{second}$$

$$\text{Free Stream Velocity } V_\infty = 0.43 \text{ inches per second}$$

$$\text{Rod Diameter } d_g = 0.25 \text{ inches}$$

All subsequent flow visualization testing was conducted at this approximate Re_d by selecting the same flow control setting for the water tunnel.

Dye Injection Technique

A special dye injection probe was designed and manufactured for the purposes of these flow visualizations. The design was undertaken to obtain a probe which minimized influences on the upstream flow characteristics. Accordingly, a thin probe structure utilizing an airfoil-like shape was manufactured. The final design is illustrated in Figure 3-9.

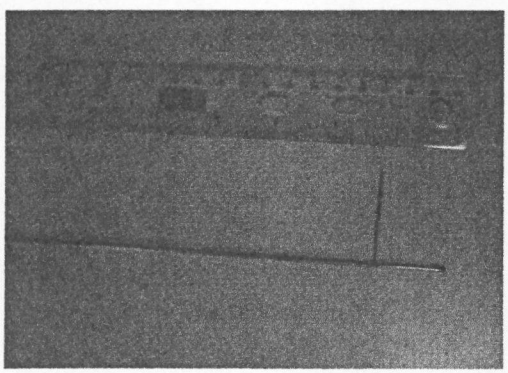


Figure 3-9. Dye Probe Design

The interference of this probe with the downstream flow characteristics was evaluated by comparing the flows behind a baseline cylindrical rod with and without the dye probe inserted in the up-stream flow (in identical flows). The baseline flow (no dye probe) was

evaluated by using internal dye injection through a tiny hole at the forward stagnation point on the rod. Next the probe was used for dye injection at the same physical point on the cylinder (forward stagnation point) in identical free stream conditions. The resulting flow was identical to the baseline flow and no discernible differences were observed. Accordingly, the probe was selected as the preferred dye injection technique (over the internal injection method) based on:

a) the relative ease of moving the dye insertion point using an external probe;
b) negligible influences on the free stream flow using the dye probe;
c) questionable dye insertion quality and repeatability associated with using an internal dye injection technique in the modified (wrapped) test articles (the wrapping would likely impact dye injection quality); and
d) the technical difficulties associated with implementing the internal injection capability on the multiple-grid test articles.

The simplest solution, which adequately satisfied the requirements of the flow visualization, was to use the external dye injection probe. The flow fields down stream of the baseline and double wrapped (1" pitch length) single and multiple grid patterns were visualized using three separate dye injection locations. These locations are shown in Figure 3-10 with an upstream view orientation.

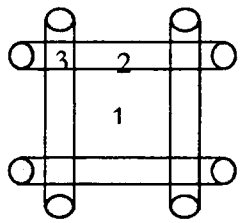


Figure 3-10. Dye Injection Locations on Single Grids and Screens with upstream view orientation

For the single screens, the dye was injected on the center grid in the middle of the screens at these same locations.

Flow Visualization Study - Results and Discussion

Single Rod Results

The baseline flow clearly demonstrated the periodic, cyclic vortex shedding behind the cylinder as expected at the low Re_d of approximately 75. The Strouhal Number (S_t) was calculated and conformed nicely with existing experimental data. The shedding frequency of the vortex pair was obtained by counting the number of vortex core pairs passing a stationary location in the flow per unit time. For a free stream velocity of approximately 0.455 inches per second and the characteristic length of 0.25 inches (rod diameter), the resulting Strouhal number was calculated as S_t=0.1875.

$$\text{Stouhal Number } St = \frac{fd}{U_\infty}$$

The wrapped rod configuration was evaluated using the various wrap pitch lengths which are specified in Table 3-1 below.

Table 3-1 - Single Rod Test Configurations

	Pitch Length (inches along rod per 360° wrap)						
	Baseline	0.5"	0.6"	0.7"	0.8"	0.9"	1.0"
Single Rod Single Wrap	X (No Wrap)	X	X	X	X	X	X
Single Rod Double Wrap							X

With increasing pitch length, the results showed a slight trend of increasing core-wise flow (longer axial shedding vortices) and an increase in the out of plane orientation of the shed vortices with respect to each other and the free-stream flow (dynamic 3-dimensionality in the vortices). That is to say that the injected dye pattern downstream of the rod appeared to diffuse or scatter more as the pitch length was increased from 0.5 inches to 1.0 inch.

Generally, the unmodified cylinder sheds strong, tightly wrapped vortices (with obvious core-wise flow) which all align with the lateral axis of the rod (90 degrees to the free stream flow). Although the vortices are all connected (meaning that there must be regions where the vortices are not aligned with the rod), these regions are small and have limited interactions (destructive interference). The addition of the wrap clearly effected the core-wise flow in the vortices as is shown in Figures 3-11and 3-12. The baseline flow shows the predominant transverse orientation of the shedding vortices' axes. The shedding vortex axes for the flow around the wrapped cylinder, however, are not completely aligned with the transverse rod axis. They are also mis-aligned with each other and as a result constructive and destructive interference is generated in the flow. This interference helps create randomized motion of the shedding vortices. The sooner this occurs in the down-stream flow, the sooner the viscous forces can destroy the vortices and transition to turbulence can occur.

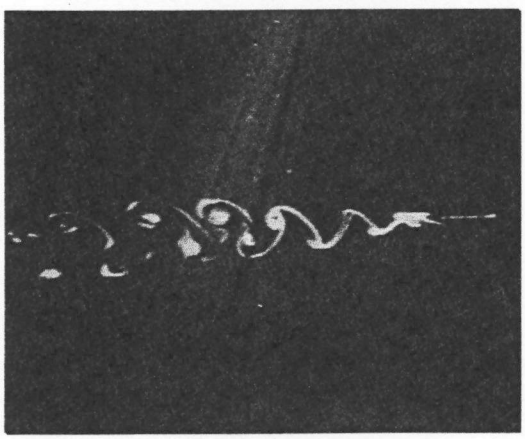


Figure 3-11. Baseline Single Rod Side View (Re_d=75)

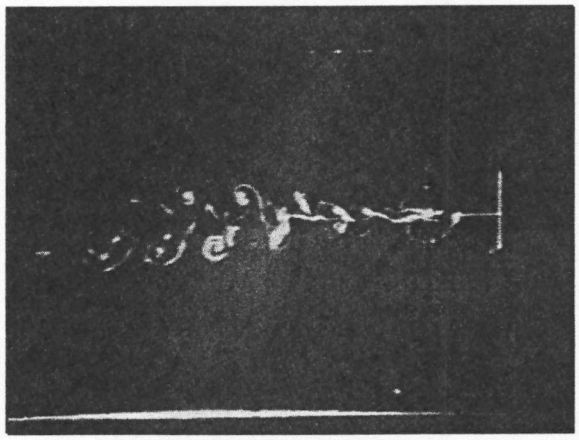


Figure 3-12. Single Rod 1" Single Wrap Side View (Re_d=75)

Top view comparisons of these flows are shown in Figures 3-13 and 3-14 further illustrating the breakdown of the vortex coherence behind the modified rod.

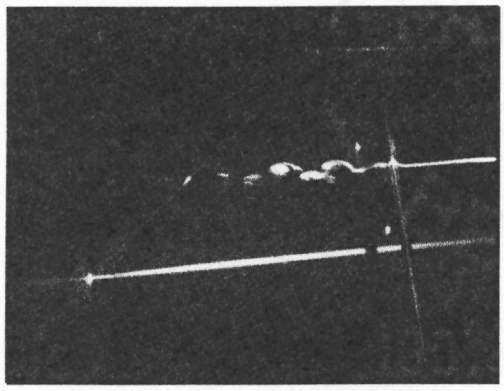


Figure 3-13. Baseline Single Rod (Re_d=75)



Figure 3-14. Modified Single Rod (Re_d=75)

The significantly reduced coherent, organized structure in the shedding vortices behind the wrapped rod are clearly illustrated in Figure 3-14. It was also very interesting to note that, although there was definite periodicity in all of the test flows (ie. vortex shedding occurring), the flow visualizations also clearly demonstrated unsteadiness in the mean flow. Distinct periods were observed where no vortex shedding took place followed by obvious periods of shedding. This was a relatively low frequency cycle with a period on the order of 30 to 60 seconds. This unsteadiness was likely a result of water tunnel propeller unsteady operation and overall closed system effects. This could adversely impact the quality of the data collected during the follow-on flow velocity measurements test phase. The relevance of direct comparisons between the test models may also be in question.

The 1 inch pitch wrap was selected as the preferred wrap configuration because of its enhanced vortex spreading destructive interference characteristics. The 1 inch wrap was also selected given the fact that the single screen test items were constructed in a 1 inch by 1 inch grid pattern. Using a 1 inch wrap would ensure a more homogeneous grid wrap (one wrap per grid). Incidentally, previous research revealed that the optimum splitter plate distance for reducing oscillatory vortex shedding is 4 times the rod diameter. In our case, this corresponded with the 1" wrap selection further supporting the flow physics observed.

Flow visualization results of the double wrap for identical flow conditions showed greater mixing and less coherent structure of the shedding vortices. Side view and top view

close-ups are shown in Figures 3-15 and 3-16 which demonstrate the enhanced three dimensionality of the vortex shedding created by the helical wrap.



Figure 3-15. Side View 1" Double Wrap (Re_d=75)

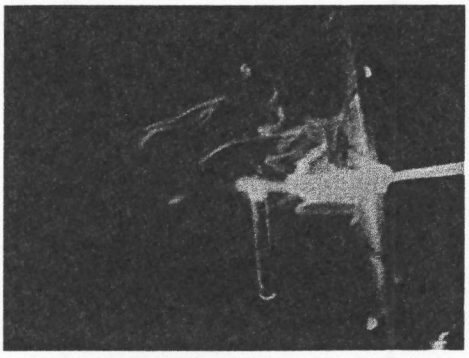


Figure 3-16. Top View 1" Double Wrap (Re_d=75)

Based on the single rod flow visualization results, the 1 inch double wrap configuration was selected for follow-on single grid and single screen flow visualization testing.

Single Grid Results

The same general trends demonstrated with the single rods were observed using the single grid test articles. The modified grid pattern (1 inch double helical wrap) showed a marked increase in the shedding vortex mixing and varying, three-dimensional vortex axes orientation. This was consistent for each of the dye insertion locations (1- center of grid, 2- middle of upper horizontal rod, 3 - rod intersection). A direct comparison of these flows is shown below in Figures 3-17, 3-18 and 3-19 for the three dye injection locations respectively. Figures on the left hand side of the page correspond with the baseline flow characteristics and modified flow characteristics on the right. As is clearly shown in the figures, flow behind the baseline grids showed much more vortex concentration and coherence. Vortex cores are clearly seen in the left hand figures whereas the flow behind the modified grid shows greater mixing without obvious concentrated vortex structures.

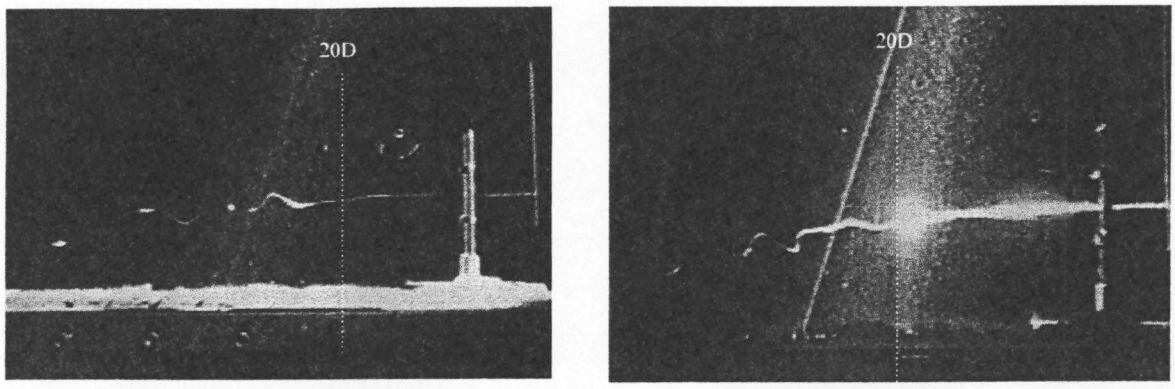


Figure 3-17. Single Grid Dye Injection Point 1 (Baseline left, Modified right) (Re_d=75)

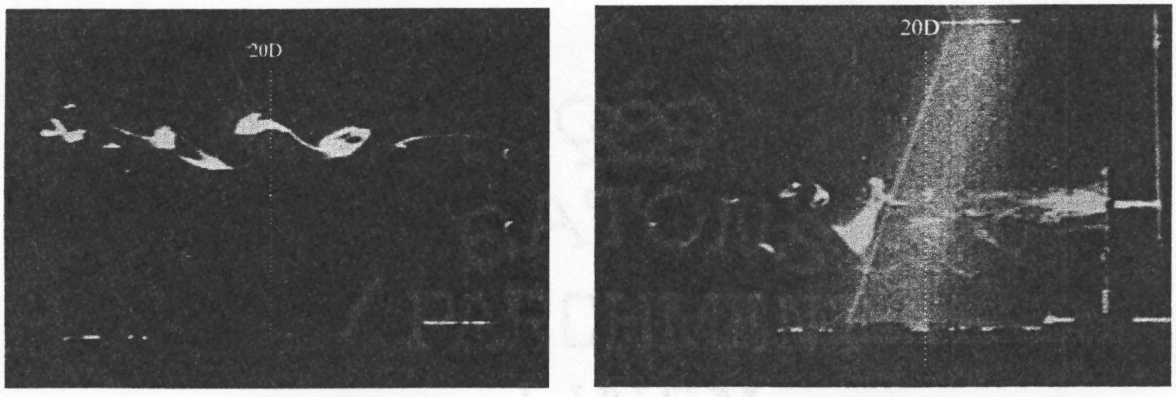


Figure 3-18. Single Grid Dye Injection Point 2 (Baseline left, Modified right) (Re_d=75)

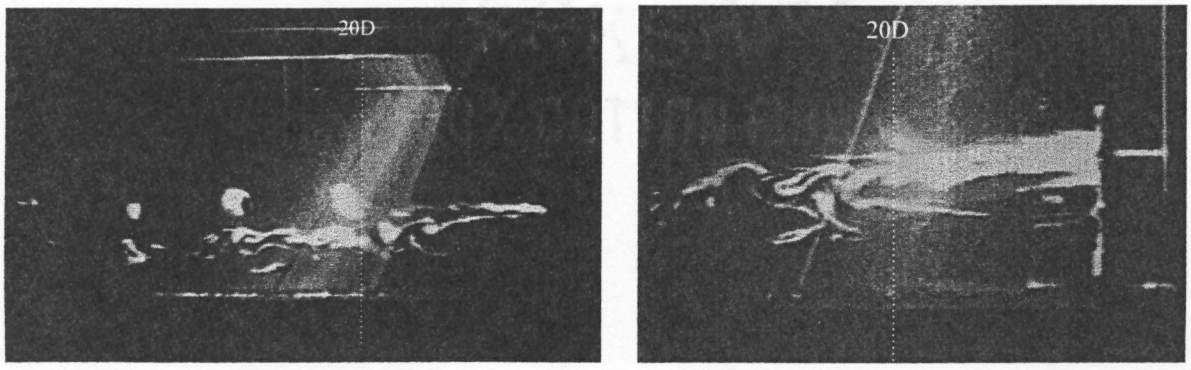


Figure 3-19. Single Grid Dye Injection Point 3 (Baseline left, Modified right) (Re_d=75)

Single Screen Results

Although the flow fields downstream of the single screens were substantially more complicated than the previously discussed single rod and single grid tests article flows, an obvious coherent shedding vortex pattern was identifiable behind the baseline unmodified screen. Concentrations of tight vortices (aligned axially with the transverse surface of the screen) were clearly observed. On the other hand, the modified screen with the 1 inch double helical wrap, showed very randomly organized flow with no obvious coherent vortex shedding structures. The dye pattern downstream also showed significant 3-D mixing. Typical flow visualization comparison results for the three dye injection locations are shown in Figures 3-20, 3-21 and 3-22.

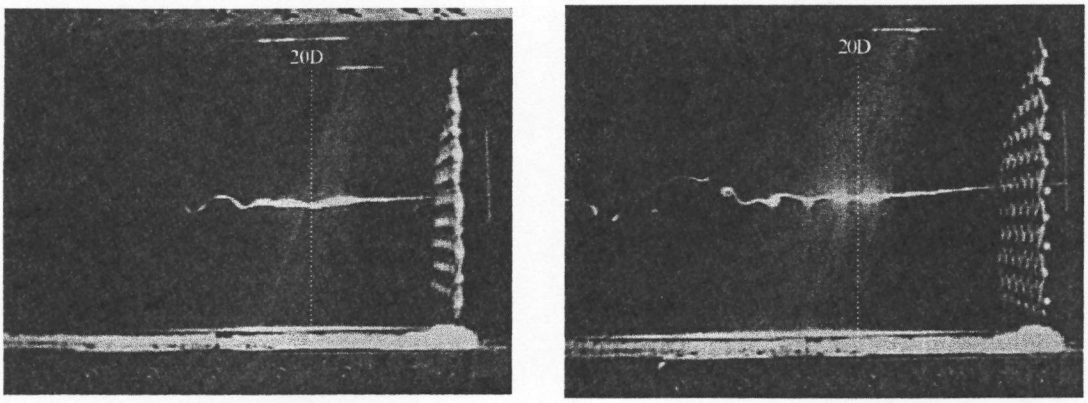


Figure 3-20. Single Screen, Dye Injection Location 1 (Baseline left, Modified right) (Re_d=75)

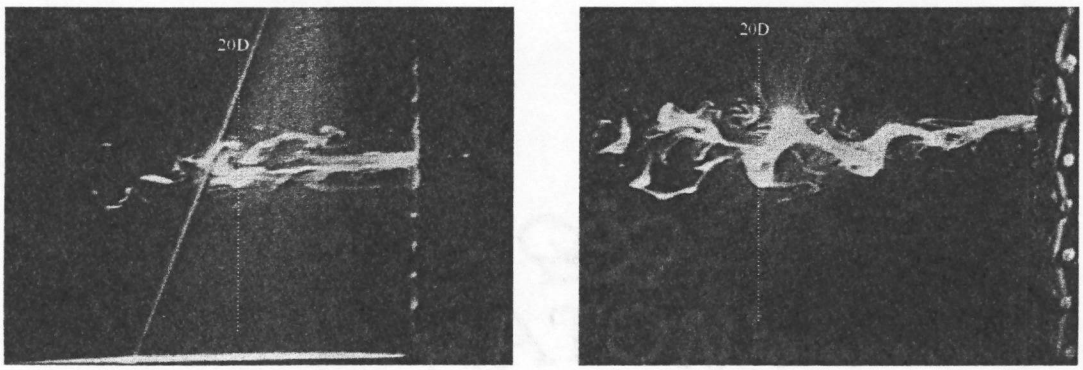


Figure 3-21. Single Screen, Dye Injection Location 2 (Baseline left, Modified right) (Re_d=75)

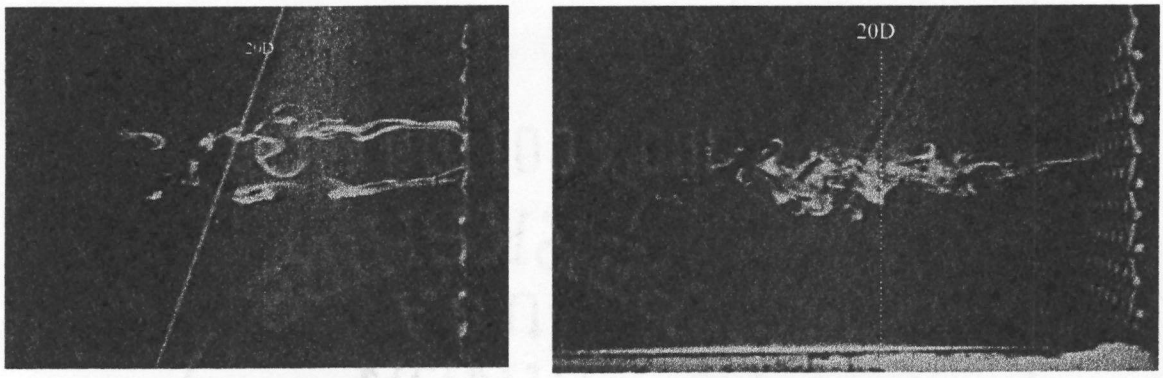


Figure 3-22. Single Screen, Dye Injection Location 3 (Baseline left, Modified right) (Re_d=75)

A direct qualitative comparison of the flow fields downstream of the baseline and modified test articles revealed consistent trends. The helical wrap modification clearly demonstrated more three dimensional mixing in the flows and created less coherent vortex shedding structures. The flow visualization results showed promise for this helical wrap modification and potential turbulence reduction effectiveness using this design. The 1 inch wrap pitch length proved to be the optimum wrap length and the double wrap showed added effectiveness in disorganizing the shedding flow structures. Based on these results, follow-on quantitative flow field measurements were conducted using this 1 inch wrap pattern for the modified single grids and screens.

Chapter 4

FLOW FIELD MEASUREMENT TESTS

Experimental Objectives

The primary objective of the flow field measurement testing was to quantitatively characterize and directly compare the flow fields downstream of the baseline and modified single grids and single screens in order to assess the potential merits of this new screen design for higher Reynolds number turbulence attenuation. The desire was to demonstrate the potential for enhanced turbulence reduction by taking advantage of the added three dimensionality introduced in the flow by the helical wrap modification. The objective was also to provide quantifiable data to support the flow visualization results.

Experimental Set-up and Method

The Test Articles

Single grid testing was conducted using the baseline and single 1 inch wrap test articles prior to the single screen tests. The single grid flow field measurement testing had been conducted prior to the double wrap flow visualization investigation and therefore the single wrap was used. The 1 inch double wrap was subsequently evaluated during the single screen tests.

The Test Facility

The UTSI water tunnel was used for all flow measurement testing. A series of single component velocity measurements using the constant temperature hot film anemometry technique were carried out to characterize the flow fields downstream of the test articles. Refer to Chapter 3 facility description for details on the UTSI Water Tunnel.

General

All quantitative flow field measurements were conducted using the constant temperature hot film anemometry technique. Prior to detailed flow field measurements, accurate hot film calibrations were carried out. Using the accurate probes, the UTSI water tunnel was then calibrated. The acquisition and processing of the single component hot film signal was performed by a TSI IFA100 for the single grid tests which were conducted in July 1996. A more advanced and capable TSI IFA300 system was obtained and used for the follow-on single screen tests in November-December 1996. Accordingly these two test phases will be discussed separately.

Single Grid Testing - Experimental Approach and Instrumentation

The approach for the single grid study was to compare the effective axial velocities at selected locations in a vertical plane 20 diameters downstream of the baseline and modified single grids. Resource limitations restricted this study to a single velocity component (axial) investigation and precluded the resolution of the actual flow velocity into the three dimensional components. Hot film measurements were used to determine the flow velocities by positioning the probe film and supports at a 90 degree angle to the mean axial flow (u component).

A model 1210 Standard Straight DISA Probe was used for the single grid experiments and was calibrated using the IFA-100 Hot film anemometer constant temperature system. The probe was calibrated in the UTSI calibration tow tank using water taken directly from the water tunnel to ensure a representative calibration medium. Specifics regarding the hot film calibrations are provided in Appendix A.

As previously mentioned, the UTSI water tunnel used in this investigation was a dated, closed-loop system. The tunnel was rated for flow velocities ranging from 0.5 inches/sec to 24 inches/sec however the most recent calibration of the tunnel had been performed in 1990 and appeared in these initial experiments to be considerably out of calibration. As a result, the free-stream velocity required for a Reynold's number of 500 for single grid tests was achieved relying solely on the calibrated hot film probe used in these

experiments. The water tunnel was calibrated prior to single screen tests and results are presented in Appendix B.

Probe Oscillation and Free Stream Turbulence Survey. Prior to collecting data in the water tunnel, the free-stream turbulence level was determined at the selected Re_d of 500. At the same time the probe oscillation sensitivity, due to probe stem insertion into the flow, was assessed at three different vertical locations in the water tunnel (at the data collection location). The results of these free-stream surveys are provided in Table 4-1. Data sampled at 1000 hertz for 2 second durations were collected at each vertical location. The average axial velocities, the associated standard deviation of the data, and the calculated turbulence intensities are defined as follows and are tabulated for the three free-stream locations.

The average velocity is defined as:

$$\overline{U} = \frac{1}{N}\sum_{i=1}^{N} u$$

The variance is given by:

$$U' = \frac{1}{N-1}\sum_{i=1}^{N}\left(\overline{U} - u_i\right)^2$$

The standard deviation is given as:

$$\sigma = \sqrt{\frac{1}{N-1}\sum_{i=1}^{N}\left(\overline{U} - u_i\right)^2}$$

The turbulence intensity is defined as:

$$TI = \frac{\sigma}{\overline{U}}$$

All statistical data contained in this document are calculated in accordance with these equations unless otherwise stated.

The raw data for the centerline-flow location (7.00 inches below the test section water surface) is provided in Figure 4-1 and was representative of all three depth locations. Clearly this mid-point demonstrated the lowest turbulence levels with higher intensities at the boundaries of the test section (surface effects and tunnel bottom boundary layer effects).

Table 4-1. Probe Oscillation and Free Stream Turbulence Survey

Probe Depth from water surface	*Average Velocity U*	*Std Deviation σ*	*Turbulence Intensity*
4.75"	2.8926	.0419	0.0145
7.00"	2.8083	.0347	0.0124
9.25"	2.827	.0380	0.0135

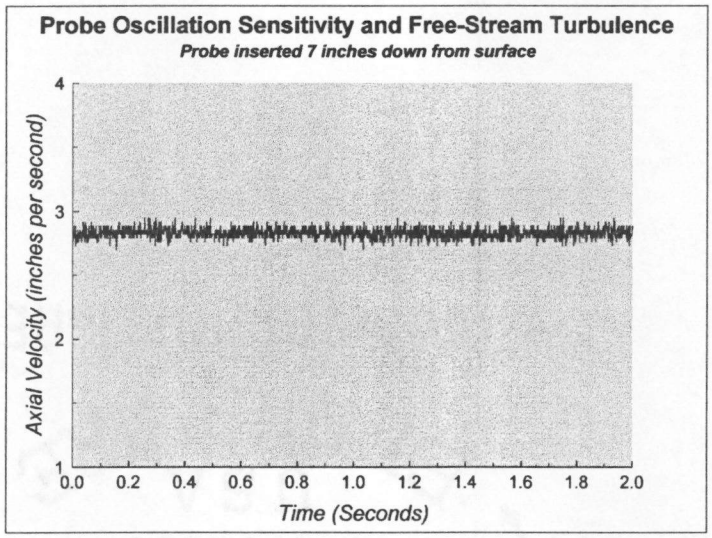


Figure 4-1. Probe Oscillation Sensitivity
and Free-Stream Turbulence Data

The screen base assembly was positioned on the tunnel bottom which put the flow location for this investigation approximately at the 9.25 inch location. Therefore the free-stream turbulence intensity level of 0.0135 (or 1.35%) was accepted at the free-stream turbulence intensity for these tests. No probe oscillations were observed at any time during testing.

Probe Mount and Traversing System. A special probe mount and traversing mechanism was manufactured to accurately position the hot film at repeatable locations in the flow

downstream of both test models to ensure direct comparisons of test results. A close-up of the single grid test model set-up in the water tunnel is provided in Figure 4-2.

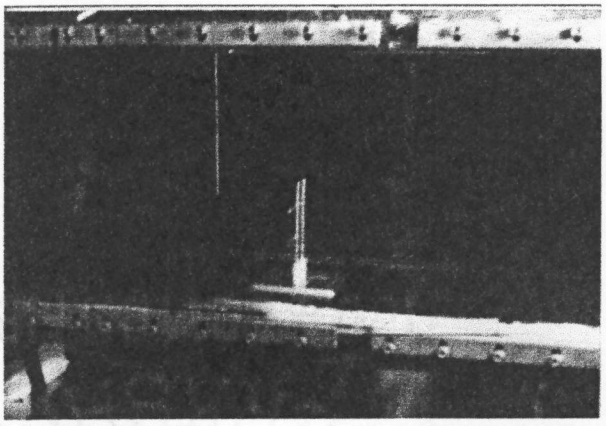


Figure 4-2. Single Grid Test Model in Water Tunnel

Single Grid Tests Conducted. Time and local axial velocity measurements were recorded at nine locations in a vertical plane (oriented parallel to the grid) positioned 20 screen diameters (or 5 inches) down-stream of the test grid models. Each axial velocity measurement was taken at a sampling frequency of 1000 cycles per second (Hz) for a two second duration. The specific data collection locations and test point numbering method and sequencing is provided in Figure 4-3. Once the water tunnel flow velocity had been adjusted for the desired operating condition, testing was completed for both grids to ensure identical free-stream flow conditions.

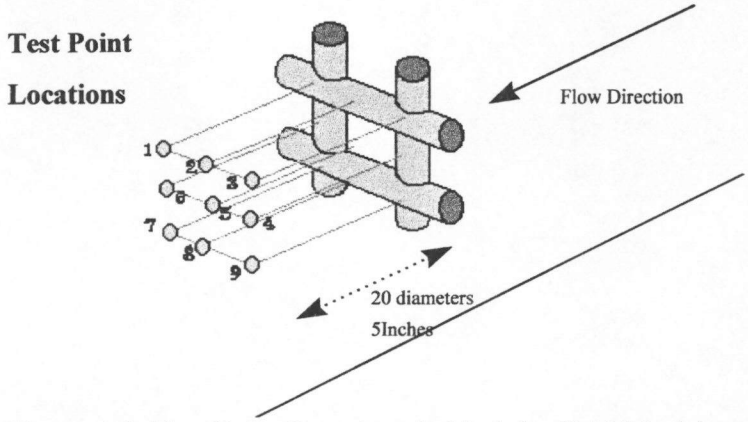


Figure 4-3. Test Point Locations behind the Grid Models

The vortex shedding phenomenon for flows around a cylinder is characterized by Reynolds number and Strouhal number.

$$\mathrm{Re}_d = \frac{\rho U_\infty d}{\mu} = \frac{U_\infty d}{\nu} \qquad St = \frac{fd}{\overline{U_\infty}}$$

For flow around cylinders at Re_d greater than 600, the Strouhal number is relatively constant at approximately 0.2. However for low Reynolds number flows (<600), the Strouhal number becomes dependent on Re_d. In this case (Re_d =500) the Strouhal number is approximately 0.18. Vortex shedding at a frequency of approximately 2 Hz was therefore anticipated for the unmodified grids (d=0.25 inches, $\overline{U_\infty}$ =2.88 inches/sec).

The test location of 20 diameters down-stream was selected due to physical setup constraints. There was also a concern that results further down-stream (100 to 200 diameters) may become dominated by tunnel free stream effects and boundary layer effects associated with the tank bottom surface. The 20 diameter downstream location was ultimately selected for these reasons. Testing in the 100 to 200 diameters downstream region (where the vortex shedding has decayed) to measure the absolute turbulence intensity reduction effectiveness was investigated during follow-on single screen testing.

Single Screen Testing - Experimental Approach and Instrumentation

The approach for the single screen study was to compare the effective axial and lateral velocities at selected locations in a vertical plane positioned 20, 100 and 192 rod diameters downstream of the baseline and modified screens. Resource limitations again restricted this study to a single velocity component investigation (axial and lateral) and precluded the resolution of the flow velocities into the actual three dimensional components. In this case both the axial and lateral velocities were independently measured. Hot film measurements were used to determine the flow velocities by positioning the probe film and supports at 90 degrees to the axial mean flow to measure the u component and aligning the probe film and supports with the axial mean flow to measure the w component. Specifics regarding the hot film calibrations are provided in Appendix A. A side view of the single screen test set-up in the water tunnel is provided in Figure 4-4.

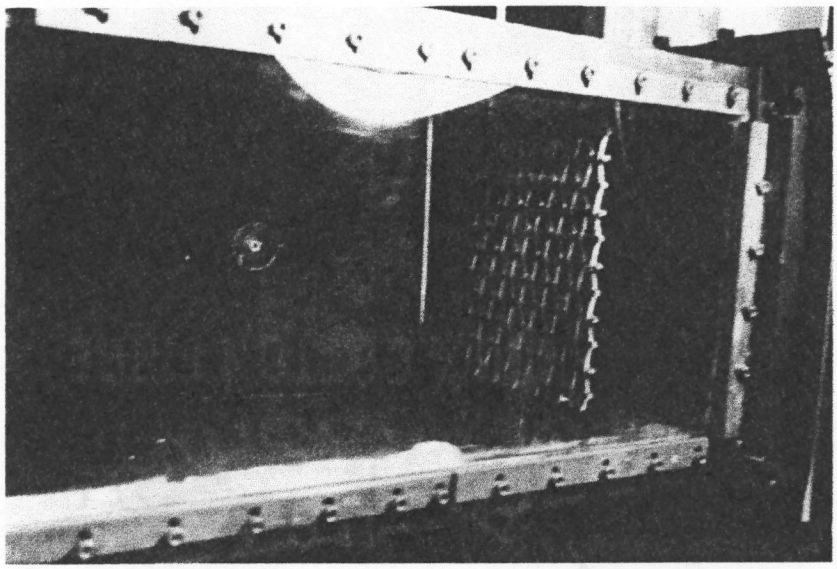


Figure 4-4. Single Screen Test Set-up Side View

Probe Mount and Traversing System. The same probe mount and traversing system and technique used during the single grid testing was employed for the single screen testing. A close-up of the probe mount and traversing system used for all testing is shown below in Figure 4-5.

A schematic of the test set-up is provided in Figure 4-6 which shows the addition of an upstream reference probe. The probe was installed to measure the up-stream, incoming flow to account for the unsteadiness in the mean axial flow observed during the flow

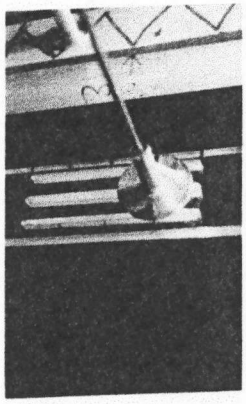


Figure 4-5. Hot Film Probe Mount and Traversing System

visualization phase. If an obvious change in the mean flow was measured, this data was discarded and the test point was repeated to ensure comparable flow conditions.

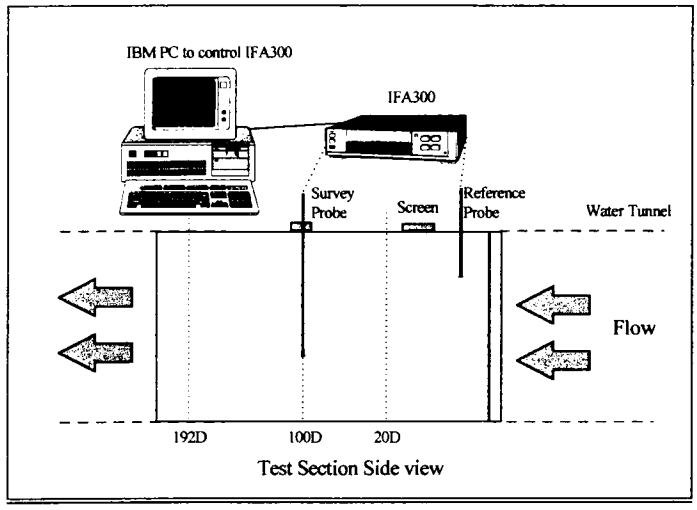


Figure 4-6. Single Screen Set-up Schematic

Single Screen Tests Conducted. Time and axial (u)and lateral (w) velocity measurements were recorded at five locations in a vertical plane (oriented parallel to the screen and perpendicular to the mean flow direction) positioned 20, 100 and 192 rod diameters (or 5, 25 and 48 inches) down-stream of the test screen models. Figure 4-6 shows an upstream view of the test screen with the probe positioned at the center location (TP3) and the test point collection area is highlighted with a white square (TPs 1, 2, 4, and 5 at the corners). Each velocity measurement was taken at a sampling frequency of 2000 cycles per second (Hz) for a two second duration. Figure 4-7 shows an upstream view of the single screen positioned in the water tunnel. The test point locations at each of the axial stations were oriented much the same as that shown in Figure 4-3 for the single grids. The pattern however, was centrally located with respect to the screen and data was only collected at the outer corners and center location (grid locations 1, 3, 5, 7, 9 as per Figure 4-3 and are referred to as screen locations 1, 2, 3, 4, and 5 respectively). Data were collected for two Reynold numbers (75 and 600). Note that the test screens did not fully enclose the water tunnel test cross-section. This allowed for flow around the screens creating added non-uniformities in the velocity profiles downstream. To minimize these influences, data collection was restricted to the center

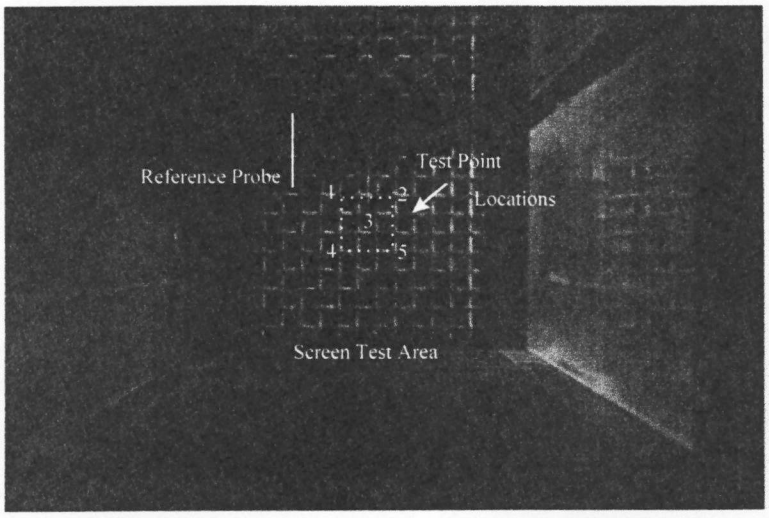


Figure 4-7. Screen Test Point Area as seen through upstream view

portion of the screens. The test point numbering sequence is shown and the reference upstream probe position is illustrated as well. Once the water tunnel flow velocity had been adjusted for the desired operating condition, testing was completed for both screens at a single axial station (ie. 20 diameters downstream) to ensure identical flow conditions for the baseline and modified configurations.

Flow Measurement Study - Results and Analysis

The results of the flow field velocity measurement study are presented herein. Specifically, a comparison of the mean axial velocities, the standard deviation of the velocities and the calculated turbulence intensities is made. Analysis was conducted for each of the test points and then averaged for a general flow comparison. Frequency spectra data were obtained for each test point using the Fast Fourier Transform (FFT) technique. As well, statistical analysis on each velocity profile for each two second duration test point was conducted. All single grid results are provided in Appendix C and single screen results are presented in Appendix D. The grid and screen results and analysis will be discussed each in turn using results selected test points which are representative of the collected data.

Single Grid Results and Analysis

Single Grid Statistical Analysis of Axial Velocities. Two sample plots of the axial velocity profiles at location 5 behind the baseline and modified grid models are presented in Figure 4-8. Velocity statistics using the 2 second (1000 Hz) samples were generated for each test point, with particular attention given to the average axial velocity, the associated standard deviation of the average velocity data and the average calculated turbulence intensity. Fast Fourier Transform analysis was also conducted for each point to determine the frequency content in the flow.

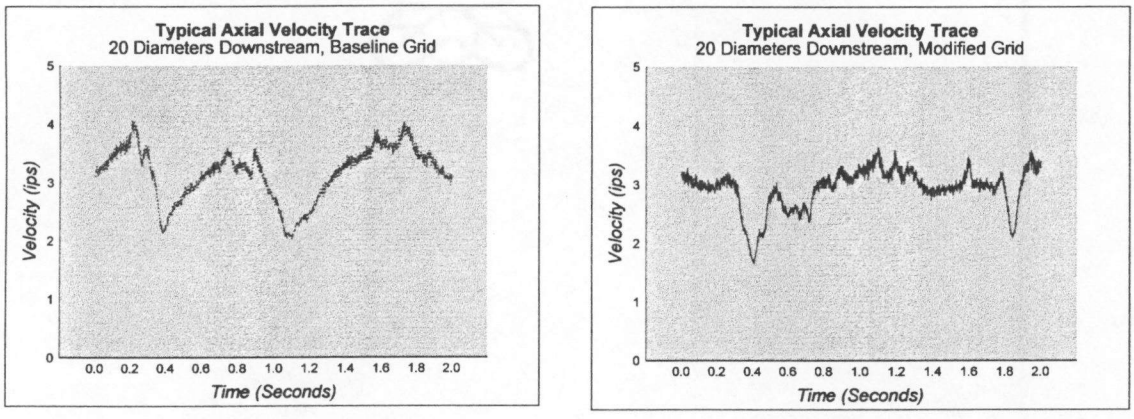


Figure 4-8. Axial Velocity Profiles at Center location 20D Downstream of Single Grids

As a specific example, the statistical data for Test Point 5 (TP 5)are summarized below in Table 4-2. The results of TP 5 (center point of the grid) were generally representative of all test points evaluated and demonstrated similar trends in the flow fields behind the two grid models. These specific results were selected for detailed analysis and discussion primarily because the flow field measured at this centralized location should be dominated by the single grids. TP 5 results should therefore be more representative of the grid influenced flow for comparison between the baseline and modified grids. The average velocity, standard deviation and turbulence intensity behind the modified grid were consistently slightly lower when compared to the same baseline grid flow data.

Table 4-2. Single Grid Test Point 5 Statistical Summary

Statistics TP5	*Avg Velocity U (inches/sec)*	*Std Dec σ*	*Turbulence Intensity*	*Frequency Content*
Baseline Grid	3.16	0.4569	0.1446	1.6Hz/0.16amp 5Hz/0.03amp 10Hz/0.02amp 0.5Hz/0.095amp
Modified Grid	2.93	0.3514	0.1199	3.0Hz/0.035amp 5.0Hz/0.05amp 10Hz/0.02amp

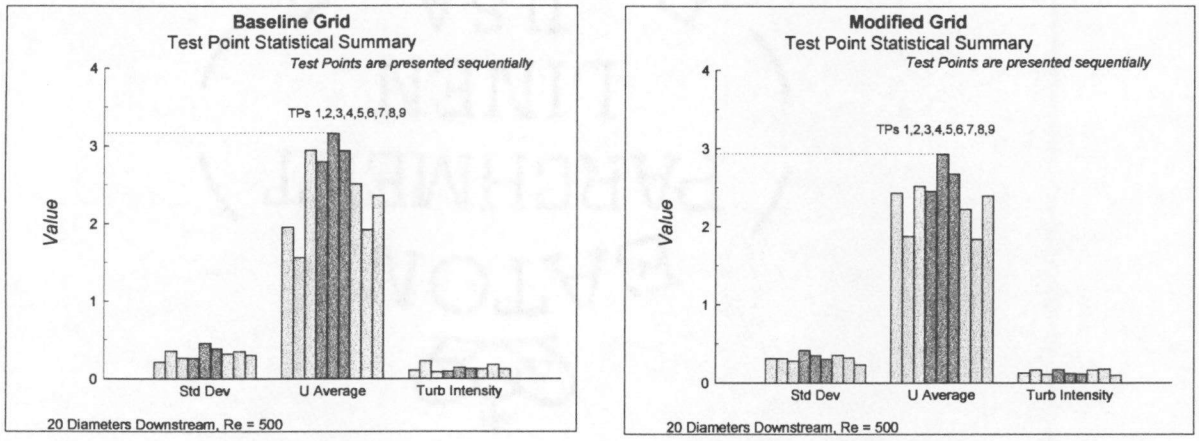


Figure 4-9. Single Grid Test Point Axial Velocity Statistical Comparison

A summary of the statistics for each of the nine test points is shown in Figure 4-9 with baseline grid data shown on the left and modified grid data shown on the right. The results are for each grid test location (1-9), presented from left to right in the bar chart. A plot of the averages of the statistical data for the nine test points is shown in Figure 4-10. This shows the trend at this downstream location of slightly reduced statistical flow parameters behind the modified grid. The flow trends are very similar and the differences, although small, are consistent.

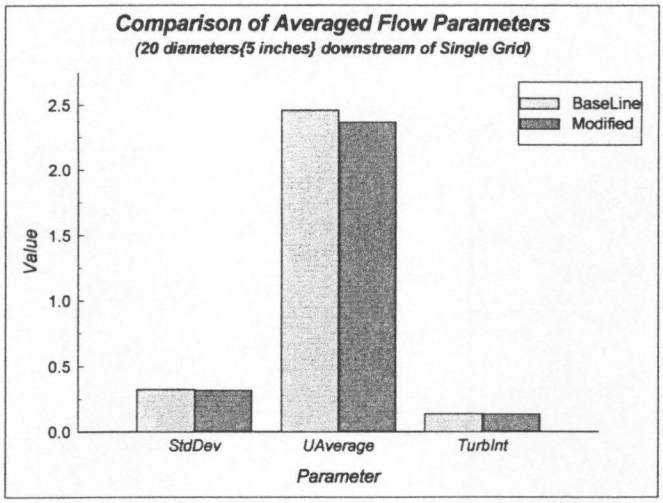


Figure 4-10. Single Grid Average Statistical Comparison

Single Grid 3-Dimensional Analysis. Figures 4-11 and 4-12 provide three dimensional surface plots showing the comparison between the average axial velocity profiles and axial turbulence intensity profiles downstream of the two grids.

The 3-D average velocity profile plots show similar general velocity shapes throughout the flow plane (XY plane), however, the modified screen demonstrated an overall lower velocity level with less pronounced gradients. This showed lower kinetic energy in the flow and less coherence within the shedding vortices behind the modified grid.

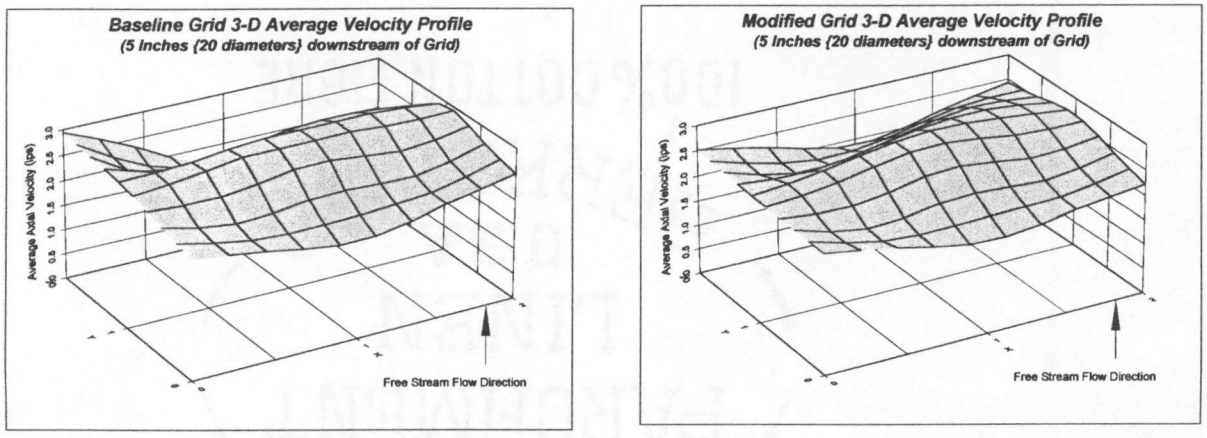


Figure 4-11. 3-D Velocity Profiles in the vertical plane 5 inches downstream of Single Grids

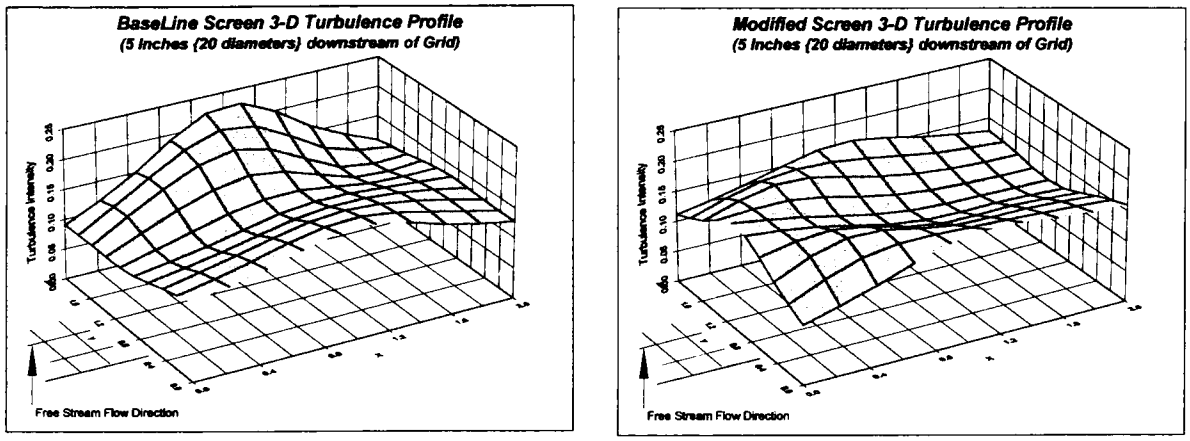


Figure 4-12. 3-D Turbulence Intensity Profiles in the vertical plane 5 inches downstream of Single Grids

Although the data trends were consistent during these single grid experiments, the overall differences between the two screens were very small. The 3-D turbulence profile plots show somewhat different patterns when comparing the flows. The trend of reduced averaged turbulence intensity with smaller gradients is evident with the modified grid. The extra waviness in the modified grid turbulence intensity profile is likely evidence of the additional frequency content in the flow.

Single Grid Frequency Analysis. The baseline frequency data clearly demonstrate the anticipated vortex shedding at approximately 2.0 Hz, in accordance with the Strouhal parameter prediction for cylindrical bodies. The harmonics at higher frequencies (5 and 10 Hz) with decaying amplitude are also evident in the Fast Fourier Transform (FFT) analysis. The frequency content data, however, in the modified screen flow sample reveal a lowering of this vortex shedding frequency to approximately 0.5 with a substantial amplitude decrease (almost 50% reduction) for this lowest frequency oscillation.

At the same time several additional frequency spikes in the flow (at relatively smaller amplitudes) are likely the harmonics of this lower frequency vortex shedding. The frequency spectra for the flows behind the screens is presented for TP 5 in Figure 4-13. These frequency content and amplitude trends were generally typical of the other single grid test point data collected.

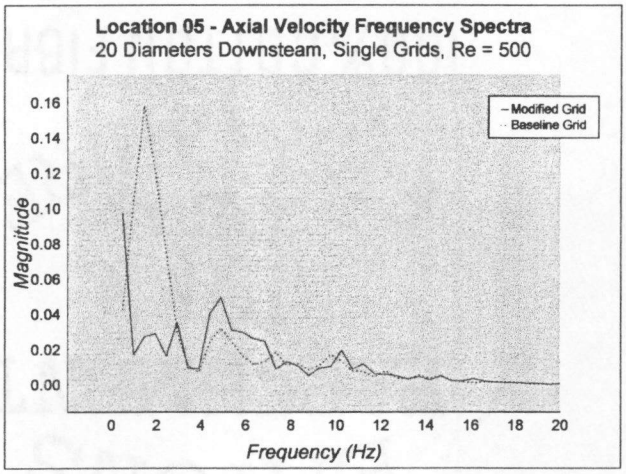


Figure 4-13. Single Grid Frequency Plots for Test Point 5

Single Screen Results and Analysis

The single screen testing was conducted for two Reynold numbers (75 and 600). The low Reynolds number data had been collected in November when dramatically varying outside air temperatures (typically varying with a net change as much as 40 to 50 °F over a 24 hour period) adversely impacted the quality of the collected data. More than 50% of the UTSI water tunnel system, including the water storage tank, was located external to the water tunnel building (refer to Figures 3-5 and 3-6), exposed to outside environmental conditions. In addition, the water tunnel ducting was of a metal construction, which highly conducted any outside temperature gradients. Despite efforts to control the water temperature using heating coils and lengthy periods of water mixing at high flow velocities, an isotropic, homogeneous fluid could not be maintained during the low Re testing. The constant temperature hot film technique was adversely impacted as it required a stable fluid medium (refer to Appendix A for Hot Film Calibration specifics). The velocity data showed erratic, unsteady large velocity fluctuations that were clearly a result of temperature gradients in the water . Water temperature fluctuations as large as 2 degrees were measured during the two second data samples. These could not be resolved from the actual flow fields induced by the test articles. Accordingly, the low Re data was deemed unsuitable for this investigation and is not reported herein.

The higher Re testing was conducted on three separate occasions during milder outdoor temperature periods. On 18 December 1996, suitable conditions permitted the acquisition of axial and lateral single screen velocity data which is discussed below.

Statistical Analysis of Velocities. Two sample plots of the axial velocity profiles at location 2, 20 diameters downstream of the baseline and modified (double wrap) single screen models are presented in Figure 4-14. Velocity statistics using the 2 second (2000 Hz) samples were generated for each test point, with particular attention given to the average axial velocity, the associated standard deviation of the velocity data, and the calculated turbulence intensity.

The velocity traces show a much more complicated flow pattern when compared to the comparable single grid plots. The upstream reference velocity was measured for each point to help ensure stable and similar water tunnel test conditions and is shown as the steady dark gray line. Trends are less noticeable in these plots however the lower average velocity behind the modified screen is noticeable compared to the constant upstream reference velocity.

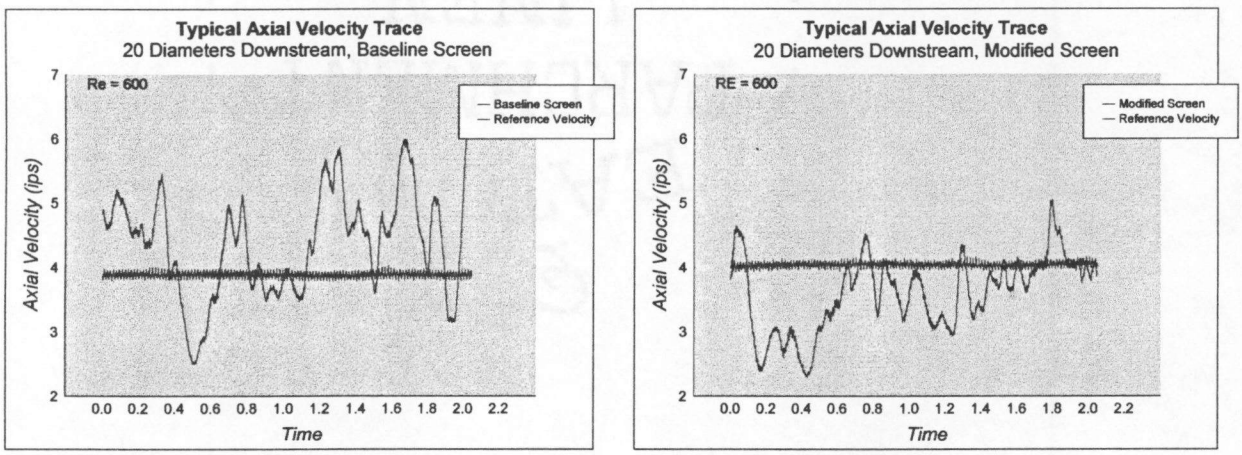


Figure 4-14. Typical Axial Velocity Profiles 20 Diameters Downstream of Single Screens Re=600 (Test Point 2)

As a specific comparison, the statistical data for the single screen Test Point 2 data are summarized in Table 4-3. Again, these results were generally representative of all test points evaluated and demonstrated similar trends in the flow fields behind the two screen models. The average velocity, standard deviation and turbulence intensity behind the modified screen were consistently slightly lower when compared to the same baseline screen flow data.

Table 4-4. Screen, Single Point Axial Velocity Statistical Summary (20D)

Statistics Test Point 02	*Avg Axial Velocity (u)*	*Std Dev σ*	*Turbulence Intensity*
Baseline Screen	4.3812 ips	0.8018	0.1481
Modified Screen	3.5487 ips	0.5740	0.1337

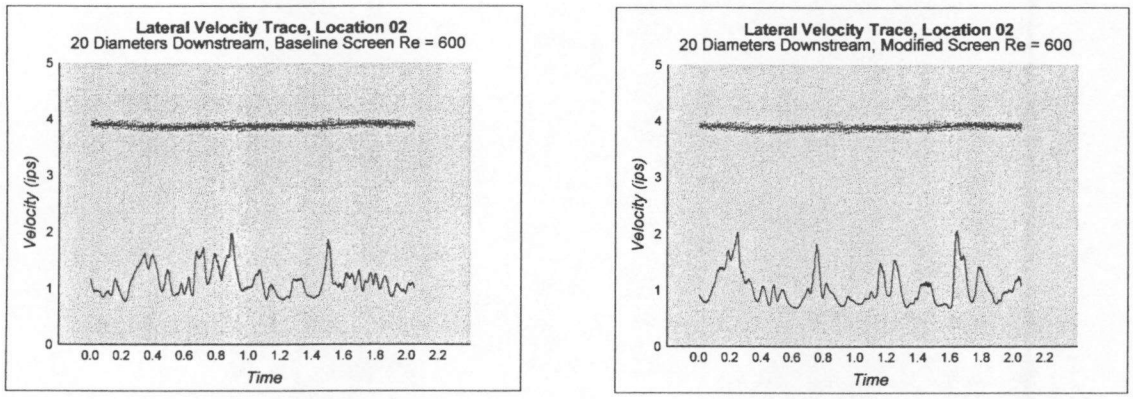


Figure 4-15. Typical Lateral Velocity Profiles 20 Diameters Downstream of Single Screens Re=600 (TP 2)

The lateral velocity traces for Test Point 2 data are provided in Figure 4-15. The reference upstream velocity (approximately 4 ips) are shown by the constant gray line.

The lateral velocity statistics associated with Figure 4-14 data are presented in Table 4-5 and show the trend of lower average lateral velocity behind the modified screen at the 20 diameter downstream location.

Table 4-5. Screen, Single Point Lateral Velocity Statistical Summary (20D)

Statistics Test Point 02	*Avg Lateral Velocity (w)*	*Std Dev σ*	*Turbulence Intensity*
Baseline Screen	1.1241 (ips)	0.2384	0.1673
Modified Screen	1.0329 (ips)	0.2934	0.2230

Contrary to the axial velocity data, however, the standard deviation of the data and the calculated lateral turbulence intensity are greater behind the modified screen. These findings conform nicely with the enhanced lateral flow mixing (3-D) which is expected as a result of the wrap.

A summary of the axial and lateral velocity statistics, using all collected data points, is provided in Figure 4-16 for the 20 diameter downstream location. The axial TI data is illustrated with the white bars and the lateral TI data with gray bars. The modified screen data is depicted with the cross-hatch pattern in contrast to the baseline data with no fill pattern.

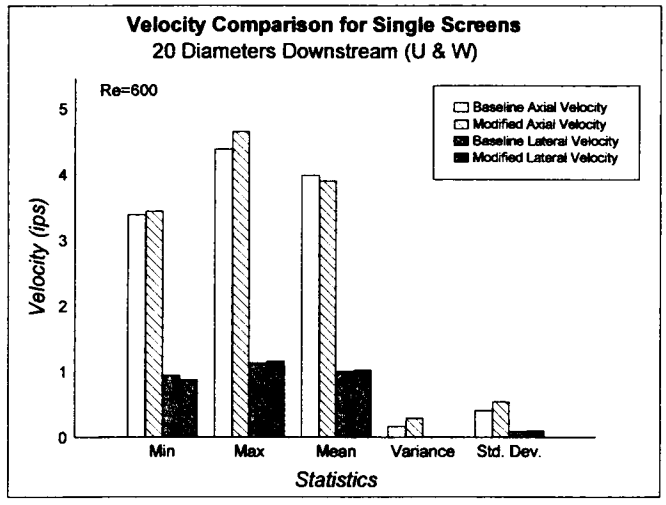


Figure 4-16. Axial and Lateral Velocity Statistics
for all Single Screen Data at 20 Diameters Downstream

Raw axial and lateral velocity traces for all test points are included in Appendix D. Statistical summaries for the 100 and 192 diameter downstream locations are provided in Figure D-36. The calculated axial velocity statistics in Figure D-36 for the modified screen reveal a trend of reduced mean velocities which persist at the downstream locations. Interestingly, despite an initial lateral velocity increase at the 20D location, the downstream data (100 and 192 D) show a consistent lowering of the mean lateral velocity in the flow behind the modified screen.

Screen Turbulence Intensity Analysis. The axial velocity trace data were also processed for instantaneous turbulence intensity (TI)values. The resulting TI plots for each test point are presented in Appendix D (Figures D-11 through D-15). Test Point 2 results at the 20 D location are shown in Figure 4-17. Generally at all downstream locations, no significant differences in the axial velocity TI plots for the baseline and modified screens are noticeable based on the raw TI traces.

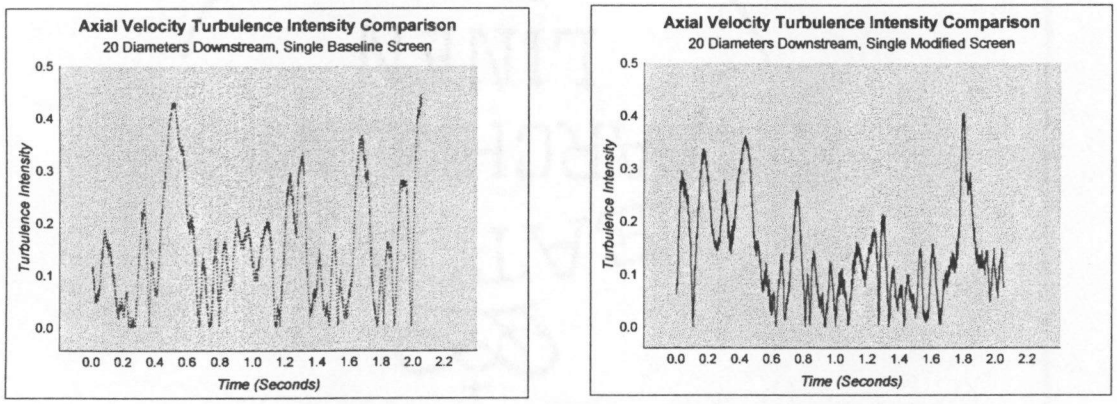


Figure 4-17. Single Screen Axial Turbulence Intensity Traces
Location 2, 20 Diameters Downstream

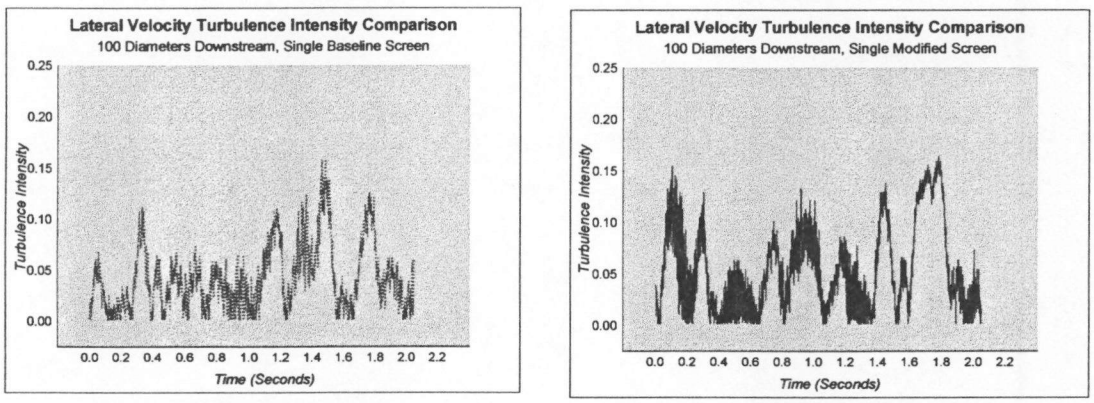


Figure 4-18. Single Screen Lateral Turbulence Intensity Traces
Location 2, 100 Diameters Downstream

The lateral TI traces for each test point conducted at all downstream locations are presented in Appendix D. Generally, a consistent increase in lateral TI behind the modified screen at all axial locations is evident. TP 2 data at the 100D location is highlighted in Figure 4-18 as a typical example.

A bar graph of the axial and lateral TI statistical data for the five test points collected behind the single screens at the 20 diameter axial location is presented in Figure 4-19. Appendix D (Figure D-37) contains the 100 and 192 diameter downstream data. This shows the trend of slightly reduced axial TI (u component) statistical parameters behind the modified screen. The axial TI trends are strikingly similar when compared to those presented for the single grid.

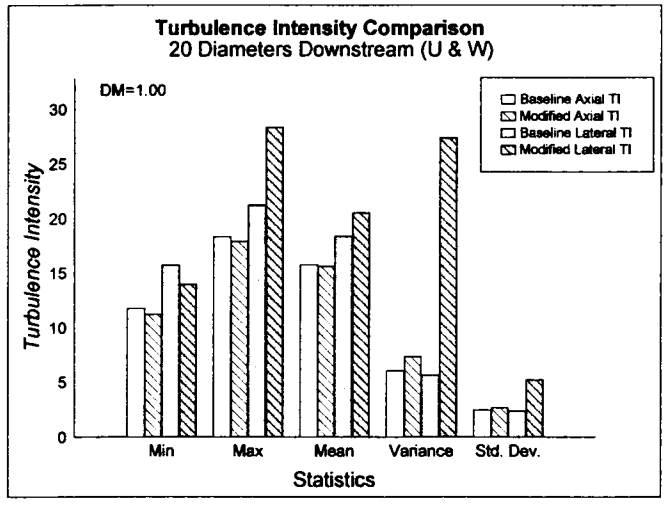


Figure 4-19. Single Screen Average TI Statistical Comparison at 20d (top left), 100d (top right), and 192d (bottom) downstream

In contrast, the lateral TI trends characterized by the calculated statistical parameters reveal a significant increase in the mean lateral TI and substantially more variance in the TI values behind the modified screen. This apparent increase deserves further analysis. Recall that the instantaneous calculation of the turbulence intensity values for these 2 second traces are based on the classical formula;

$$TI = \frac{\sqrt{(\overline{U} - u_i)^2}}{\overline{U}}$$

where $\overline{U}$ is the average velocity of the 2 second sample and u_i is the instantaneous velocity. In fact, there are two $\overline{U}$ values, one for each modified screen and one for each baseline screen data sample. As already discussed, the modified screen consistently demonstrated a lower average velocity at all test points conducted (all axial and downstream lateral) and accordingly the modified screen TI values are somewhat artificially high for direct

comparison purposes between the two screens. This difference is slight at most for the higher axial turbulence data however for the lateral velocity data this effect is dramatic. The fact that the average lateral velocity (disregarding the initial 20D temporary increase) behind the modified screen is consistently lower compared to the baseline screen is in itself an improvement in the uniform axial flow. To demonstrate a more relevant direct comparison between the lateral TI's, the baseline screen average velocity $\overline{U}$ is used in the denominator in the calculation of both the baseline and modified screen TI plot values as follows;

$$TI_{Baseline} = \frac{\sqrt{(\overline{U}_{Baseline} - u_i)^2}}{\overline{U}_{Baseline}} \qquad TI_{Modified} = \frac{\sqrt{(\overline{U}_{Modified} - u_i)^2}}{\overline{U}_{Baseline}}$$

The two resulting plots are shown in Figure 4-18 for Test Point 2 data at the 100 diameter downstream location. Using the same denominator value permits the direct comparison of the actual lateral TI reduction using the modified screen. The reduction in TI is clearly demonstrated in Figure 4-20 with the horizontal reference line.

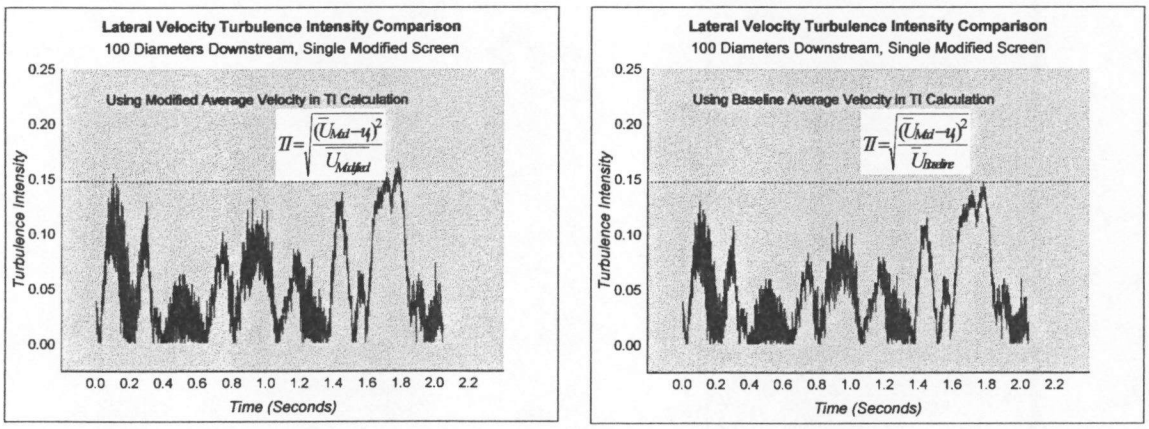


Figure 4-20. Turbulence Intensity Plots showing the effect of lower mean velocity behind the modified screen

The entire trace has shifted slightly downward (lower TI) because of the larger $\overline{U}_{Baseline}$ denominator. This "comparison corrected" technique has been used here in order to better compare the baseline and modified screen lateral turbulence intensities. The TI plots contained in Appendix D (Figures D-11 through D-15, D-21 through D25 and D-31 through D35) are all generated using the classical average velocity denominator value as per the accepted TI definition (not "comparison corrected"). Accordingly, it is important to

recognize that the modified screen data TI values are based on consistently lower mean lateral and axial velocity values, giving them relatively higher TI values.

In general, the modified screen data generally shows a marginally lower axial turbulence intensity profile than the baseline screen. The lateral TI values appear consistently higher behind the modified screen when calculated as a fraction of the mean lateral velocity ($\overline{U}_{\text{Modified}}$)at the test point locations. Because there is an overall lowering of the lateral velocity at downstream locations, the net effective lateral TI is lower than presented in Appendix D. In actuality, the lateral TI behind the modified screen is comparable to or slightly lower than the baseline screen when a direct, relevant comparison is made.

3-Dimensional Analysis of Screens. The 3-D analysis was completed for the single screens using five test points only. As such, only limited value in the analysis of this data is possible. The mean axial velocity plots are illustrated in Figure 4-21 for the 20 diameter

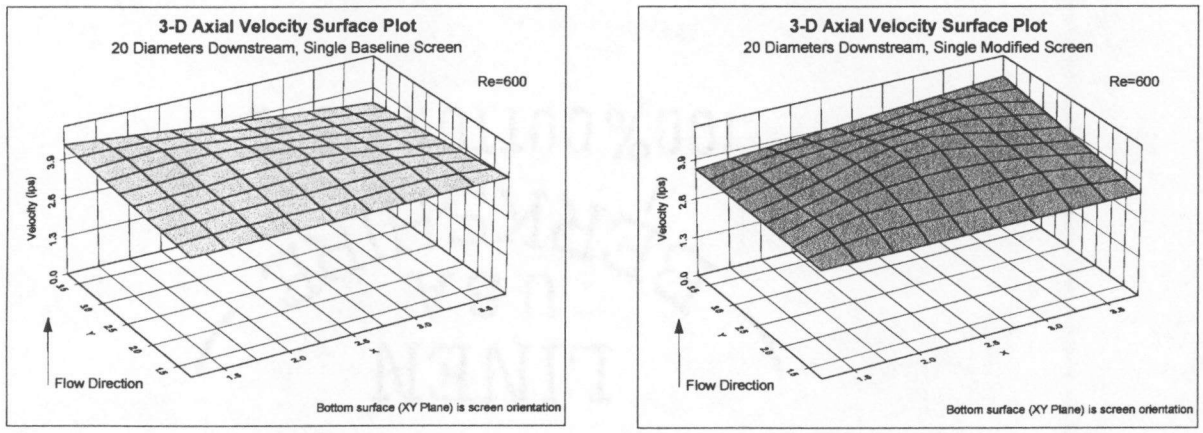


Figure 4-21. Axial Velocity Surface Plot
20 Diameters downstream of Single Screens

downstream location. The modified screen data appears to have greater axial velocity gradients based on the 3-D illustration and the statistical data. These gradients are more quickly broken down to a uniform axial velocity distribution behind the modified screen as is evident in the 100 and 192 diameter downstream data illustrated in Figure D-38.

The axial turbulence intensity surface plot in Figure 4-22 suggests slightly stronger gradients downstream of the modified screen. Again, the trends behind both screens are similar and any differences are very small. It is interesting to note that the patterns are much the same with the smallest turbulence intensity occurring at the center test point.

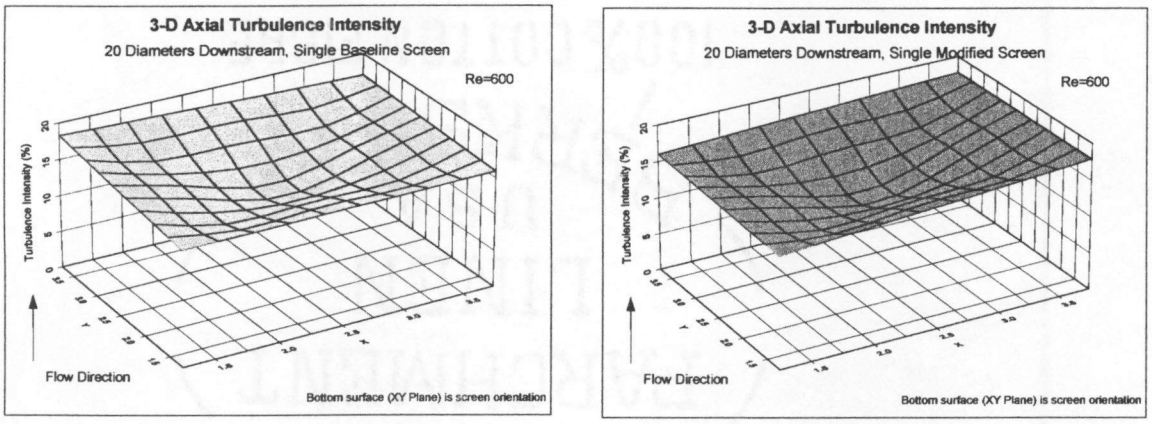


Figure 4-22. Axial Turbulence Intensity Surface Plot
20 Diameters downstream of Single Screens

Figure D-39 in the appendix presents the 100 and 192 diameter downstream plots which further demonstrate these trends.

Screen Frequency Analysis. All axial and lateral velocity frequency spectra plots are contained in Appendix D (Figures D-1 through D-10). As an example, the frequency spectra associated with the axial velocity data collected at Test Point 2, 20 diameters downstream of the screens is presented in Figure 4-23 for detailed analysis. This data was generally representative of all test locations. The baseline and modified screen data are superimposed in one plot for a more obvious comparison. The left plot in Figure 4-23 reveals the predominant frequency content of the flow in the 0 to 20 hertz frequency range (similar to the single grid data). The 0 to 20 hertz range (critical data) is magnified in the right plot in Figure 4-23. Again, a shift in frequency is evident behind the modified screen and an increase in the distinct frequency content is apparent. This increased frequency content is the predominant characteristic distinguishing the modified screen from the baseline screen. The amplitudes of the axial velocity frequencies behind the modified screen also show

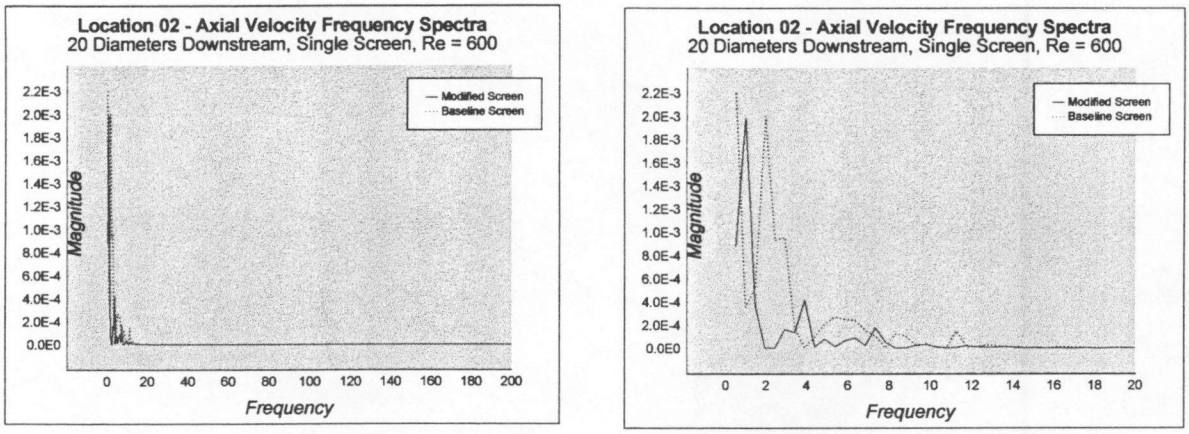


Figure 4-23. Axial Velocity Frequency Spectrum Plots 20 Diameters Downstream of Screens (0 to 200 Hz left, 1-20 Hz right)

a reduction as compared to the baseline plot. This characteristic appears to be the key contributor to the resulting lower axial turbulence intensity behind the modified screen. These results are surprisingly similar to the single grid results. These same general trends are apparent at the other test locations and differences are most likely attributable to the non-uniform structures of the test screens.

The lateral velocity frequency spectra plots at location 2 are shown in Figure 4-24. A slight increase in the distinct frequency content is observed behind the modified screen however, unlike the axial frequency data, an increase in the amplitudes occurs. These results

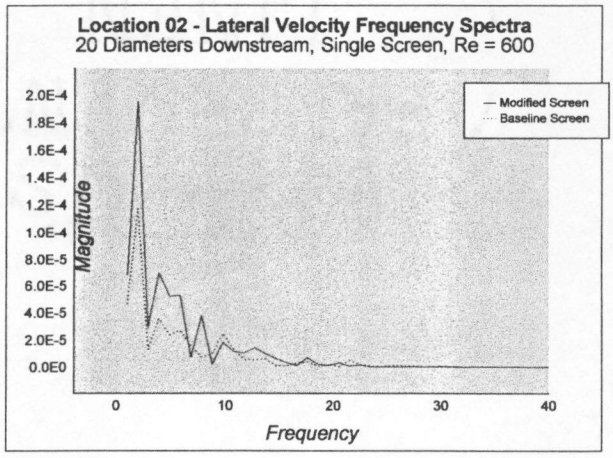


Figure 4-24. Lateral Velocity Frequency Spectrum Plots 20 Diameters Downstream of Screens (0 to 20 Htz)

are consistent with the increased lateral turbulence intensities measured downstream of the modified screens (100 and 192 diameter locations). This is most likely a direct result of the added 3-D mixing created by the wrap which is most apparent in the lateral direction.

Screen Turbulence Attenuation. The mean axial turbulence intensity values are plotted in Figure 4-25 as a function of distance downstream of the screens, showing the net influence of the screen modification. The values plotted are the averages of all test points collected at each axial location using the traditional TI calculation as well as the "comparison correction" technique for the modified screen.

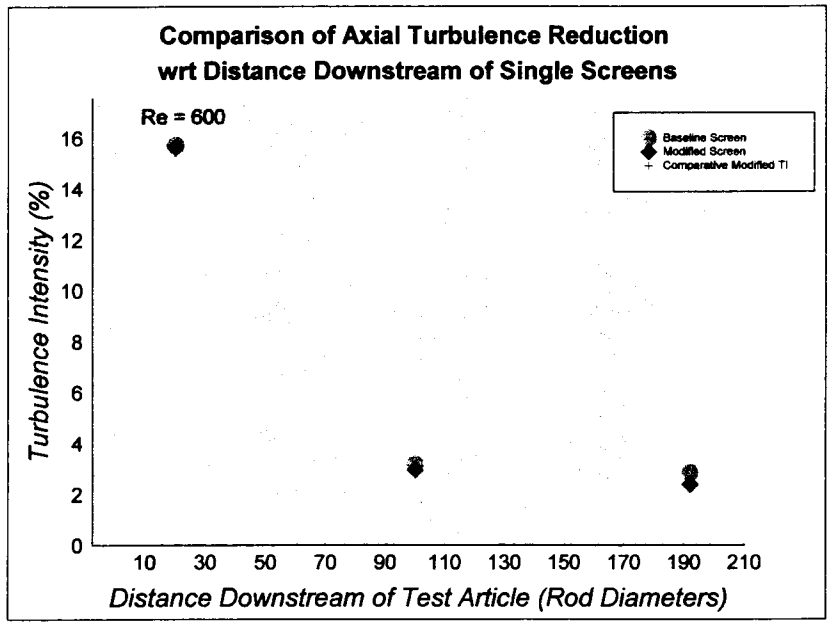


Figure 4-25. Axial Turbulence Intensity Profiles downstream of Single Screens

The data shows a slight reduction in axial TI behind the modified screen, but only beyond the 100 diameter location. The apparent increased attenuation for the modified screen supports the enhanced three dimensional flow breakdown observed during flow visualization and manifested in a more uniform axial velocity distribution downstream. The modified attenuation points using TI values calculated using the comparative equation ($\overline{U}_{\text{Baseline}}$ "comparison corrected") are also plotted and show very little improvement over the classically derived modified screen TI plot.

The stream-wise attenuation characteristics of the lateral velocity turbulence intensity are shown in Figure 4.26. The modified screen data initially shows a dramatic increase in the lateral TI properties at the 20 diameter downstream location, which is expected with the added 3-D mixing created by the helical wrap. The attenuation is also more effective (greater attenuation slope) behind the modified screen showing a final, lateral TI at the 192 diameter downstream location practically identical to the baseline screen. The differences are slight, but the trends are noticeable and support the flow visualization data. These results also conform with the anticipated flow physics created by the wrap modification.

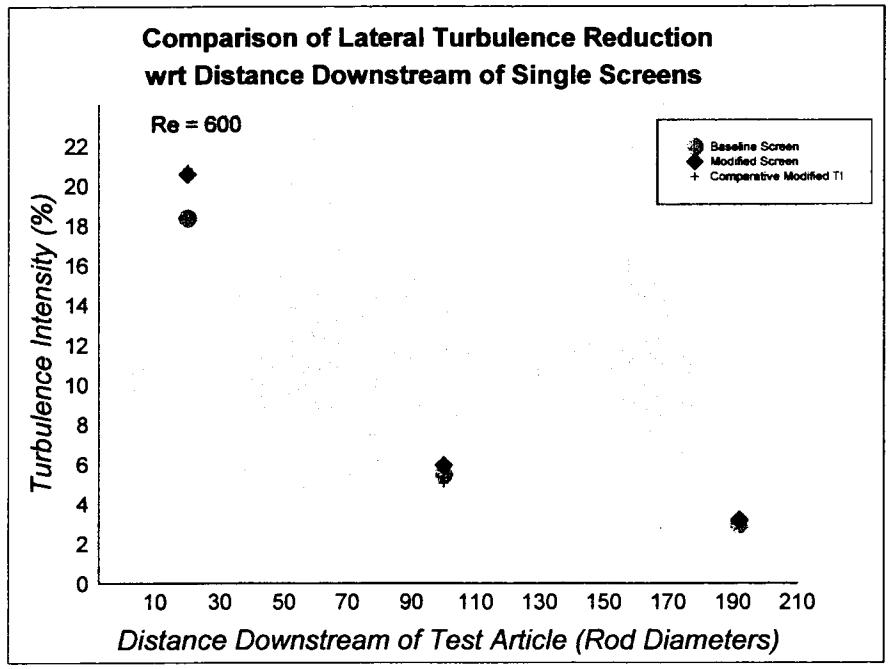


Figure 4-26. Lateral Turbulence Intensity Profiles
Downstream of Single Screens

Again the reference velocity corrected TI plot is shown for the modified screen with the dark dashed dashed points. Here the effects of the lower mean lateral velocity behind the modified screen become much more apparent. Using this "comparison corrected" data, the modified screen shows significantly improved TI attenuation with a steeper drop-off (slope) and lower final TI value at the 192 diameter downstream location.

For this investigation, the upstream incoming turbulence was not scaled for the test articles. As a result, the downstream flows are dominated by screen and grid generated flow turbulence. A direct comparison of these flow characteristics is certainly relevant in evaluating the 3-D mixing capabilities of these screen designs. This comparison provides valuable insight into the screen generated turbulence interactions with the mean flow however definitive conclusions regarding the net turbulence attenuation of the upstream flow can not be drawn, base on this data alone. Future testing should involve properly scaled incoming turbulence for the test screens in order to accurately determine free stream turbulence attenuation properties.

Test Constraints and Limitations

Several significant constraints and limitations affecting this investigation were observed and warrant discussion. The UTSI Water Tunnel design combined with environmental conditions during testing adversely impacted the quality of the data collected. The screen data was collected in November and December 1996 when large, daily environmental temperature fluctuations, on the order of 50 degrees Fahrenheit, were typical. Uniform, stable water temperatures were practically impossible to achieve or maintain. Large portions of the gathered data (low Re data) were subsequently rendered unsuitable for further analysis and reporting because of these unknown local temperature gradients in the flow which could not be resolved from actual flow velocity using the constant temperature hot film anemometry technique. A fully internally housed water tunnel with accurate flow quality control is necessary for year round testing. The deteriorated state of the UTSI water tunnel, its apparent poor calibration and the impacts on accurate flow generation (repeatable turbulence and mean flow characteristics) was also of concern during these tests. Accurate and repeatable turbulence generation in a fully stabilized flow is essential. The water tunnel should be substantially renovated and calibrated for follow-on testing.

This investigation was based on comparing flow data gathered behind two test articles. All test grids were hand manufactured at UTSI and the test screens were obtained from a commercial manufacturer and then hand modified. As such all test articles were non-precision fabricated to lax tolerances. The modification involved hand-wrapping the grids and screens with the malleable copper coated wire. The wire wraps were attached at the rod

ends with non uniform solder beads. *Watmuff's* [9] recent research into the detrimental effects created by free stream non-uniformities, generated by non-uniform wind tunnel screens, highlights the importance of precision fabricated, uniform screens. In the course of his efforts to improve the flow quality in a small stand-alone wind tunnel, modified for flow transition studies (laminar to turbulent flow), he measured significant stream-wise vortices (Klebanoff modes) created by practically immeasurably small non-uniformities introduced into the flow by non-uniform screens. With the insertion of a Blasius flat plat into the downstream flow, these immeasurably small non-uniformities created large spanwise vortices. He discovered spanwise variations in the porosity of his screens and when corrected, reduced the background unsteadiness in the flow by a factor of 30. In this study, the screens were much larger and the variations in screen porosity and helical wrap were proportionately large (although not measured) given the hand manufacture technique. Accordingly, large flow non-uniformities can be expected downstream of the grids and screens. This draws into question the degree of relevance of the direct comparison of test data and the overall confidence in the data quality. Repeatable trends were observed, however, that conform nicely with the anticipated physics of the flows and as such are most likely representative of modification influences on the flow. Future testing, however, should involve precision manufactured test articles to eliminate these flow discrepancies and sources of comparison errors.

The use of small, non-precision fabricated grids and 12 x 12 inch screen leftover pieces during testing, was driven by schedule and fiscal constraints. The test articles did not completely enclose the water tunnel cross-sectional area which allowed for flow bypass and any resulting interference effects. These were minimized during screen testing by collecting data at the center location but down stream test points would be progressively impacted. The single grid data was mostly impacted by this and as a result the center test point data was chosen for detailed analysis. These detrimental effects were further reduced based on the comparative nature of this study. Generally, as a proof of concept study, these shortcomings are acceptable however, future testing should involve larger test articles fully enclosing the test section to better duplicate the water/wind tunnel turbulence reduction applications.

Chapter 5

CONCLUSIONS AND RECOMMENDATIONS

An experimental study of the potential for enhanced turbulence attenuation using a mesh screen modified with a helical wrap was conducted. Previous investigations have suggested that helical wrapping can influence the shedding vortices downstream of the screen by enhancing 3-D mixing in the flow. The flows behind baseline and modified single rods, grids and screens were investigated using qualitative flow visualization techniques and quantitative hot film velocity measurements.

The following conclusions are identified:

a) A direct qualitative flow visualization comparison of the flow fields downstream of the baseline and modified test articles revealed consistent, repeatable trends;

b) The helical wrap modification clearly demonstrated more three dimensional mixing in the flows behind the single rods, grids and screens and created less coherent vortex shedding structures;

c) The flow visualization suggests that the modified screen assists in the weakening and possible destruction of the vortices which are shed when the flow passes through the screen;

d) Flow visualization results indicated that the 1 inch wrap pitch length was the optimum wrap pitch length and the double wrap showed added effectiveness in disorganizing the shedding vortices;

e) The average axial velocity, standard deviation and axial turbulence intensity behind the modified grid and screen were consistently slightly lower when compared to the baseline data at Reynold numbers of 500 and 600 respectively and at all downstream axial locations;

f) The axial velocity frequency spectra in the flow 20 diameters downstream of the modified grid (1 inch single helical wrap) and screen (1 inch double helical wrap) revealed a lowering in the vortex shedding frequency with an associated

amplitude decrease on the order of 50% in the 2 Hertz (baseline shedding frequency) range;

g) Contrary to the axial velocity results, the average lateral velocity and standard deviation results behind the modified screen were consistently slightly higher when compared to the baseline data at the 20 diameter downstream location. These findings conformed nicely with the enhanced lateral 3-D flow mixing which was anticipated as a result of the wrap and demonstrated in the flow visualizations;

h) Farther downstream (100 and 192 diameters), the average lateral velocity and standard deviation results showed a consistent reduction when compared to the baseline data;

i) The lateral turbulence intensity values were consistently higher at all axial stations behind the modified screen as compared to the baseline data when calculated as a fraction of the local average lateral velocity. When directly compared to the baseline data using the same scaling denominator ($U_{Baseline}$), the modified screen lateral turbulence intensity values were comparable to or slightly better than the baseline screen results;

j) The lateral velocity frequency spectra showed a slight increase in distinct frequency content 20 diameters downstream of the modified screen, however, unlike the axial frequency data, an increase in the amplitudes was observed. This is most likely a direct result of the added 3-D mixing created by the wrap which is most apparent in the lateral direction;

k) Although the data trends were consistent during these experiments, the overall differences between the baseline and modified test articles (single and multiple grids) were very small. This justifies more detailed analysis before absolute conclusions concerning the turbulence reduction effectiveness of the modified screen can be drawn; and

l) The effective manipulation of the frequency spectra distribution by the helical wrap modification immediately downstream may be the primary mechanism causing enhanced mixing in the flow and the reduction of the coherent shedding vortex structures.

The following recommendations are made:

a) Future testing should involve precision fabricated screens of various wrap characteristics, screen dimensions and porosities to achieve a thorough parametric study;
b) Although the limited testing conducted to date is beneficial to preliminary investigations into the effectiveness of turbulence intensity reduction in a uniform axial flow using helically wrapped screens, eventual testing must involve test articles completely enclosing the test section;
c) Future testing should also key on the flow field and in particular the turbulence intensity farther downstream of the screen (on the order of 200 to 300 diameters of the screen mesh) where the vortices have decayed to final turbulence levels in the flow;
d) Future testing should properly scale the upstream turbulence for compatibility for test purposes with the selected test articles in order to better evaluate the turbulence reduction effectiveness of this modification;
e) Follow-on testing in a wind tunnel with potentially greater velocity measurement sensitivities should be considered;
f) The effects of multiple modified screens should also be considered when assessing overall turbulence attenuation effectiveness; and
g) The pressure loss characteristics of flow through the modified screen should also be addressed as this directly impacts the operating requirements and capabilities of a tunnel.

LIST OF REFERENCES

LIST OF REFERENCES

1. Prandtl, L., Attaining a Steady Air Stream in Wind Tunnels:, NACA TM 726, Oct. 1933.
2. Batchelor, G.K., "The Theory of Homogeneous Turbulence", Cambridge University Press, 1953.
3. Bradshaw, P., "An Introduction to Turbulence and its Measurement", Pergamon Press, 1971.
4. Townsend, A.A., "The Passage of Turbulence Through Wire Gauzes", Q.J. Mech. Appl. Math., 4 308, 1951.
5. Corrsin, S., "Turbulence: Experimental Methods" Handbuck der Physik, 8-523, Berlin: Springer, 1963.
6. Laws, E.M. and Livesey, J.L., "Flow Through Screens", Ann. Rev. Fluid Mech., 10, 247-266, 1978.
7. Dryden, H.L. and Schubauer, G.B., "The Use of Damping Screens for the Reduction of Wind-Tunnel Turbulence", Journal of Aeronautical Sciences, April 1947.
8. Aljabari, S., "Pressure Loss Associated with Compressible Flow Through Square Mesh Wire Gauzes", AIAA 92-4043, 1992.
9. Watmuff, J.H., "Detrimental Effects of Almost Immeasurably Small Free-Stream Nonuniformities Generated by Wind Tunnel Screens", Aerospace Sciences Meeting and Exhibit, AIAA Paper No. 97-0228, Reno, NV. January 1997.
10. Butler, K.M., and Farrell, B.F., "Three Dimensional Optimum Perturbations in a Viscous Shear Flow", A 4 (8), 1637, 1992.
11. Cornish, J.J., "Vortex Flows", Eighth Quick-Goethert Lecture Series at The University of Tennessee Space Institute, 1982.
12. McKeage, B.J. and Vakili, A., "A New Screen for Turbulence Attenuation at Higher Reynold Numbers", Aerospace Sciences Meeting and Exhibit, AIAA Paper No. 97-0229, Reno, NV., January 1997.

13. McKeage, B.J., "A Screen Modification for Enhanced Turbulence Attenuation at Higher Reynold Numbers", AIAA Southeastern Regional Student Conference, Atlanta, Georgia, April 1997.

14. Goldstein, R.J., "Fluid Mechanics Measurements", Hemisphere Publishing Corporation, 1983.

15. Taylor, G.I. and Batchelor, G.K., "The Effect of a Wire Gauze on a Small Disturbance in a Uniform Stream", Q.J. Mech. Appl. Math. 2, 1, 1949.

16. Loehrke, R.I. and Nagib, H.M., "Control of Free-Stream Turbulence by Means of Honeycombs: A Balance between Suppression and Generation", ASME J. Fluids Engng. 98I, 342, 1976.

17. Scheiman, J. and Brooks, J.D., "Comparison of Experimental and Theoretical Turbulence Reduction from Screens, Honeycomb, and Honeycomb-Screen Combinations", J. Aircraft, 18, 638, 1981.

18. Collar, A.R., "The Effect of A Gquze on the Velocity Distribution in a Uniform Duct", ARC R&M 1867, 1939.

19. Scheiman, J., "Considerations for the Installation of Honeycomb and Screens to Reduce Wind Tunnel Turbulence", NASA TM 81868, 1981.

20. Burley, R.R. and Harrington, D.E., "Experimental Evaluation of Honeycomb/Screen Configurations and Short Contraction Section for NASA Lewis Research Center's Altitude Wind Tunnel", NASA Technical Paper 2692, May 1987.

21. Farrel, C. and Youssef, S., "Experiments on Turbulence Management Using Screens and Honeycombs", Transactions of the ASME, 26 / Vol. 118, Mar 1996.

22. Ahmed, G.R. and Brundrett, E., "Effect of Screen Porosity and Location on Wind-Tunnel Turbulence", AIAA Journal, Vol. 33, No. 5, 1994.

23. Salmirs, S. and Herrick, P., "Measurements of Turbulence Decay and Pressure Loss Between Wind Tunnel Turbulence Smoothing Screens", 28th Aerospace Sciences Meeting, Reno NV., 1990.

24. Derbunovich, G.I., Zemskaya, A.S., Repik, Y.U. and Sosedko, Y.P., "Optimal Control of Flow Turbulence by Means of Screens", Fluid Mech. Soviet Research, Vol. 19, No. 5, Sep-Oct 1990.

25. Pinker, R.A. and Herbert, M.V., "Pressure Loss Associated with Compressible Flow Through Square-Mesh Wire Gauzes", J. Mech. Eng. Sciences, Vol. 9, No. 1, 1967.

26. Lumley, J.L. and McMahon, J.F., "Reducing Water Tunnel Turbulence by Means of a Honeycomb", Transactions of the AMSE, Dec. 1967.

27. Mehta, R.D., "Turbulent Flow Through Screens", AIAA 84-0538, 22nd Aerospace Sciences Meeting, Reno, NV., 1984.

28. Groth, J. and Johansson, A.V., "Turbulence Reduction by Screens", J. Fluid Mech., Vol.197, 139-155, 1988.

29. Saxena, V., "Reduction of Turbulence in a 5 Inch Conduit Using Honeycombs and Screens", MSc Thesis, University of Minnesota, May 1989.

30. Goethert, B.H., "Transonic Wind Tunnel Testing", Oxford, N.Y., Pergamon Press, 1961.

31. Pope, A., "Low Speed Wind Tunnel Testing", N.Y., Wiley, 1966.

APPENDICES

APPENDIX A

HOT FILM CALIBRATIONS

Hot Film Calibration

Thermal anemometers utilize a small, electrically heated film to detect heat transfer changes associated with a moving fluid. These heat changes are then correlated to fluid velocity changes. A thermal anemometer is defined as a system which senses changes in heat transfer which are caused by changes in fluid velocity. Basic elements of a hot film anemometer include a sensing probe with a thin cylindrical film section exposed to the fluid flow (which effectively acts like a resistor), a constant temperature feed back loop, a series of fixed resistors, and a bridge power supply to complete the setup. Typically a linear relationship between the resistance R_{op} of the sensor and the constant temperature T_m is assumed as follows:

$$R_{op} = \left(\frac{R_{100} - R_0}{100} \right) T_m + R_0$$

Hot film sensors were used during this study because of their inherent strength and damage resistance to particles and debris in the water tunnel. Constant temperature hot film anemometers boast frequency response capabilities on the order of 100 KHz and are generally easy to use. The primary disadvantage associated with this velocity measurement technique is its obtrusive nature which can interfere with the flow. Additionally, probe oscillations created by flow over the support can results and effect velocity measurements. During this study, several precautions were taken to minimize these potentially adverse obtrusive influences including a careful probe oscillation study.

The relationship between the flow velocity and the sensor output resistance must be carefully determined prior to testing. The calibration process involves exposing the sensor to a suitable range of known flow velocities and then measuring the operating resistances. The accuracy of the sensor is directly related to the precision and care of the calibration procedure and also dependent on how closely the ensuing test conditions replicate the calibration conditions. The two predominate characteristics of a hot film calibration include the non linear nature of the resulting Velocity versus Voltage curve and the apparant decreasing sensitivity at elevated velocities (less steep slope).

When using a single sensor measurement technique, ideally the hot film probe is positioned such that the flow is normal to the sensor film axis and normal to the probe supports. All calibrations were conducted using the UTSI Hot Film Calibration Stand with a probe alignment to the flow in this fashion. In reality, however, and certainly in a turbulence investigation, the flow will approach the sensor at an angle and will be comprised of three orthogonal velocity components (with respect to the sensor hot film axis). These components include the velocity components:

a. V_N normal to the sensor and parallel to the supports;

b. V_T tangential to the sensor; and

c. V_{BN} normal to the sensor and normal to the supports.

These components are illustrated in Figure A-1.

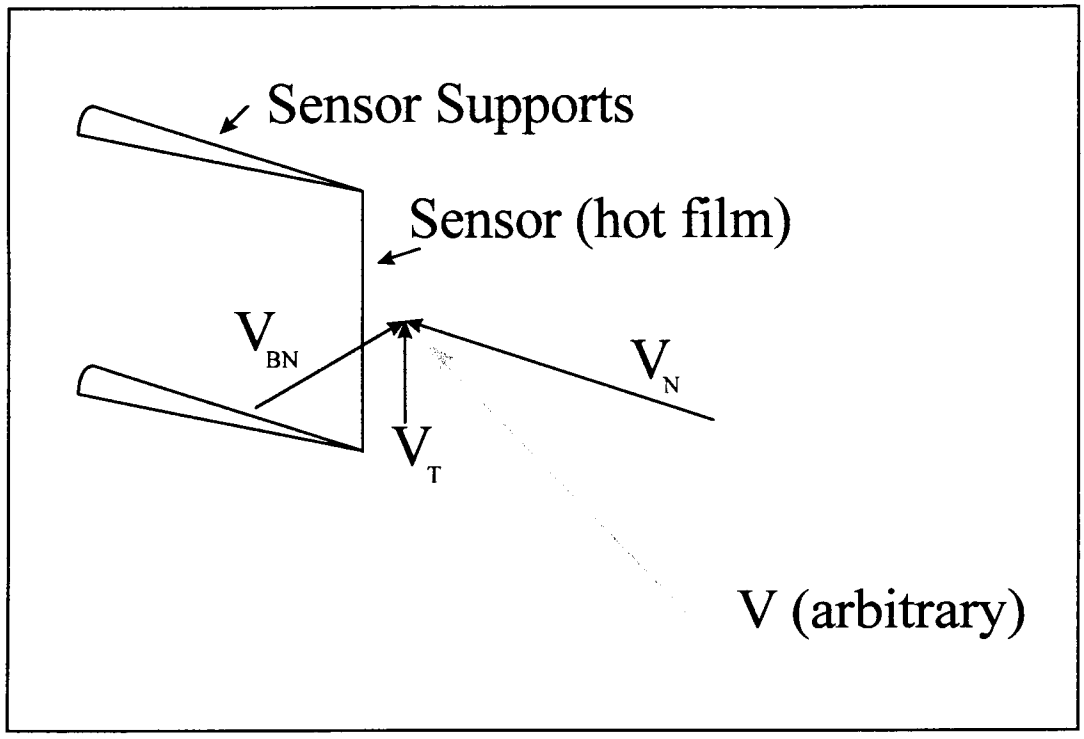


Figure A-1. Hot Film Sensor Velocity Components

Calibrations to resolve these components of flow velocity to determine the effective velocity are complex but possible and are detailed in Reference [14]. Due to resource limitations and a marginal benefit to turbulence measurement testing a simple calibration was used. The probe was positioned in the calibration stand with the supports and hot film perpendicular to the flow velocity direction. Accordingly, the probe output voltage was calibrated to known V_{BN} component velocities. The probe was then positioned in the water tunnel such that the V_{BN} direction was aligned with the tunnel flow axis. The resulting velocity measurement was called the axial component (u), ignoring off angle flow influences. In the same manner, with the probe rotated 90 degrees to the tunnel flow axis, the resulting velocity measurement was called the lateral component (w), again ignoring any off angle flow influences. This simple calibration was suitable for this study which was primarily concerned with comparing flow fields at selected downstream locations in identical upstream flows. The probes were oriented exactly in the same positions during the study to enable direct comparisons in the flow data.

Single Grid Hot Film Calibration.

A model 1210 Standard Straight DISA Probe was used for the single grid experiments and was calibrated using the IFA-100 Hot film anemometer constant temperature system. The probe was calibrated in the UTSI calibration tow tank using water taken directly from the water tunnel to ensure a properly representative calibration medium. The calibration illustration is provided in Figure A-2.

During the calibration, the tow tank water temperature remained within 0.5 degrees of the water tunnel temperature (approximately 28°C). The quality of the water appeared very clean and throughout the calibrations, air bubble accumulations on the probe rarely occurred and did not pose any special problems (as is evident in the quality of the resulting calibration curves).

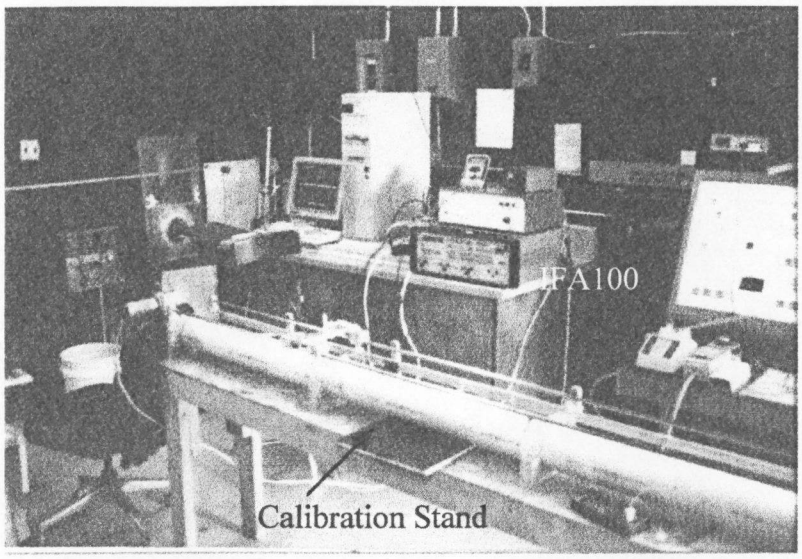


Figure A-2. IFA100 Hot Film Calibration Set-up with Tow Tank

A supplemental calibration and units conversion program, which had been written in Quick Basic for unrelated research work, was modified for the purposes of this project. The program converted voltage outputs from the IFA100 (from the hot film) to velocity values in inches per second using the calibration curve obtained by means of a curve fit. Nonlinear Least Squares Analysis (nonlinear regression) of the calibration data were performed using an iterative algorithm to fit Kings nonlinear mathematical model to the raw data points. The general form of King's Law is shown in the following equation:

$$E^2 = a + b \times V^n$$

The optimum curve fit for King's formula was achieved by iterating solutions using a, b and n as unknown parameters (a=b=n=1 as the initial guest value). After 6 iterations, the curve fit converged to a solution of the form:

$$E^2 = 2.1621 + 3.0367 \times V^{0..4758}$$

The Residual Sum of the Squares (RSS) was minimized in the iterations generating this solution. The RSS was the sum of the residual squares, where the residuals were the differences between the actual dependent (E^2) variable and the "predicted value" (the

distance from a data point to its predicted value on the fitted curve). The optimized RSS was 1.5. The calibration curve for the probe is provided in Figure A-3.

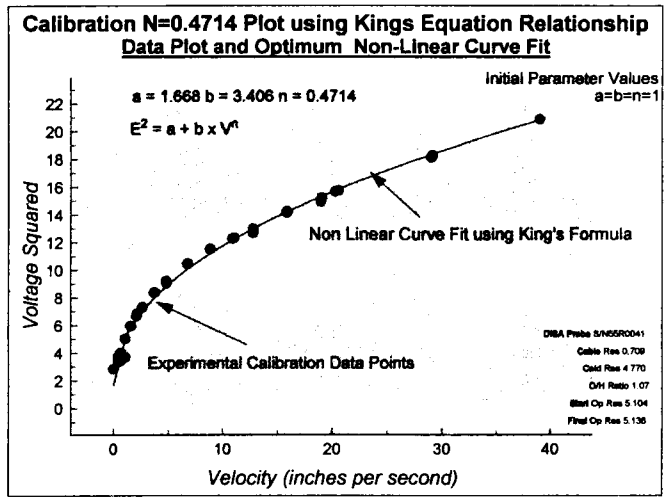


Figure A-3. IFA100 Hot Film Calibration Curve
with King's Law Non-Linear Curve Fit

The optimized curve fit in Figure A-4 using King's non-linear relation was not considered to be the best possible curve fit for follow-on test purposes. At velocities above approximately 1.5 inches per second, the curve fit showed a pronounced deviation from the actual data. As a result, a fourth order polynomial curve fit was applied to the raw data as a comparison. This curve fit is shown in Figure A-4. The polynomial equation is shown as follows:

$$V = -0.8876 + 0.3919 \times \left(E^2\right) - 0.03063 \times \left(E^2\right)^2 + 0.002377\left(E^2\right)^3 + 0.0005296\left(E^2\right)^4$$

The polynomial curve fit was ultimately selected as the best fit and was used in the voltage-to-velocity conversion program. Selected points in the calibration profile were repeated in the tow tank prior to the test and demonstrated excellent conformity with the curve fit.

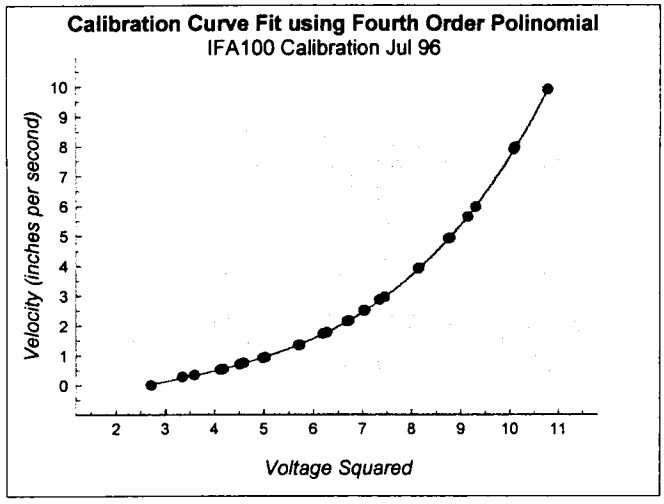
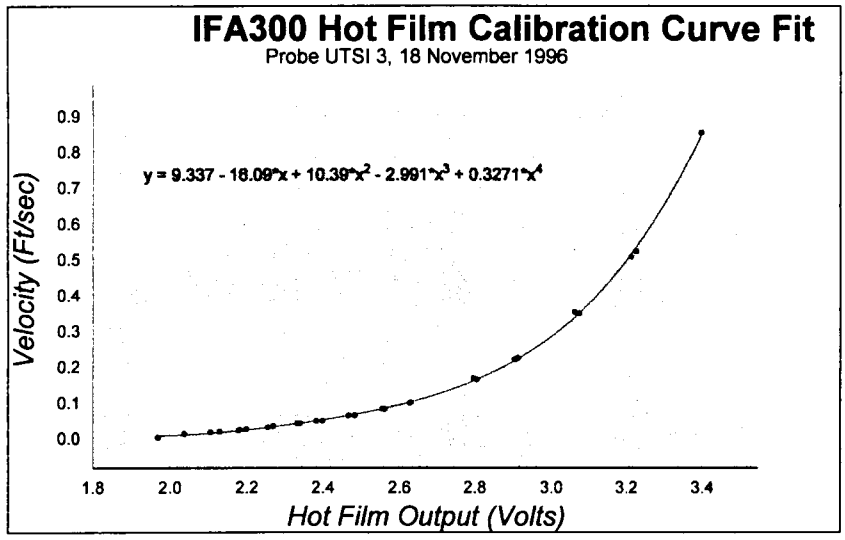


Figure A-4. IFA100 Hot Film Calibration Polynomial Curve Fit

Single Screen Hot Film Calibration.

Calibration of the two hot film probes used for the follow-on single screen testing was dramatically simplified with the help of the IFA300 software. Two separate sensors were used during these tests (UTSI Probe 1210-29W SN:926058 and Sverdrup Probe #6 SN:1201-6). Both exhibited practically identical characteristics and the calibrations demonstrated excellent repeatability. Unlike the single grid calibrations which had been conducted in July with warm water temperatures (28°C), the single screens calibrations were conducted in November with water temperatures typically around 13 to 15 °C. An IBM compatible computer was required to control the Calibration Stand and and separate computer was required to operate the IFA300 software during the calibration procedure. The calibration procedure was practically identically to the IFA100 procedure however, the IFA300 system directly provided a 4th order polynomial curve fit. The two calibration curves are provided in Figure A-5. The plots clearly illustrate the small error associated with each point.



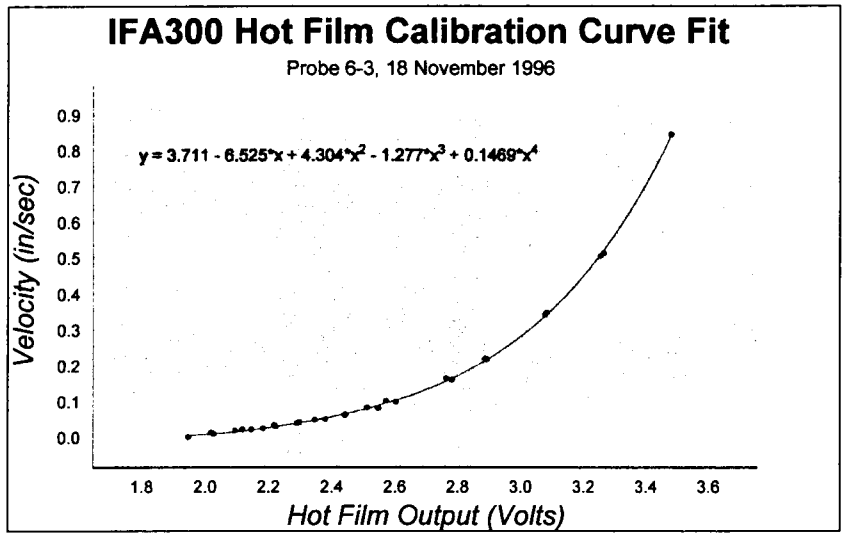


Figure A-5. IFA300 Hot Film Calibration Curves for Single Screen Tests

APPENDIX B

WATER TUNNEL CALIBRATION

Water Tunnel Calibration

Prior to the single screen testing, the UTSI water tunnel was calibrated and a velocity profile survey was conducted at various locations in the test section. Since single screen testing involved considerable data acquisition and was time consuming, an accurate water tunnel calibration was required to ensure comparable test conditions. The tunnel was calibrated at the flow centerline location with the 1 inch thick honeycomb flow straightener installed at the inlet to the test section. The resulting calibration curves are presented in Figure B-1.

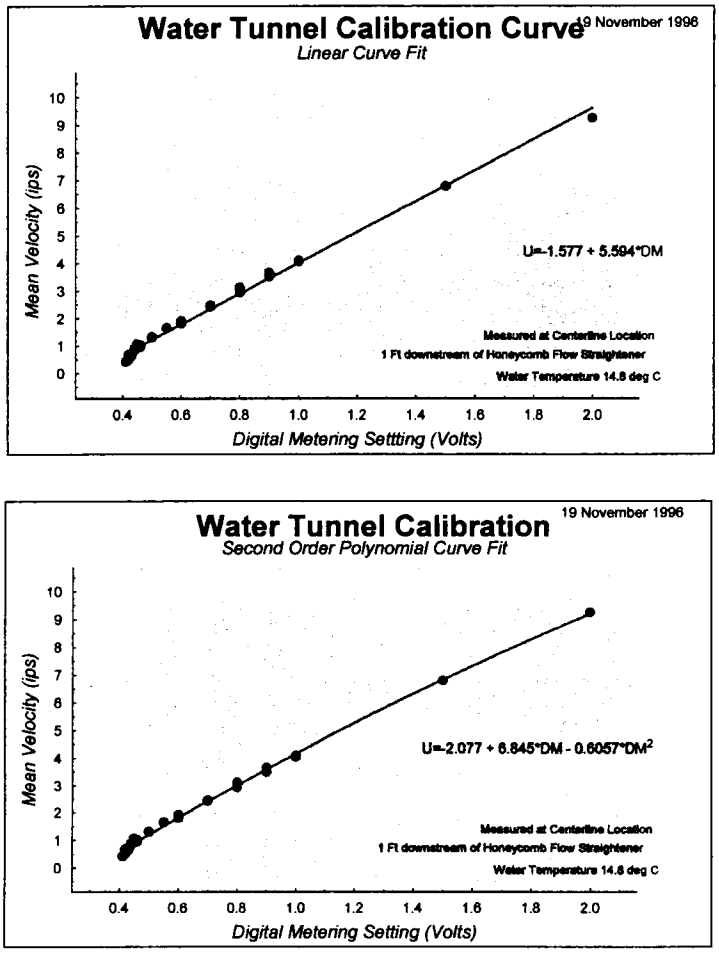
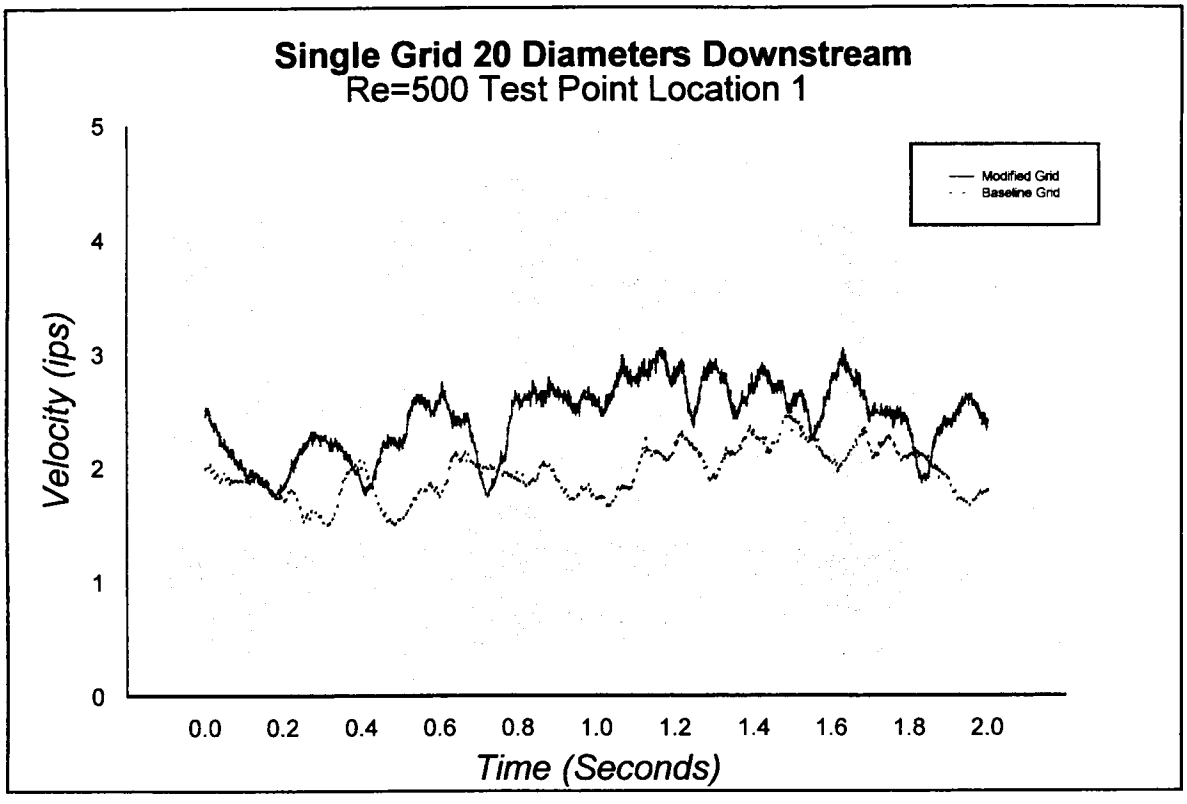


Figure B-1. Water Tunnel Calibration Curves (Linear Curve Fit on Top and 2nd Order Polynomial Curve Fit on Bottom)

APPENDIX C

SINGLE GRID RESULTS



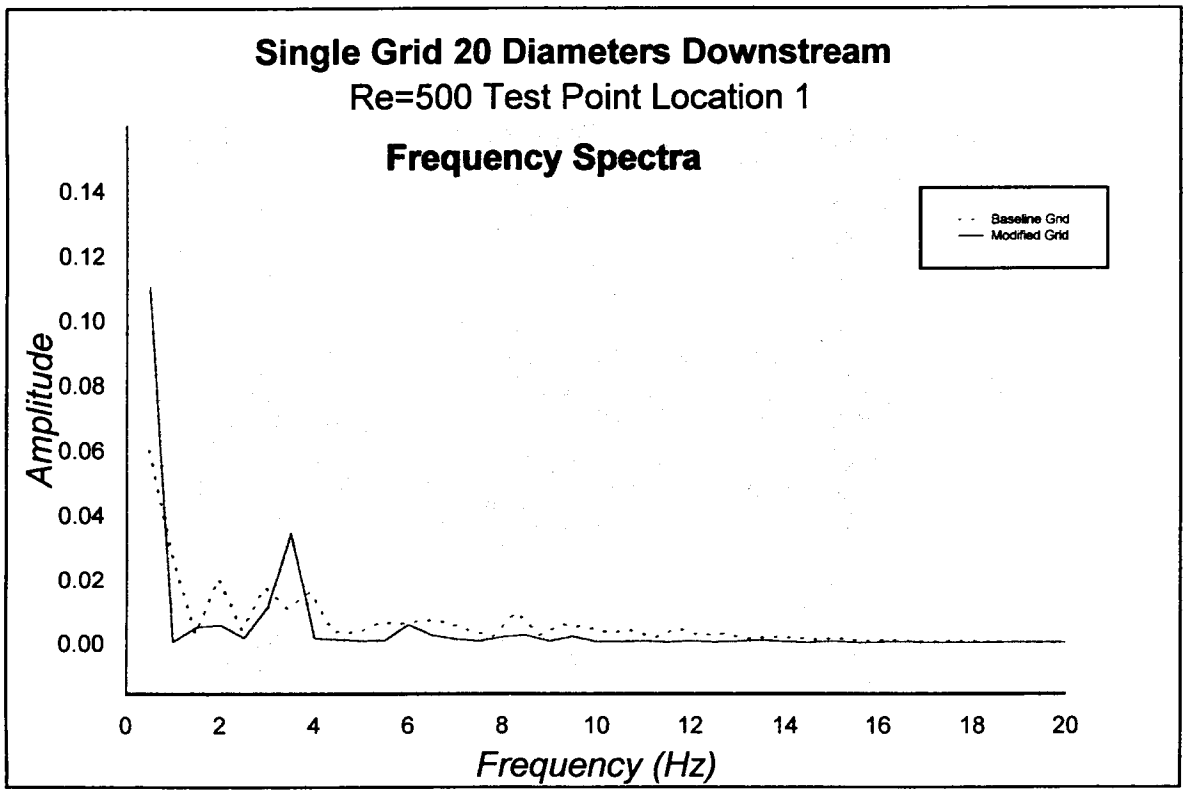
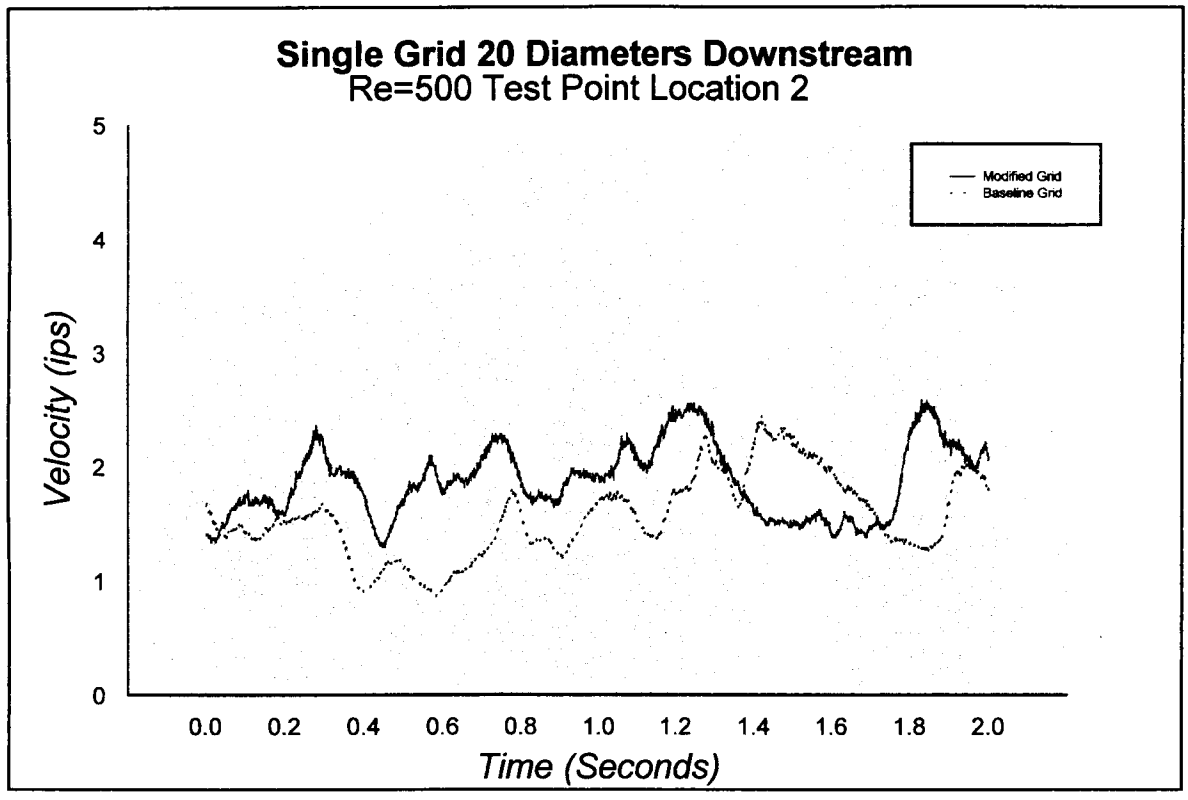


Figure C-1. Single Grid Location 01
Velocity and Frequency Spectra Plots



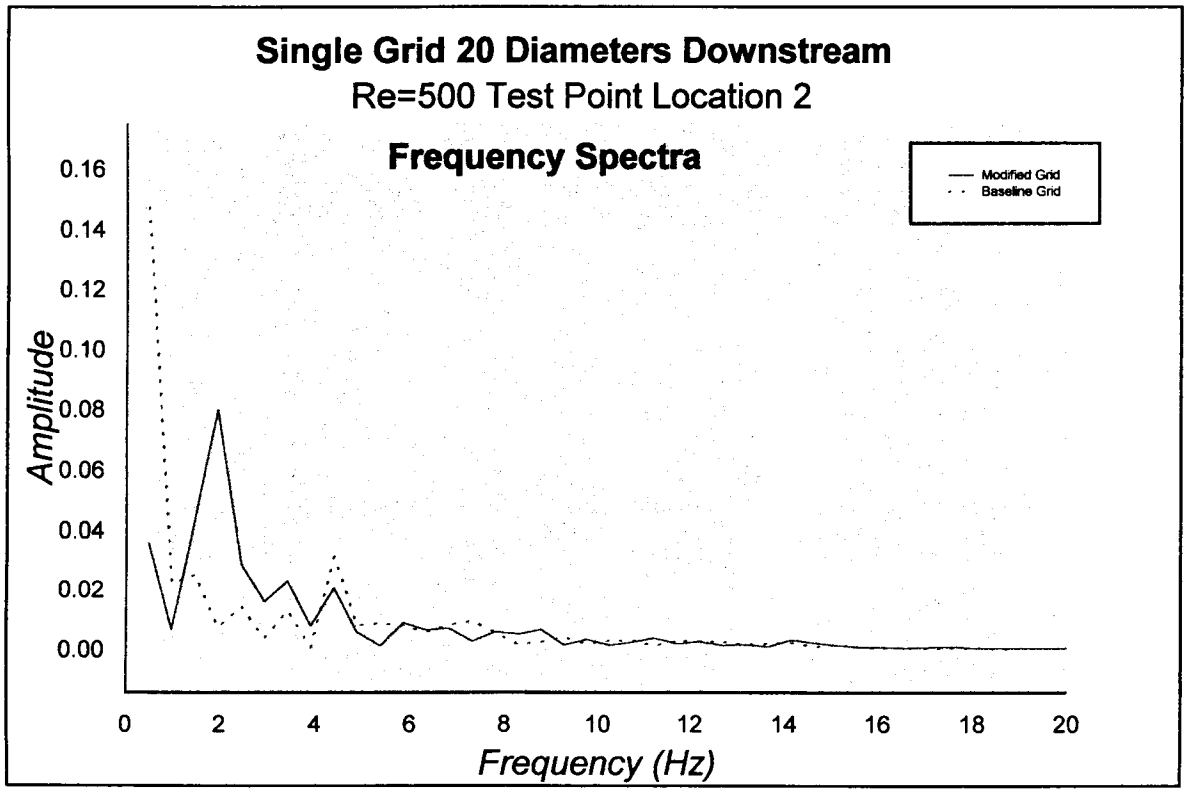
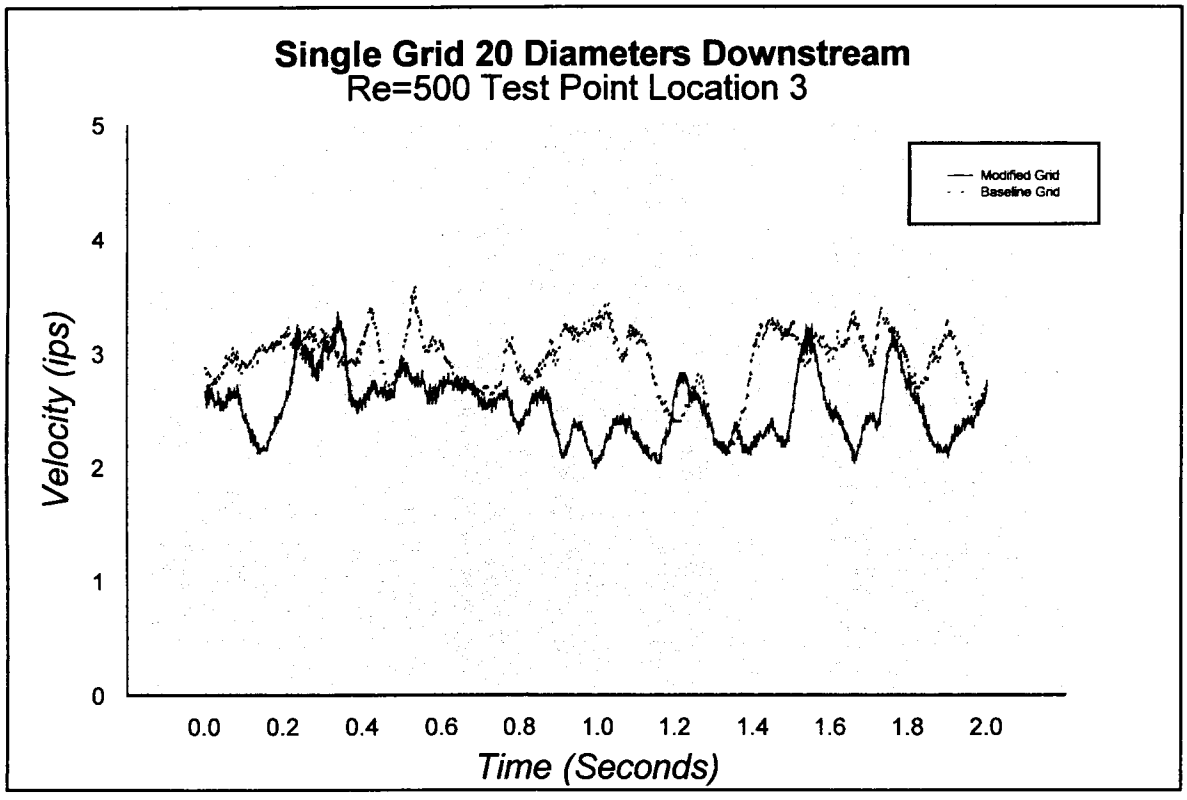


Figure C-2. Single Grid Location 02
Velocity and Frequency Spectra Plots



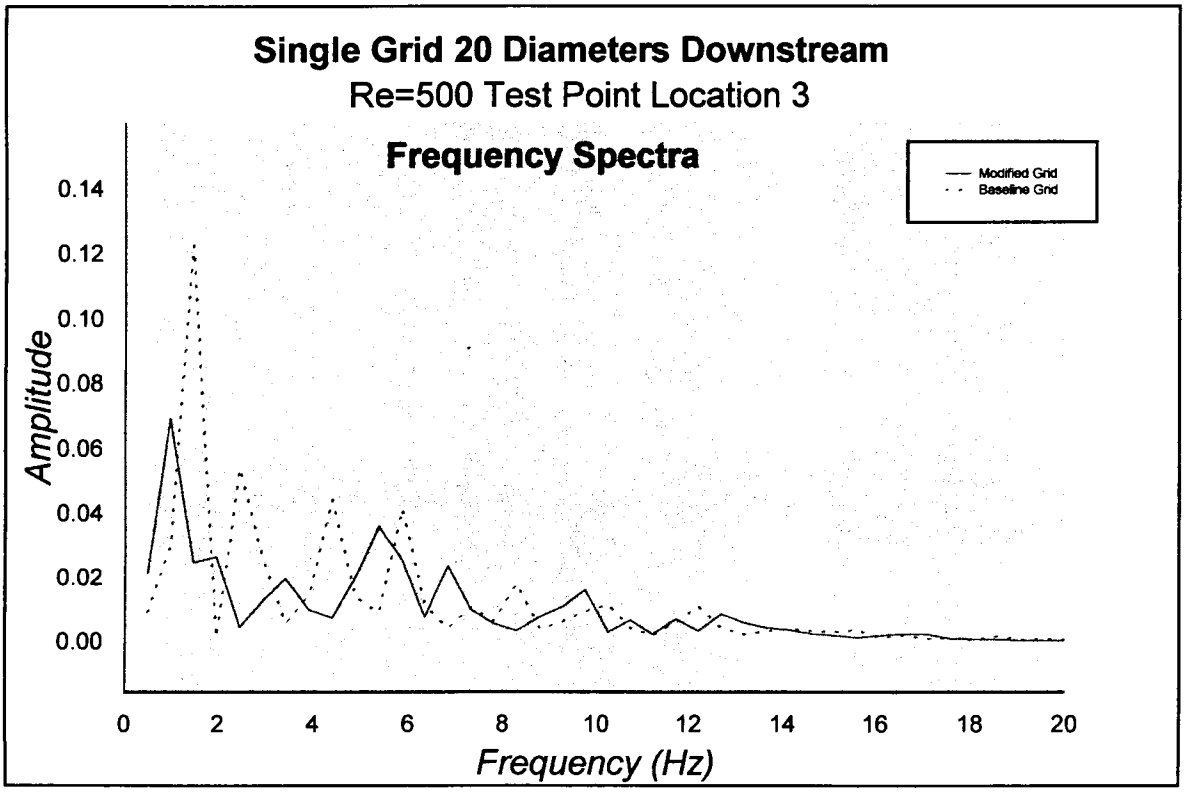
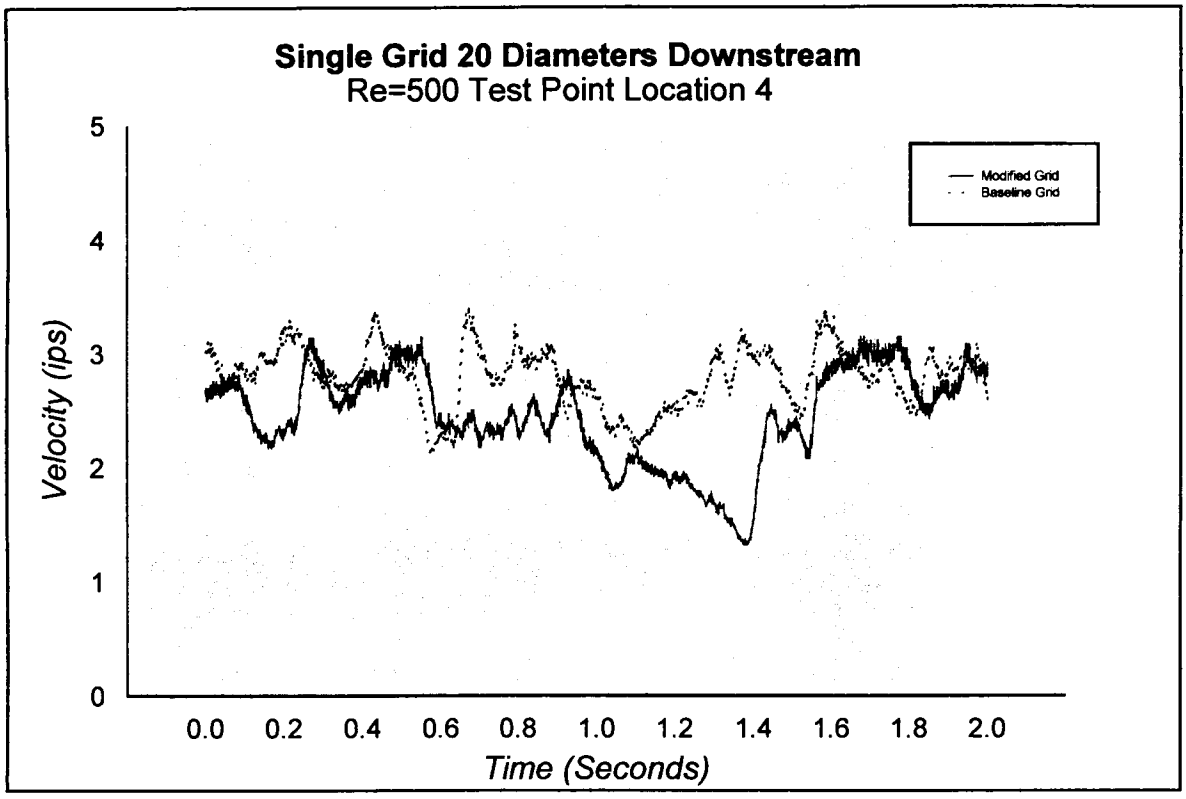


Figure C-3. Single Grid Location 03
Velocity and Frequency Spectra Plots



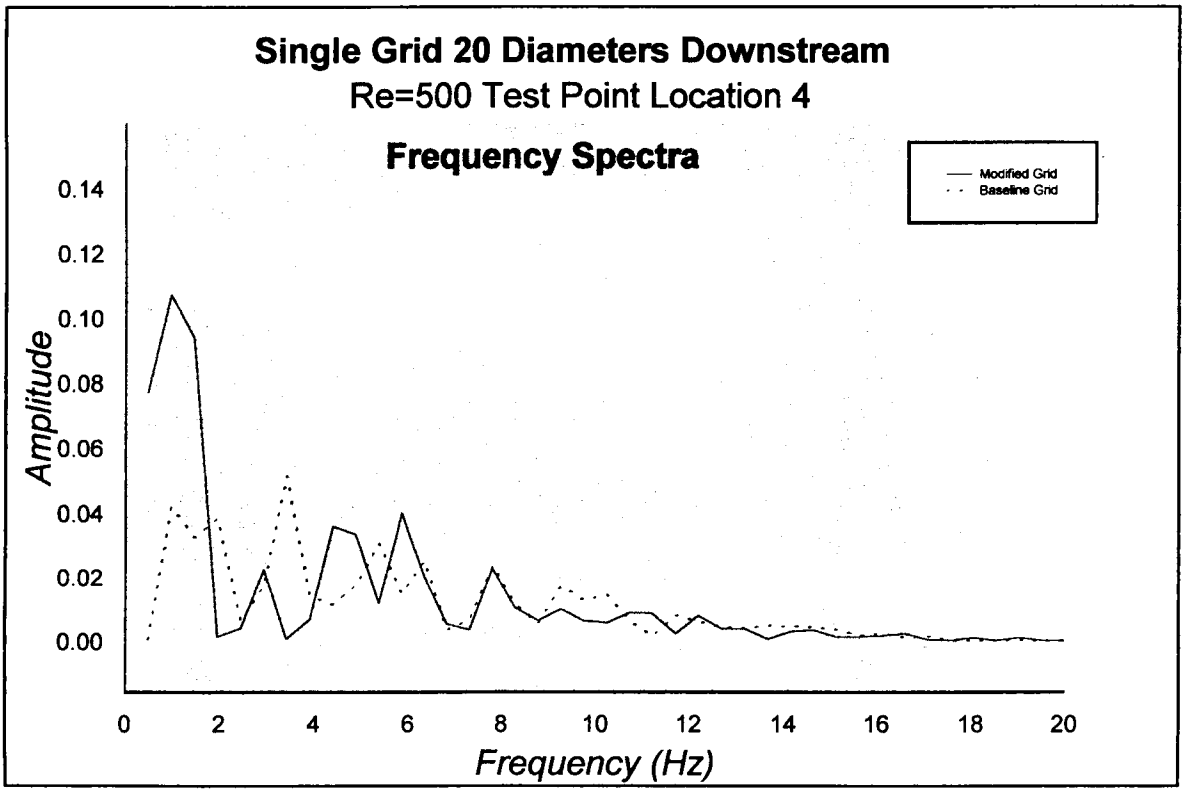
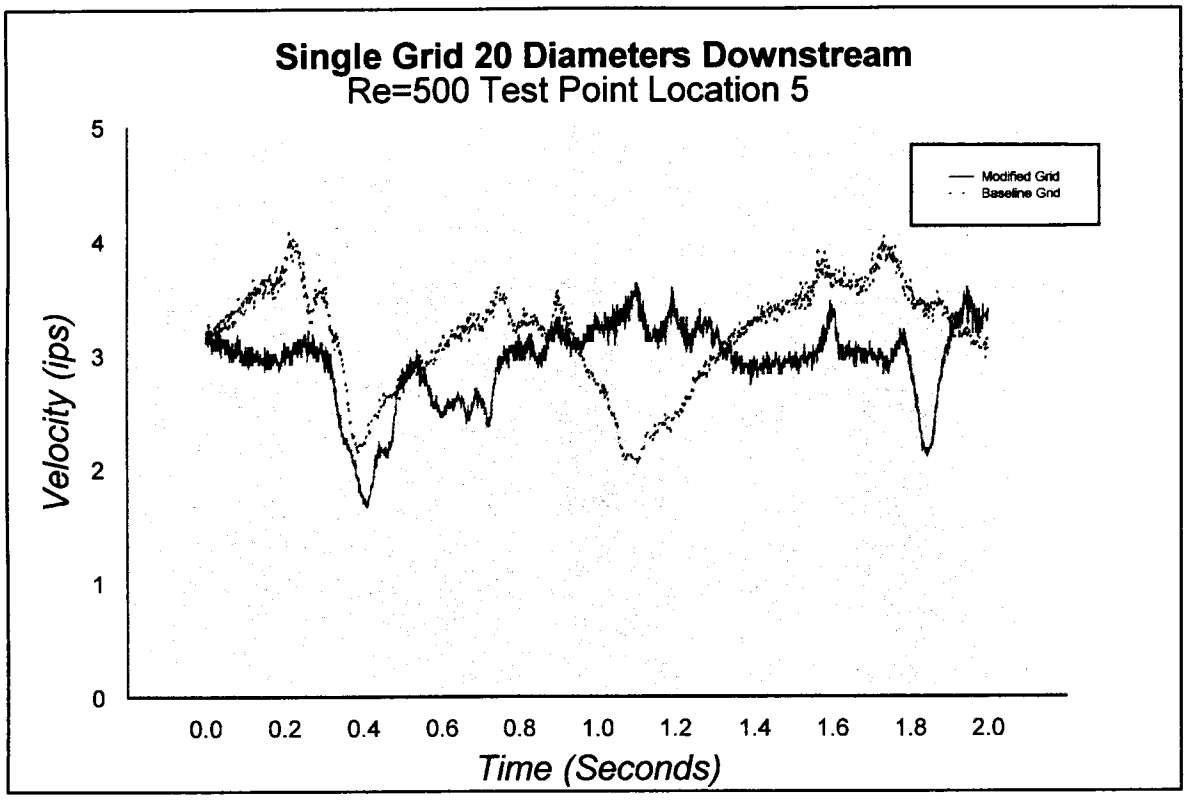


Figure C-4. Single Grid Location 04
Velocity and Frequency Spectra Plots



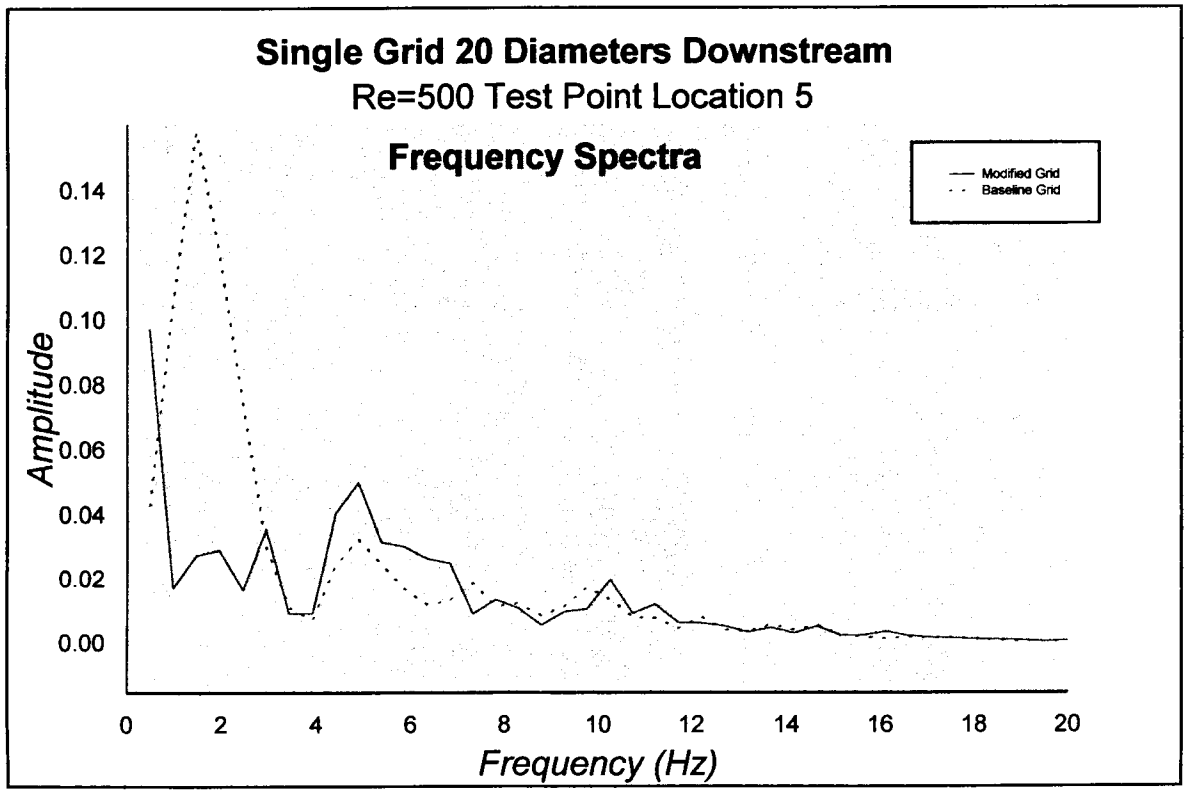
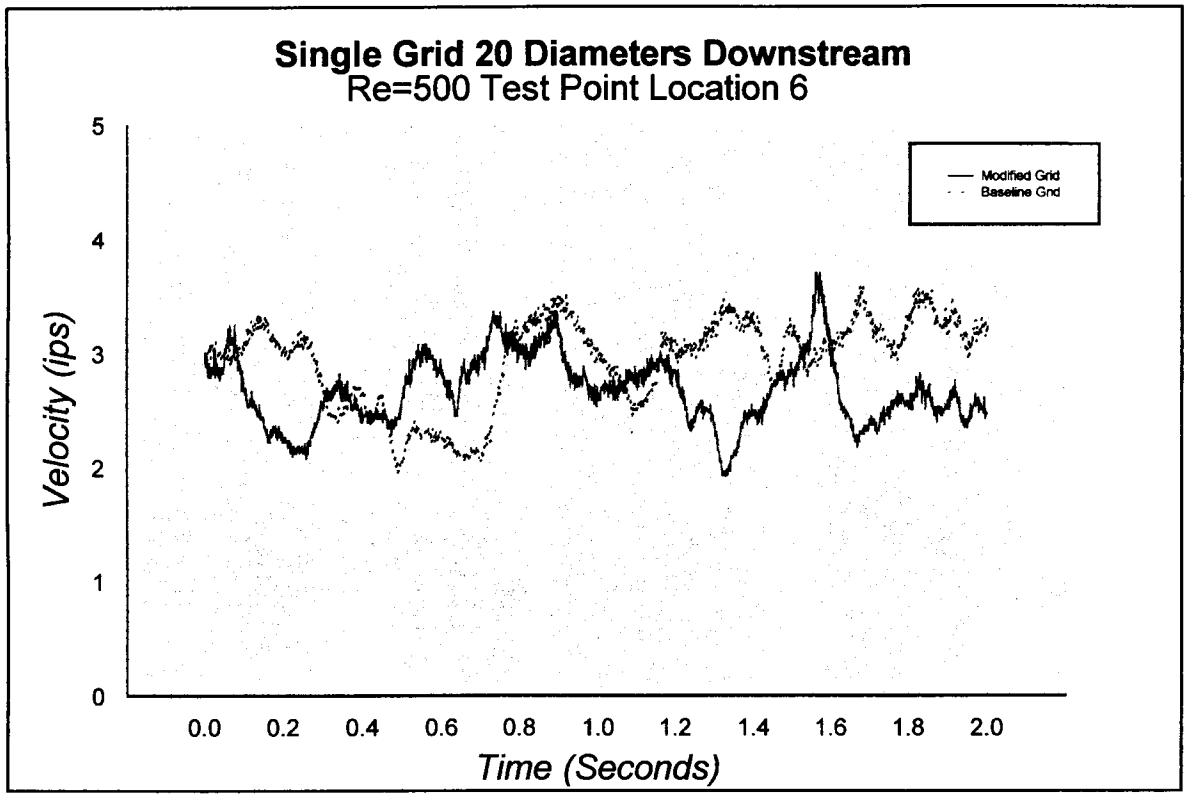


Figure C-5. Single Grid Location 05
Velocity and Frequency Spectra Plots



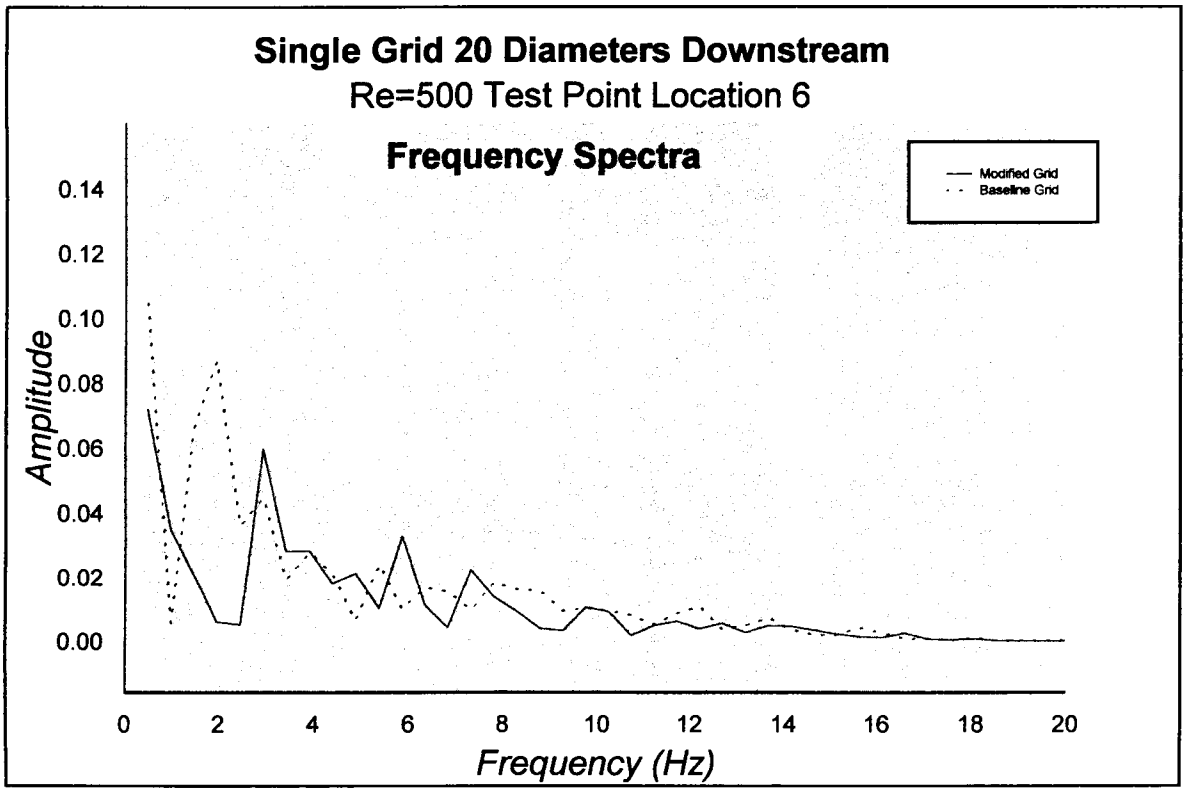
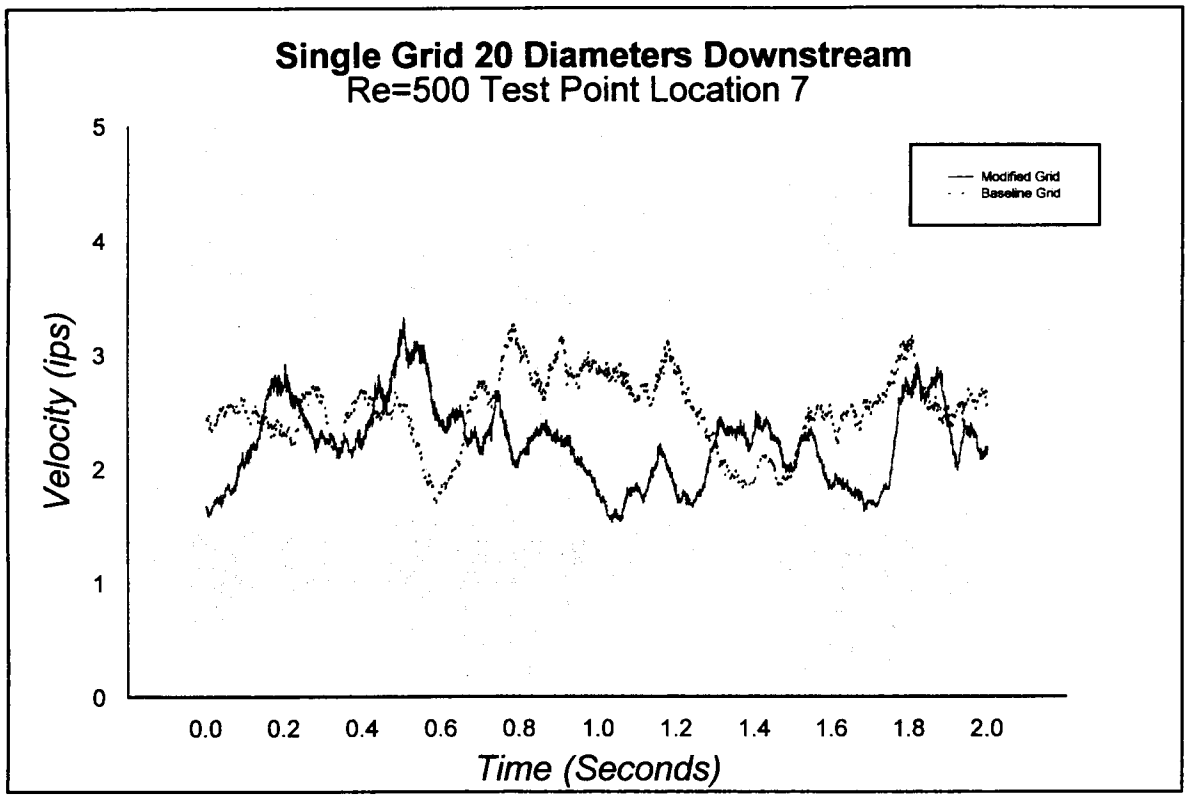


Figure C-6. Single Grid Location 06
Velocity and Frequency Spectra Plots



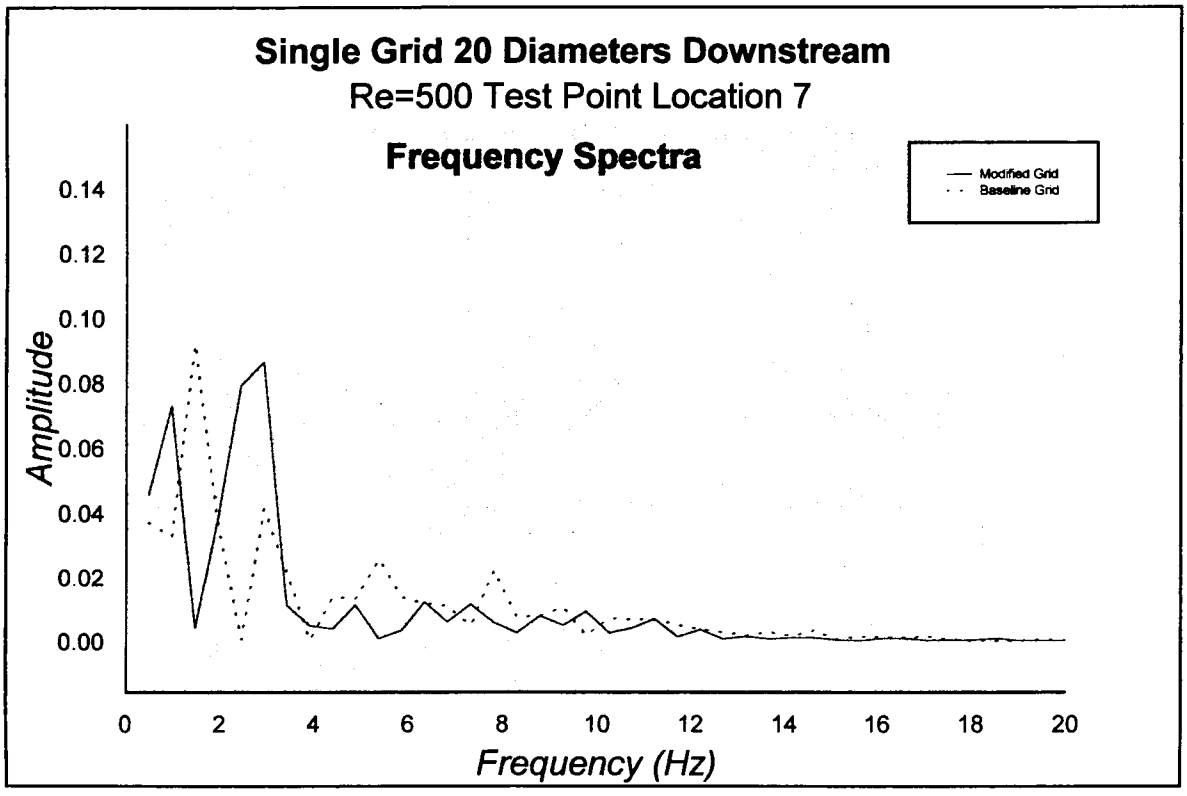
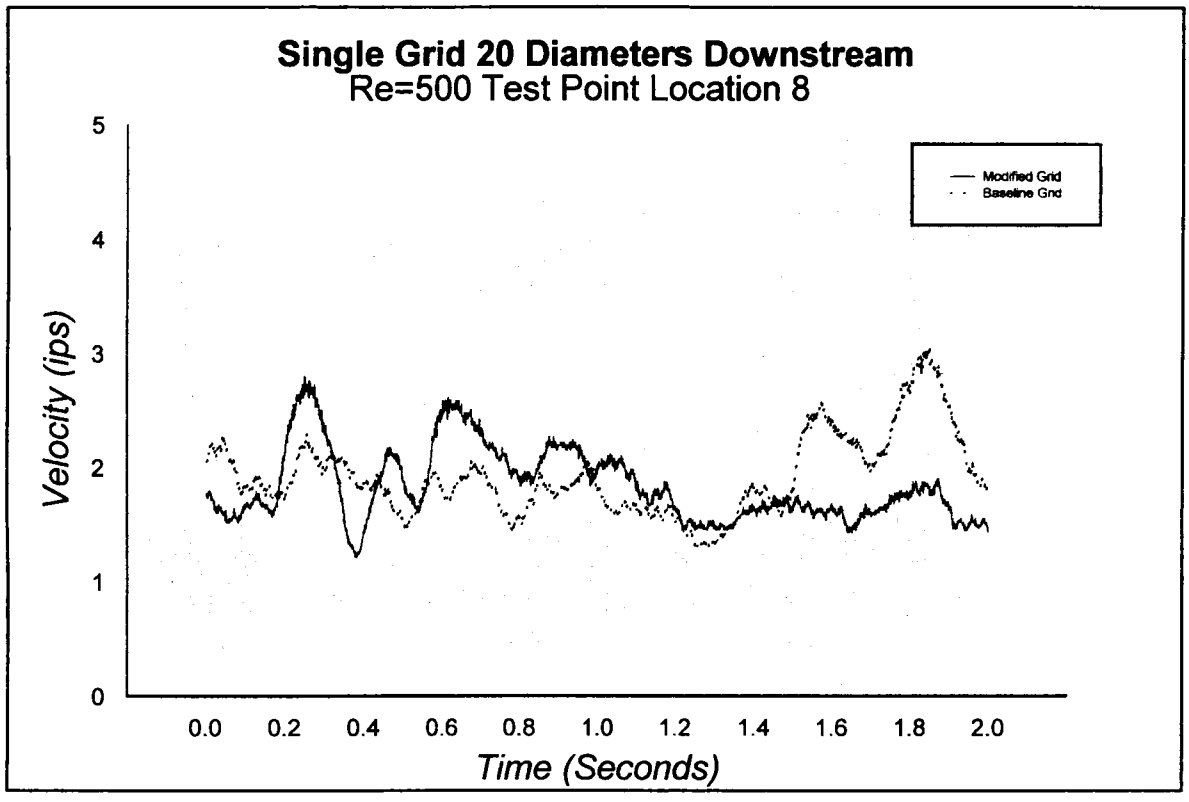


Figure C-7. Single Grid Location 07
Velocity and Frequency Spectra Plots



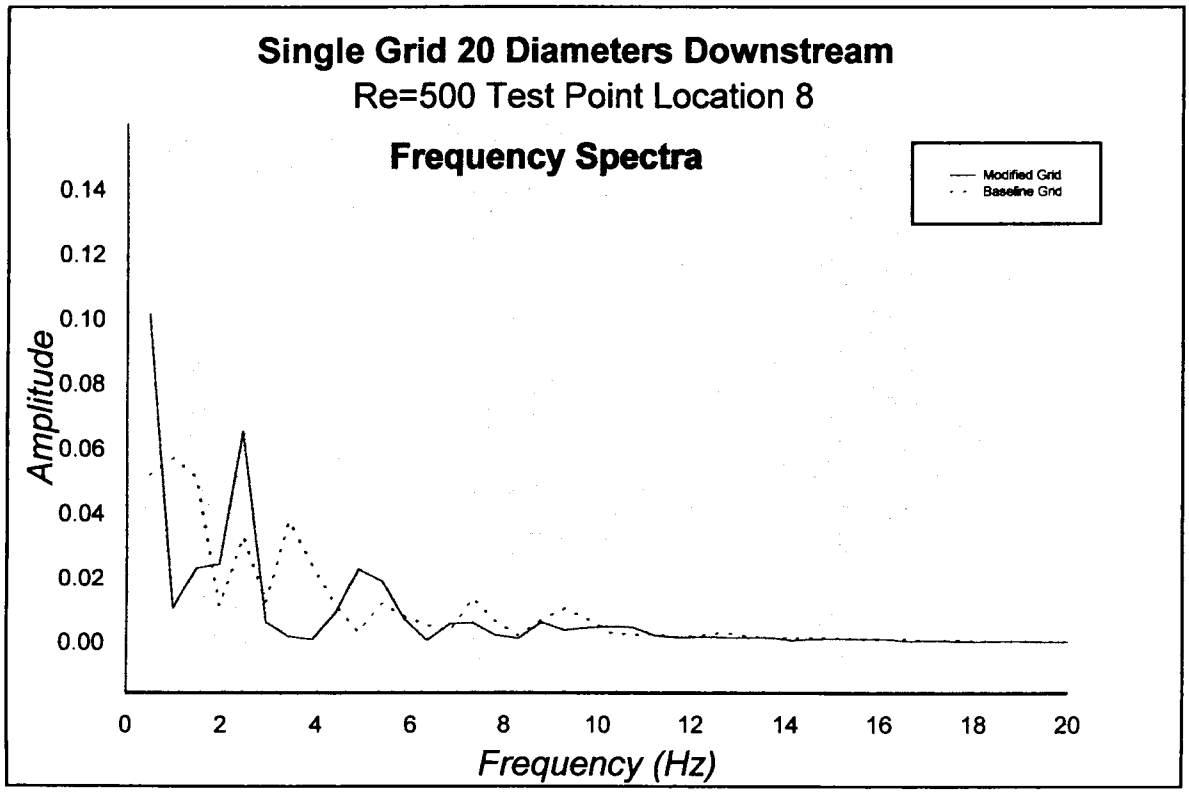


Figure C-8. Single Grid Location 08
Velocity and Frequency Spectra Plots

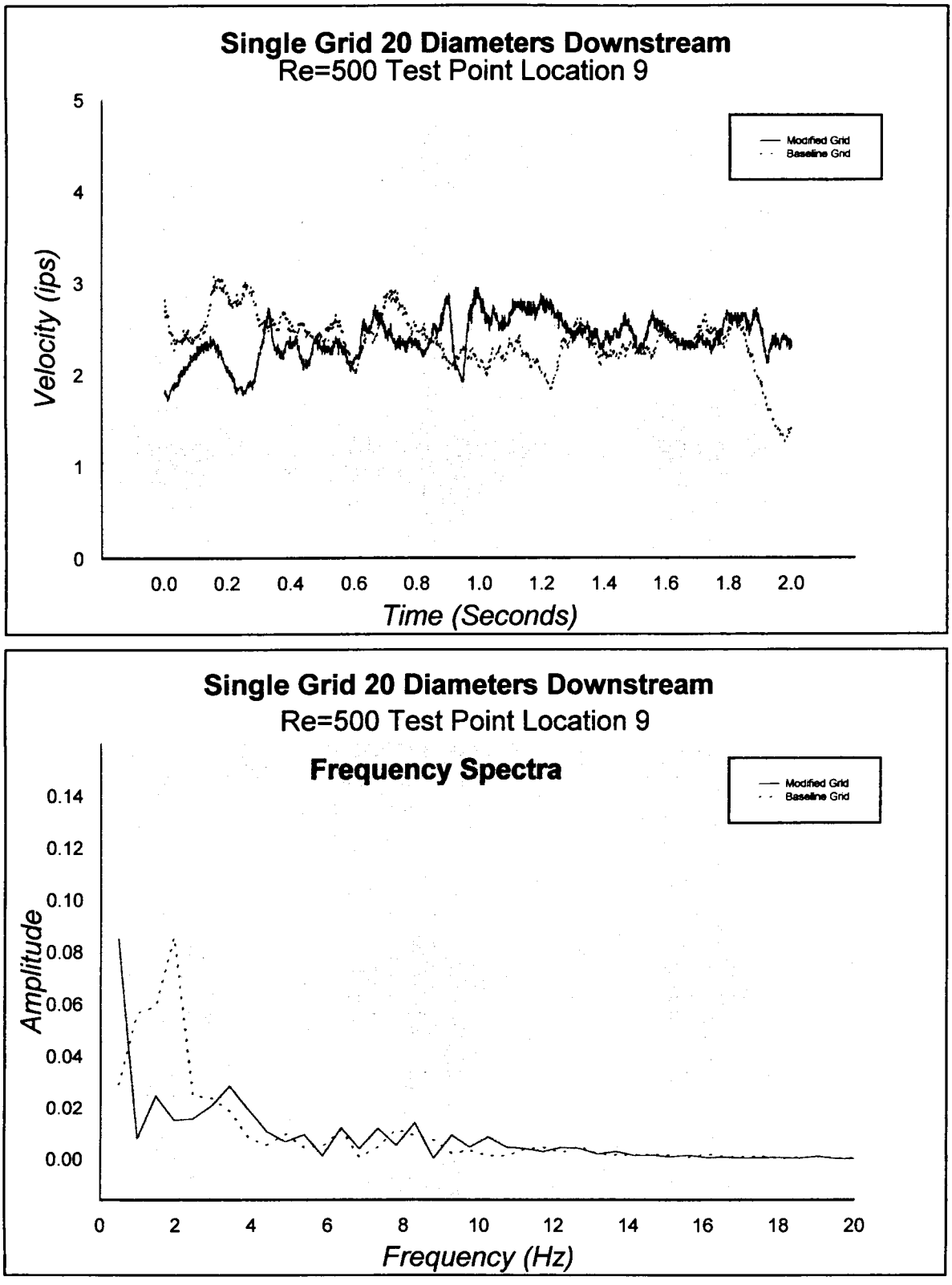


Figure C-9. Single Grid Location 09
Velocity and Frequency Spectra Plots

APPENDIX D

SINGLE SCREEN RESULTS

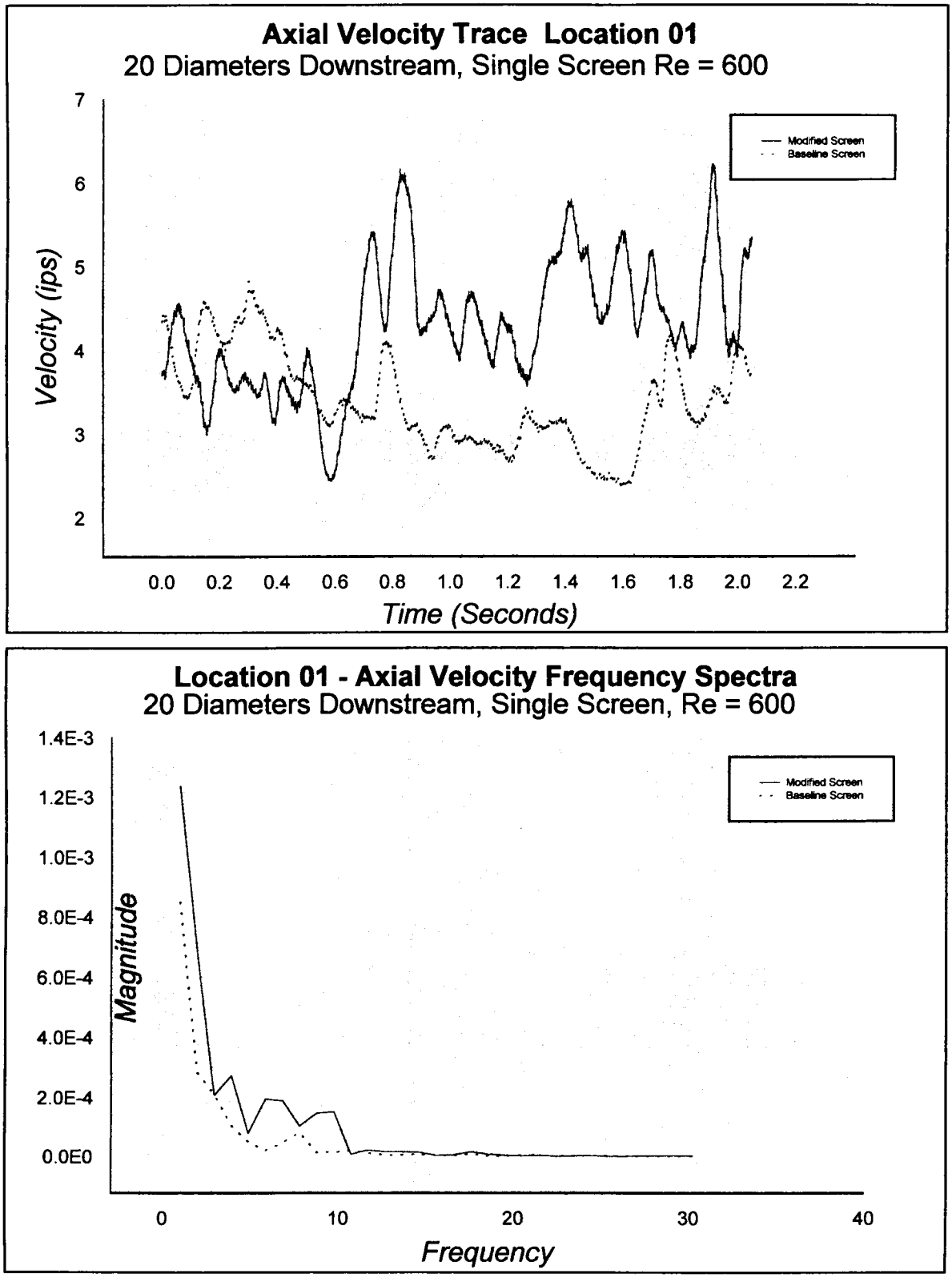


Figure D-1. Single Screen Location 01, 20 Diameters Downsteam
Axial Velocity and Frequency Spectra Plots

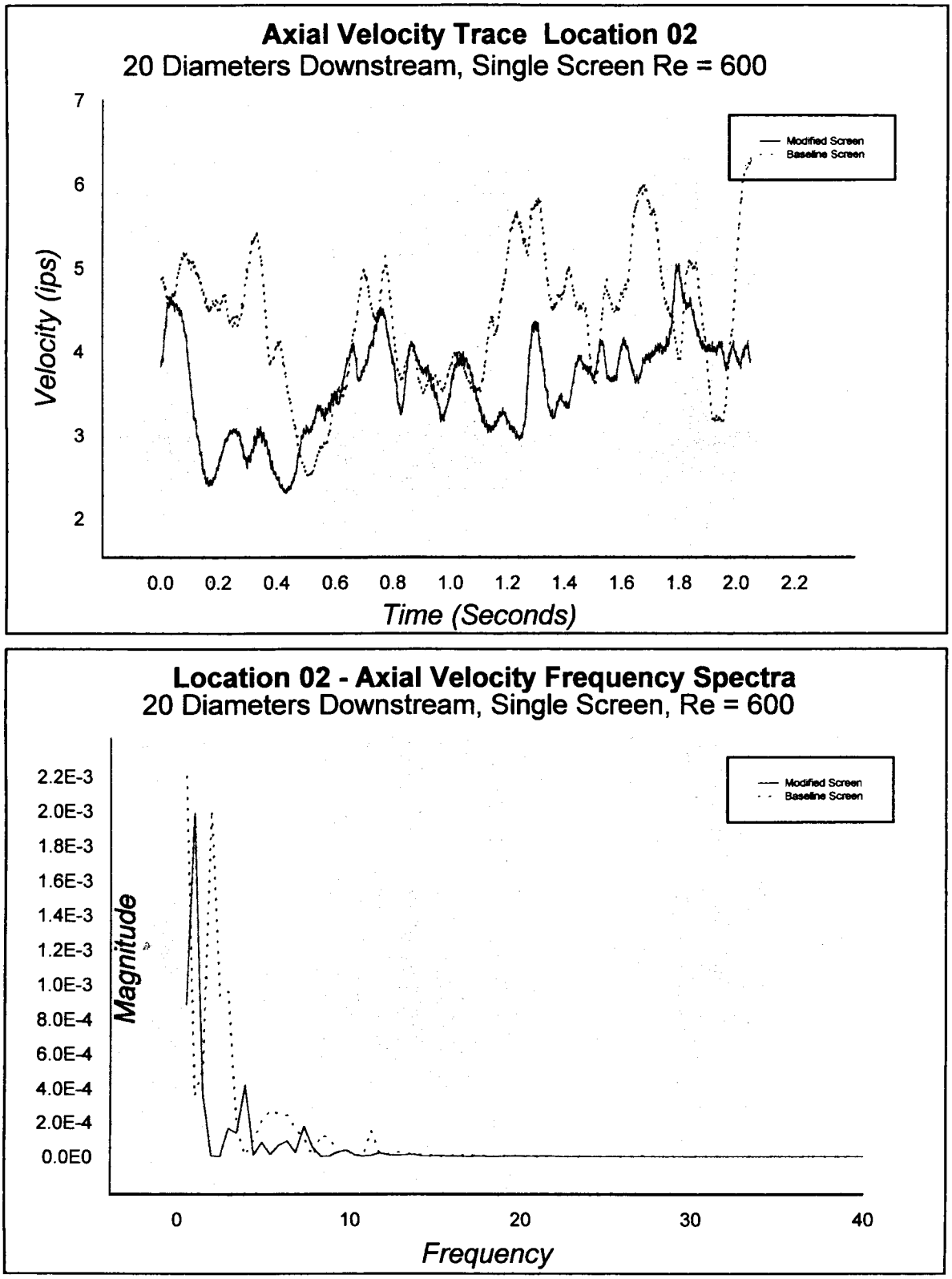


Figure D-2. Single Screen Location 02, 20 Diameters Downsteam
Axial Velocity and Frequency Spectra Plots

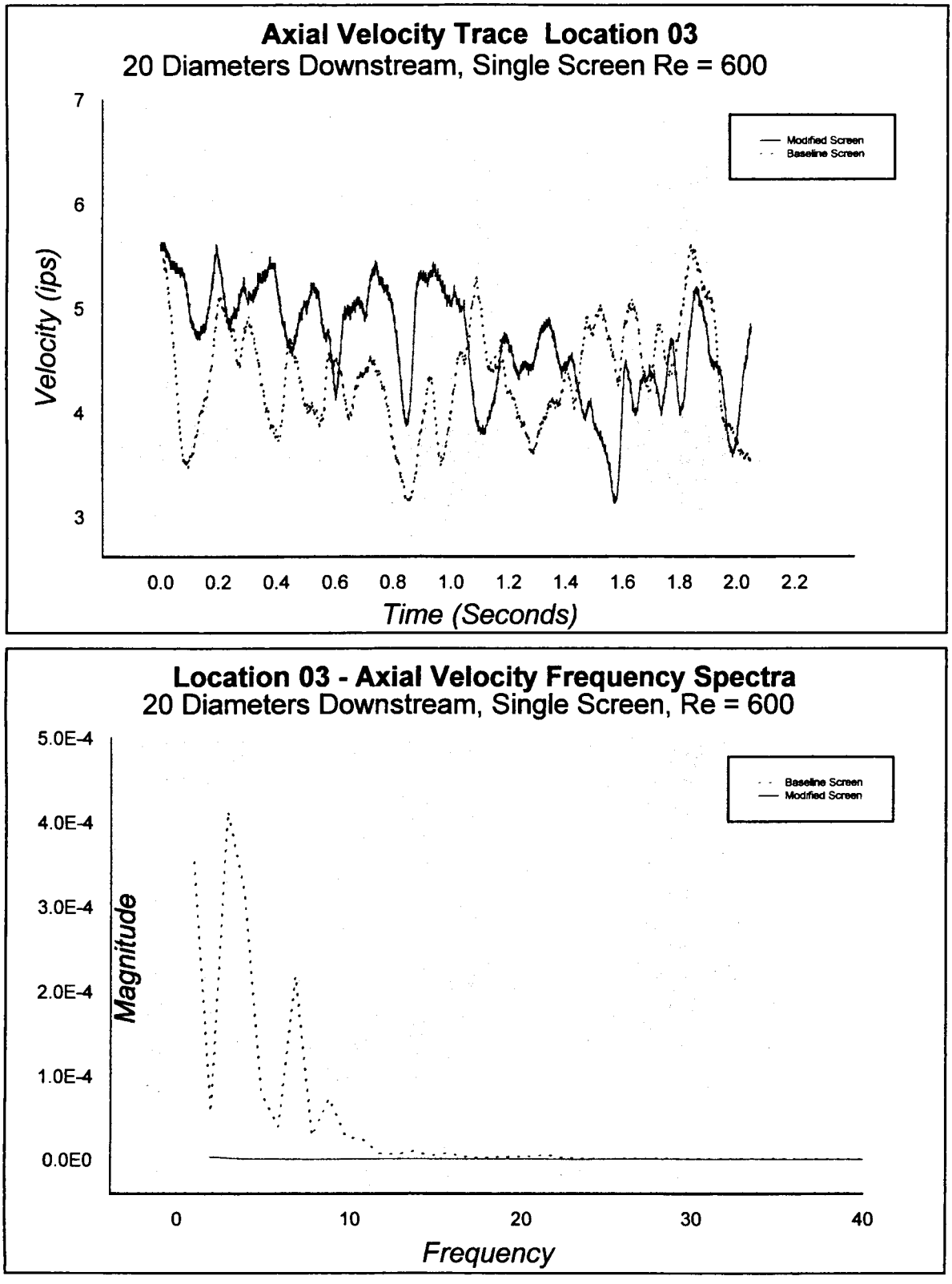
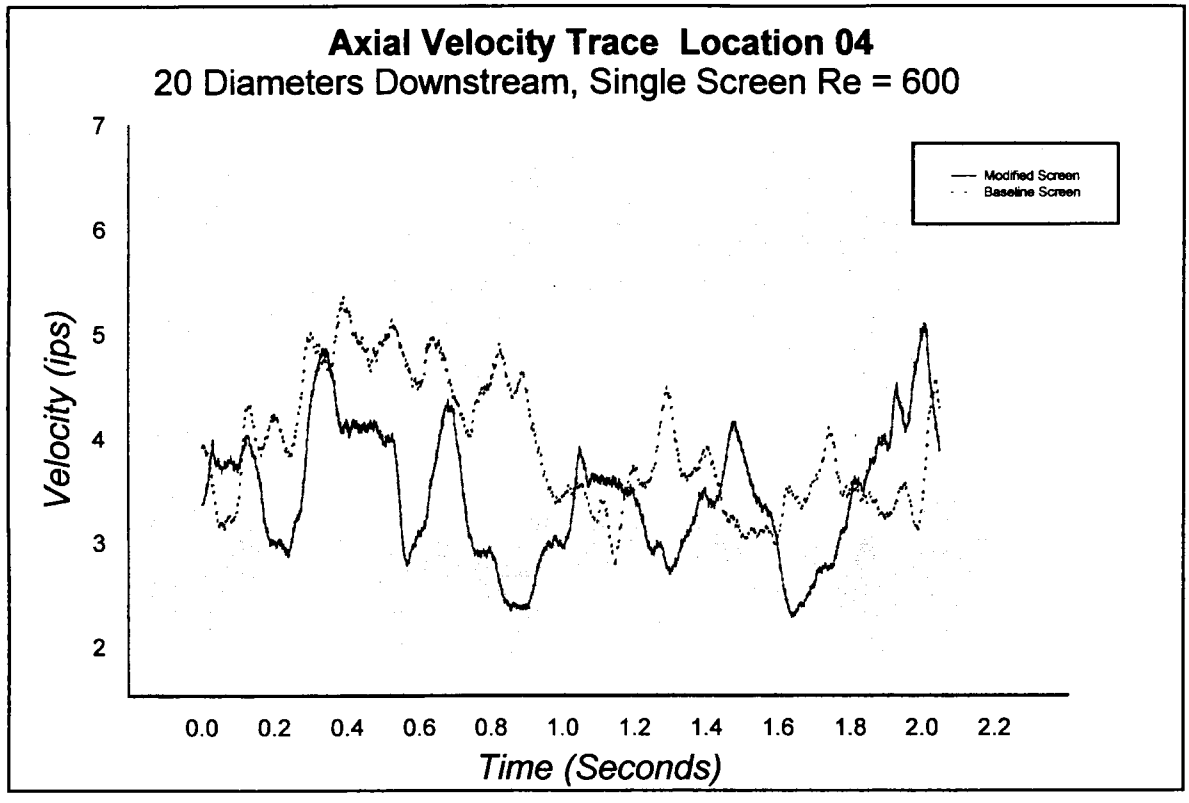


Figure D-3. Single Screen Location 03, 20 Diameters Downsteam
Axial Velocity and Frequency Spectra Plots



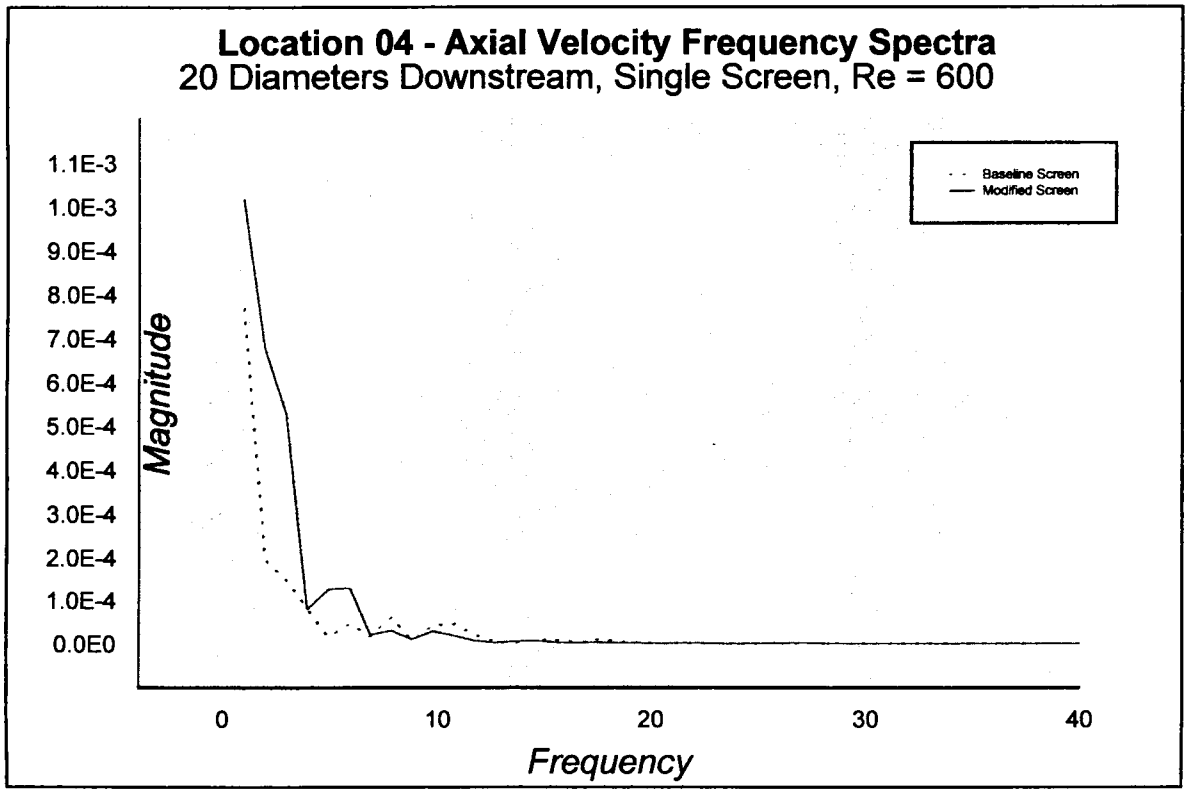


Figure D-4. Single Screen Location 04, 20 Diameters Downsteam
Axial Velocity and Frequency Spectra Plots

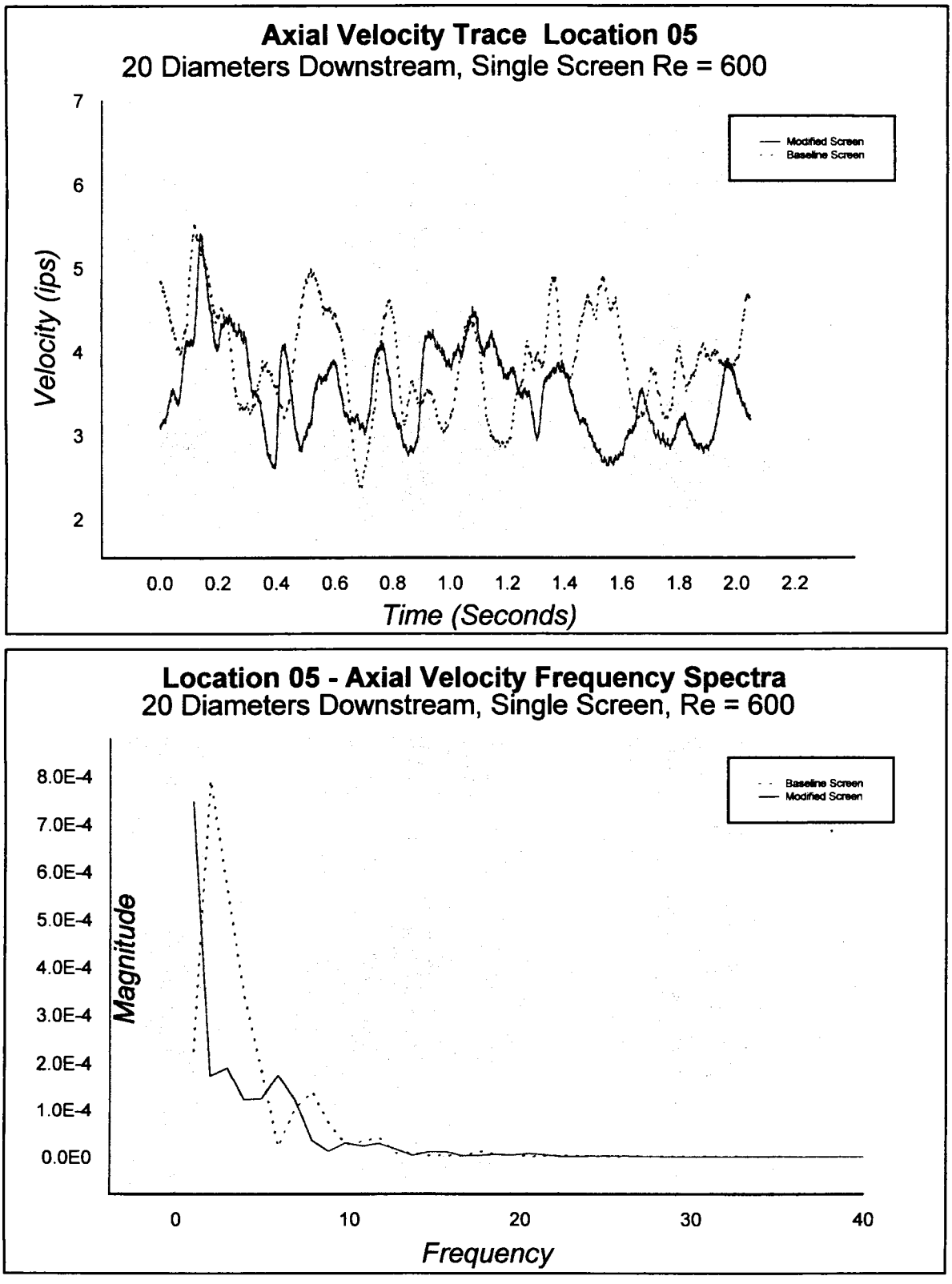


Figure D-5. Single Screen Location 05, 20 Diameters Downsteam
Axial Velocity and Frequency Spectra Plots

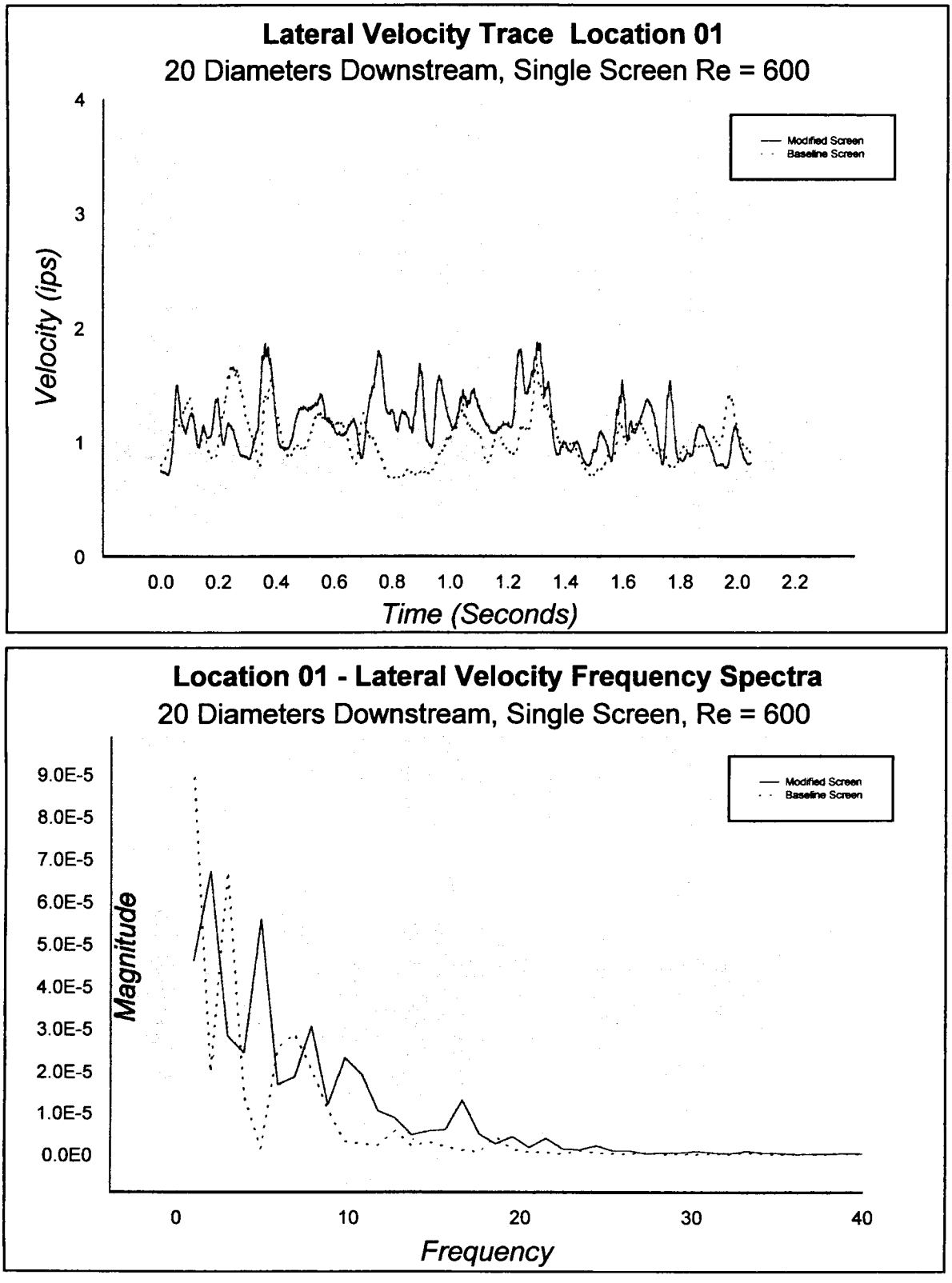


Figure D-6. Single Screen Location 01, 20 Diameters Downsteam Lateral Velocity and Frequency Spectra Plots

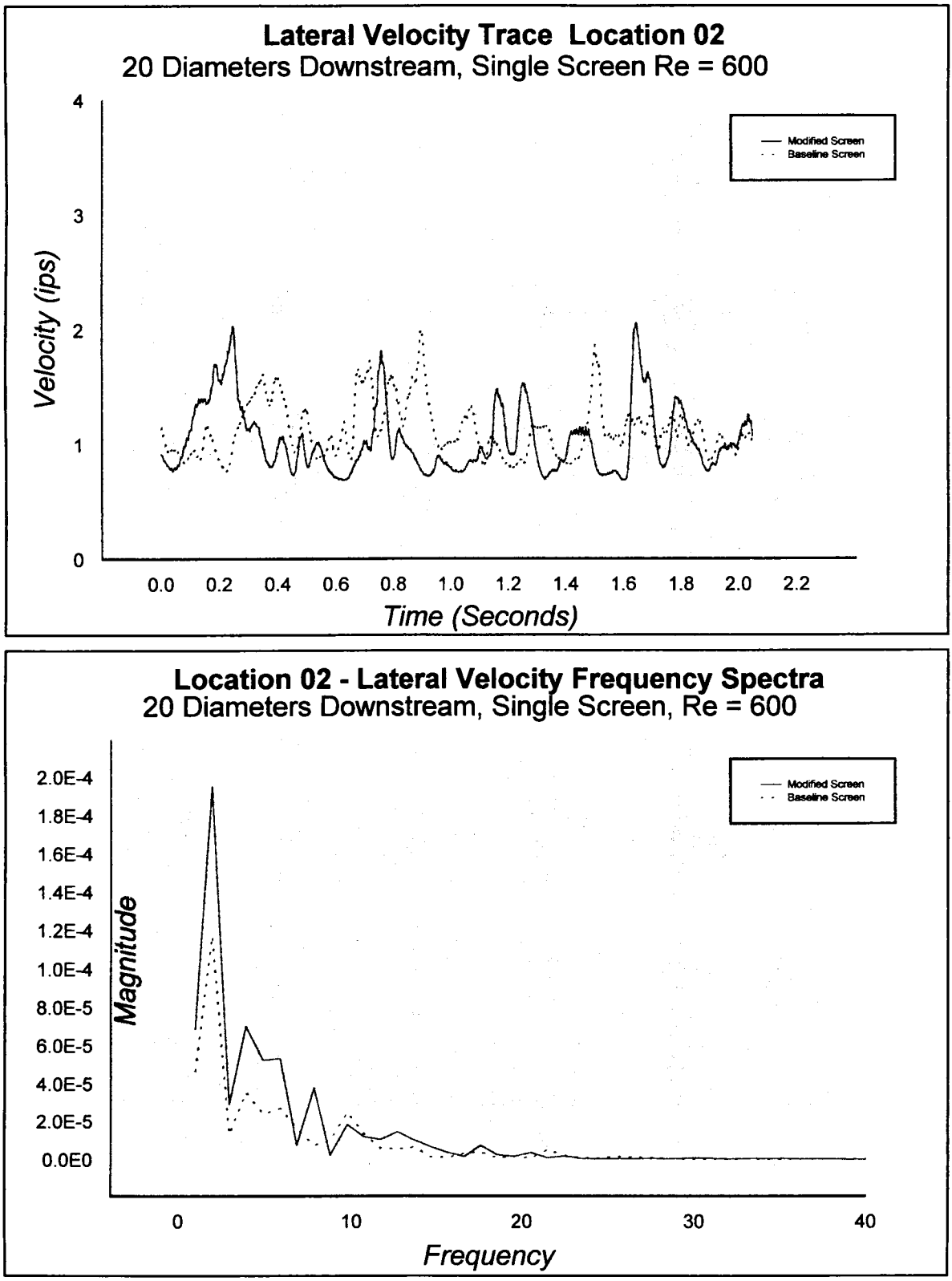
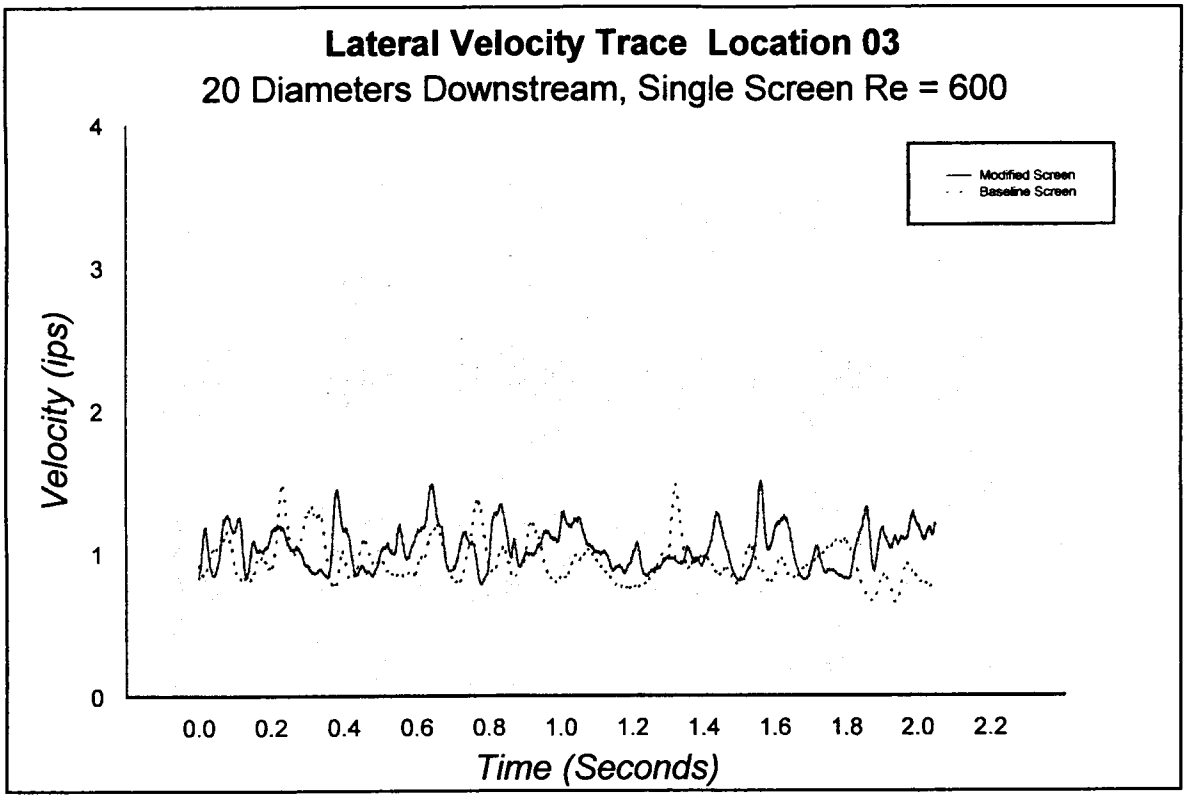


Figure D-7. Single Screen Location 02, 20 Diameters Downsteam Lateral Velocity and Frequency Spectra Plots



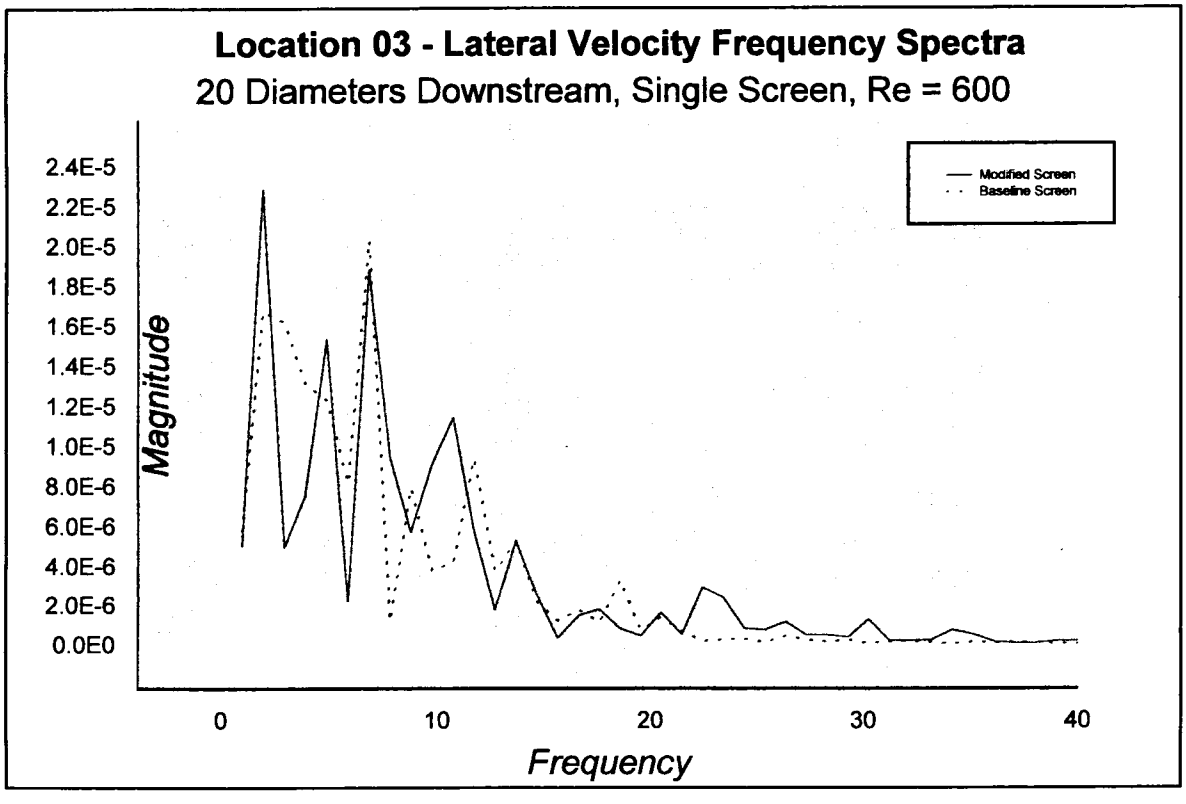


Figure D-8. Single Screen, Location 03, 20 Diameters Downsteam
Lateral Velocity and Frequency Spectra Plots

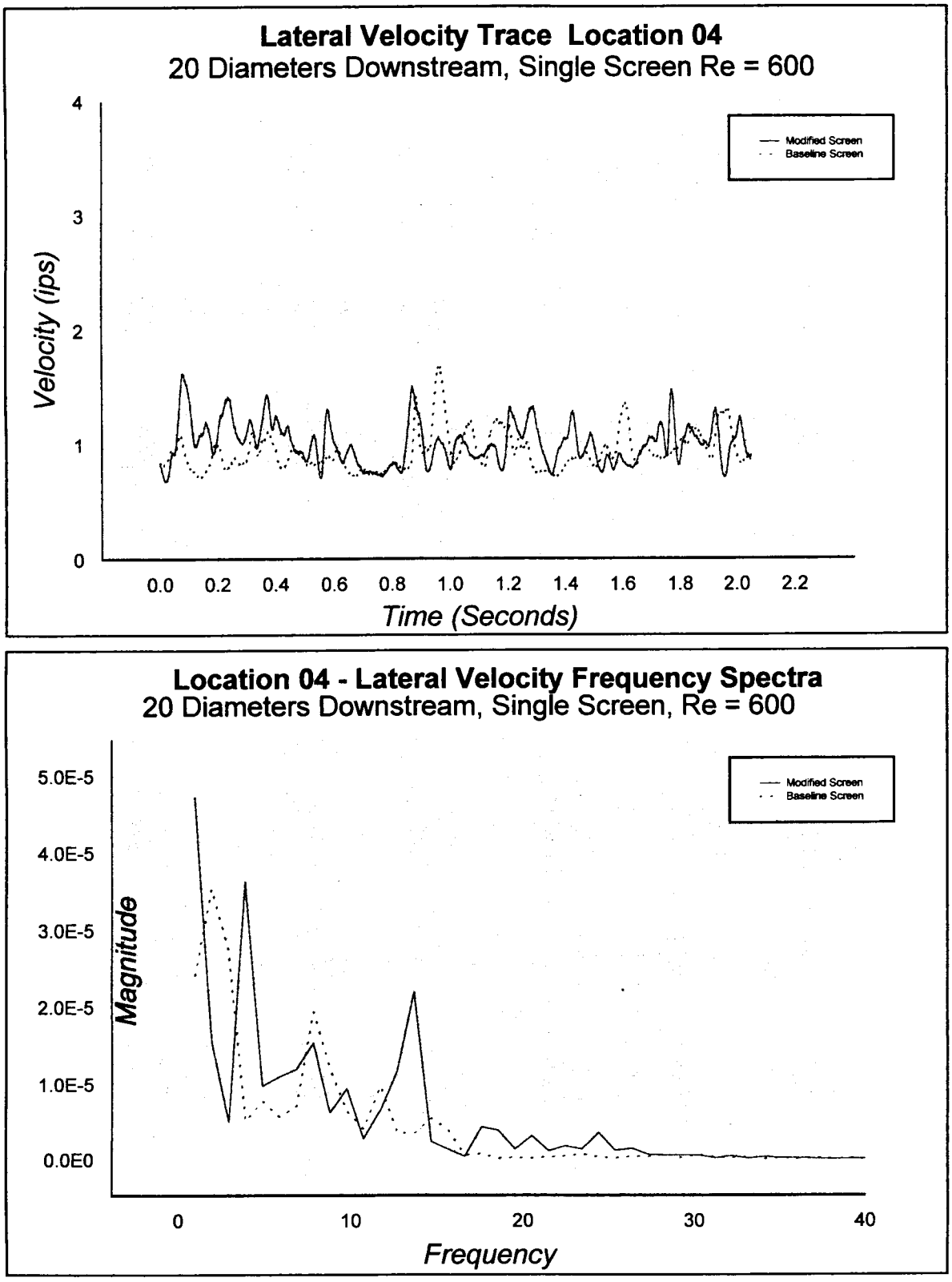


Figure D-9. Single Screen, Location 04, 20 Diameters Downsteam
Lateral Velocity and Frequency Spectra Plots

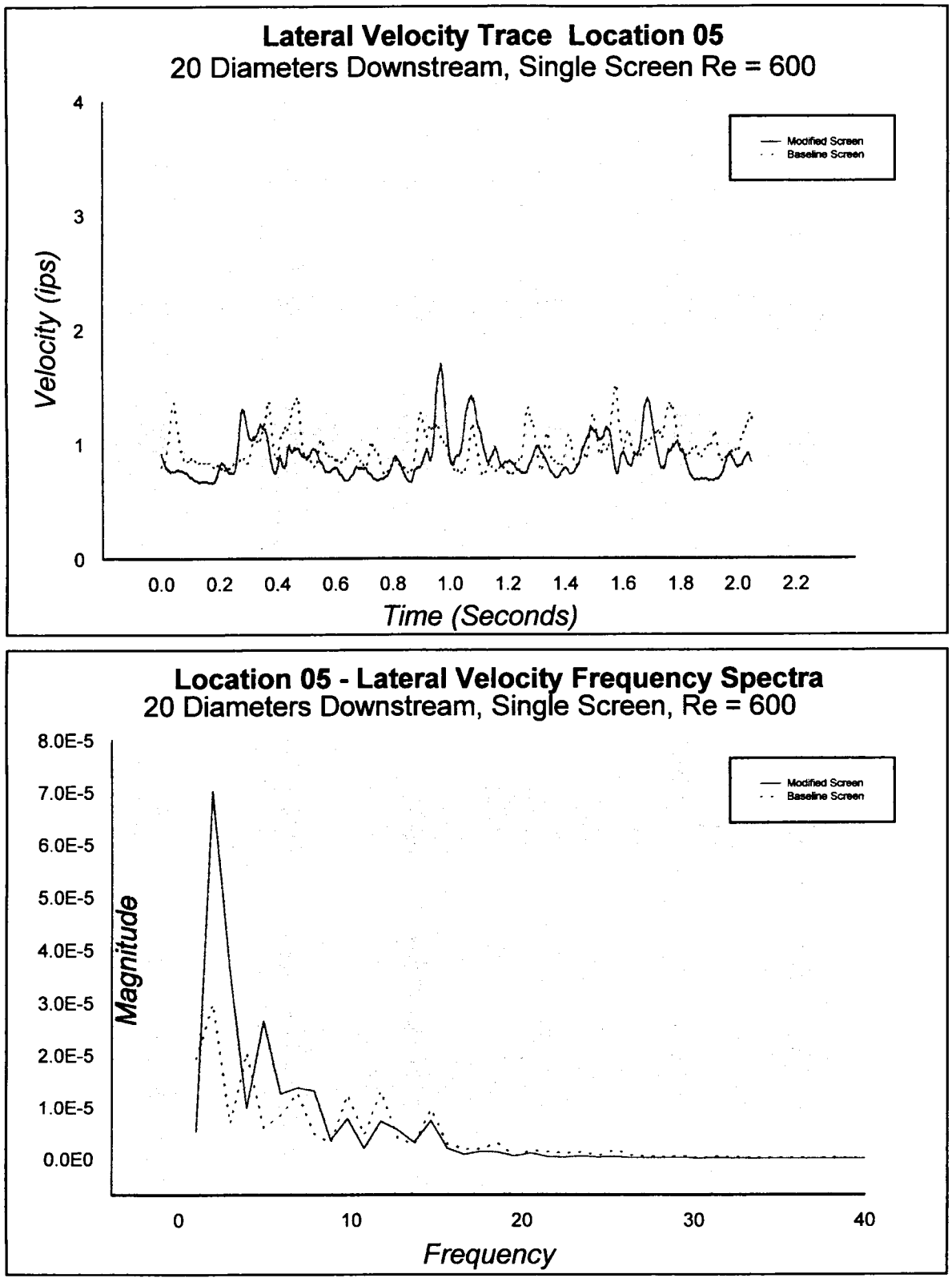


Figure D-10. Single Screen, Location 05, 20 Diameters Downsteam Lateral Velocity and Frequency Spectra Plots

20 Diameters Downstream, Location 01, Re=600

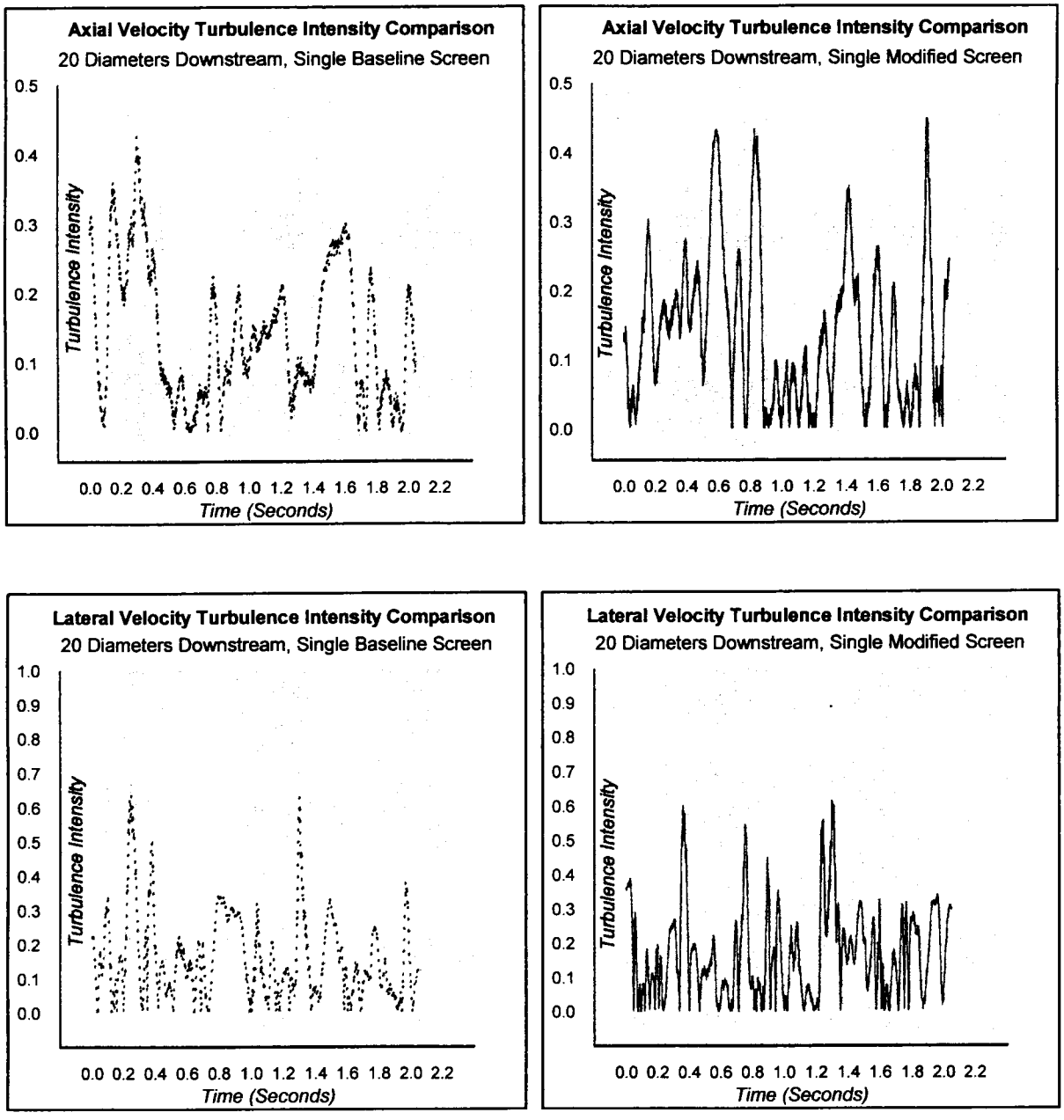


Figure D-11. Single Screen, Location 01, 20 Diameters Downsteam
Axial and Lateral Turbulence Intensity Plots

20 Diameters Downstream, Location 02, Re=600

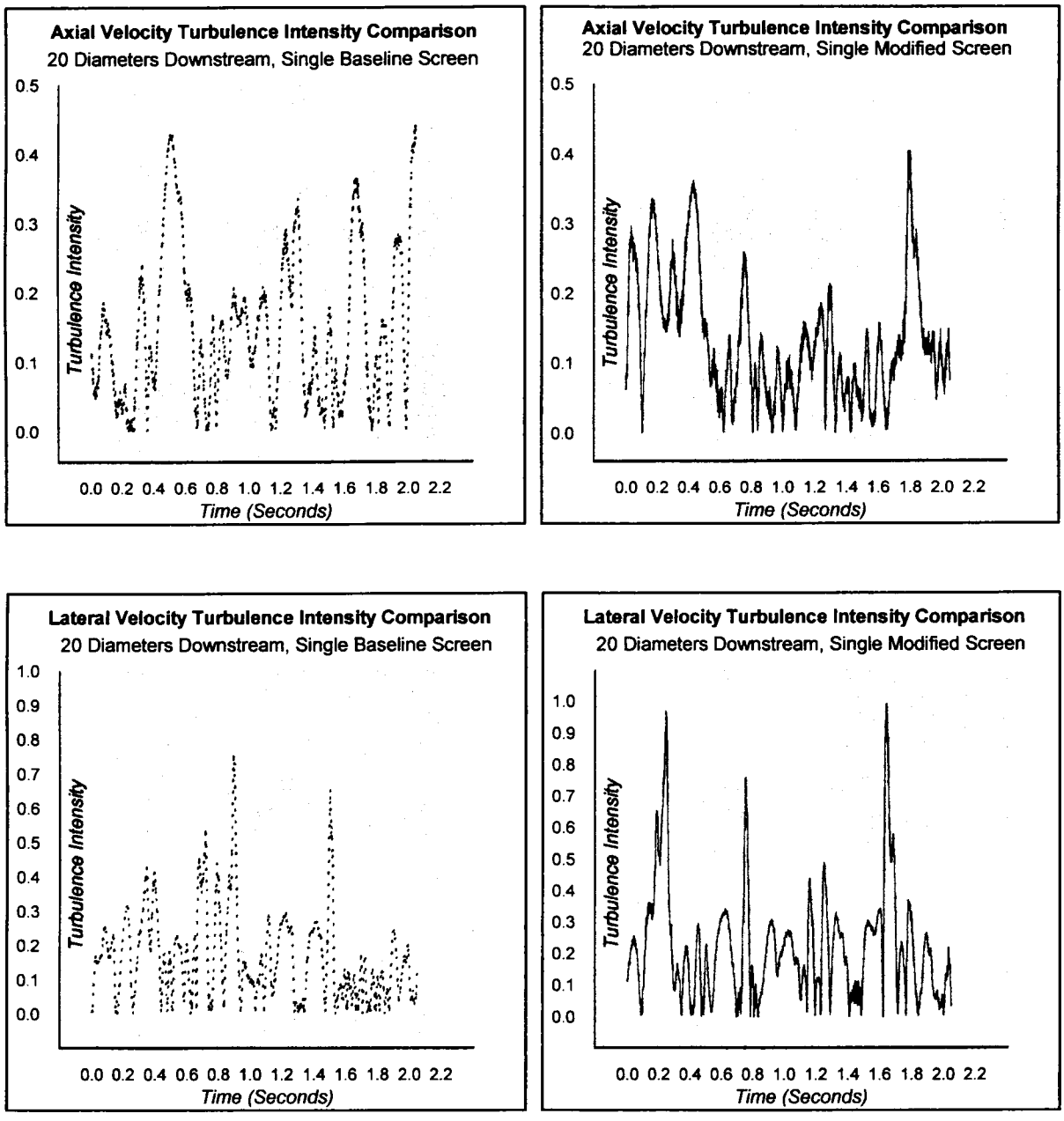


Figure D-12. Single Screen, Location 02, 20 Diameters Downsteam
Axial and Lateral Turbulence Intensity Plots

20 Diameters Downstream, Location 03, Re=600

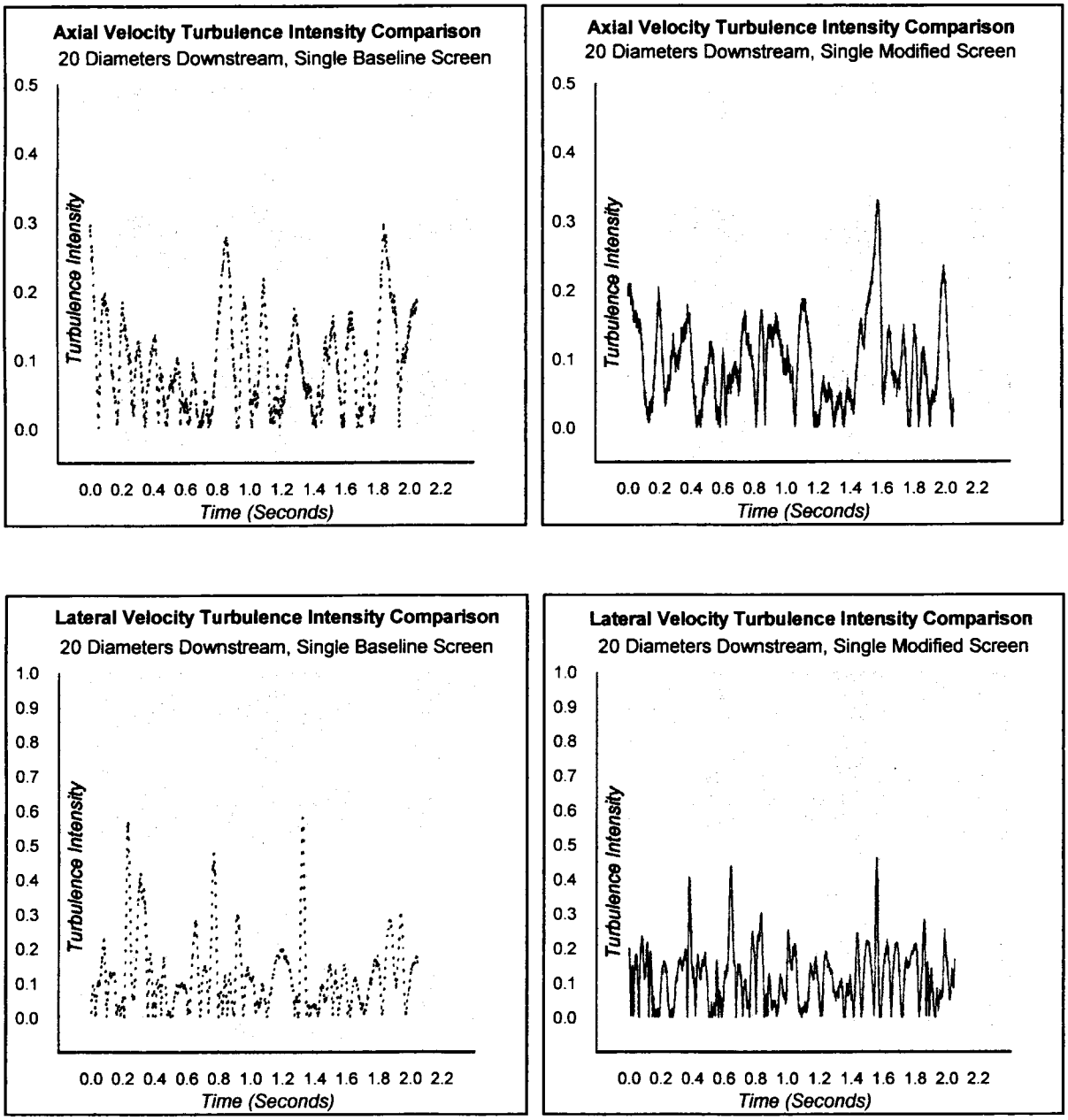
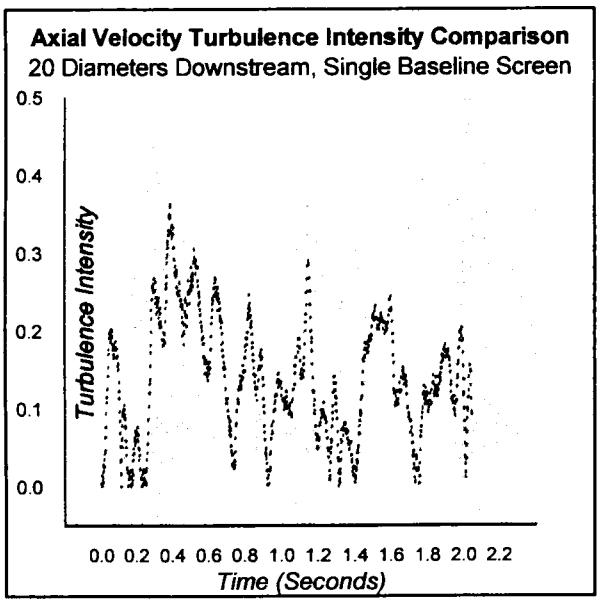
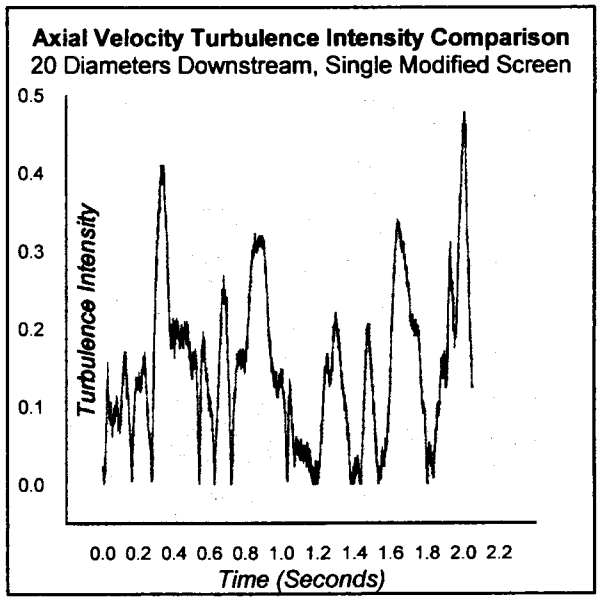
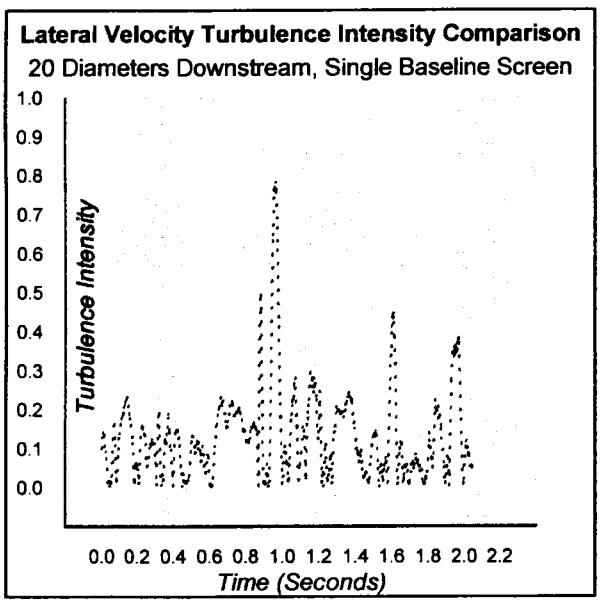


Figure D-13. Single Screen, Location 03, 20 Diameters Downsteam
Axial and Lateral Turbulence Intensity Plots

20 Diameters Downstream, Location 04, Re=600







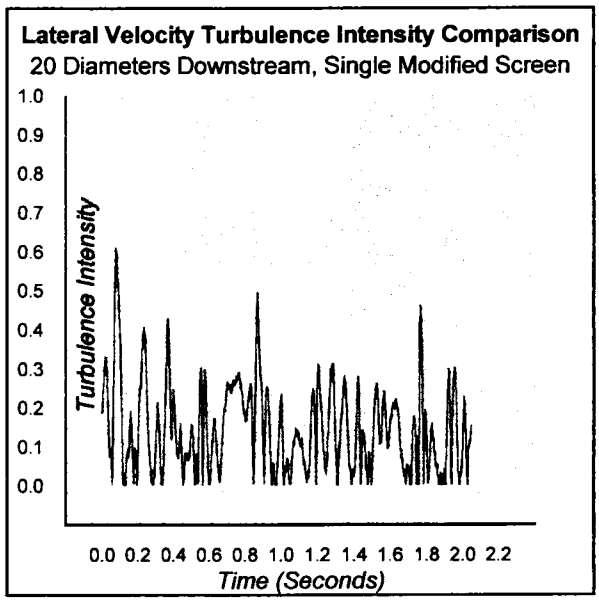
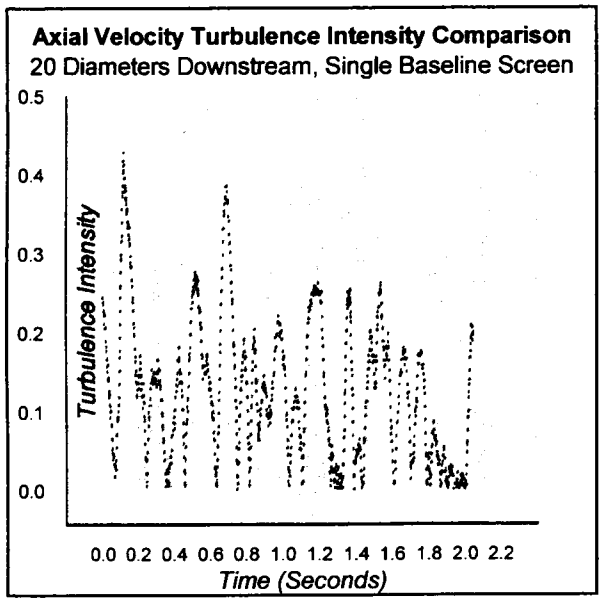
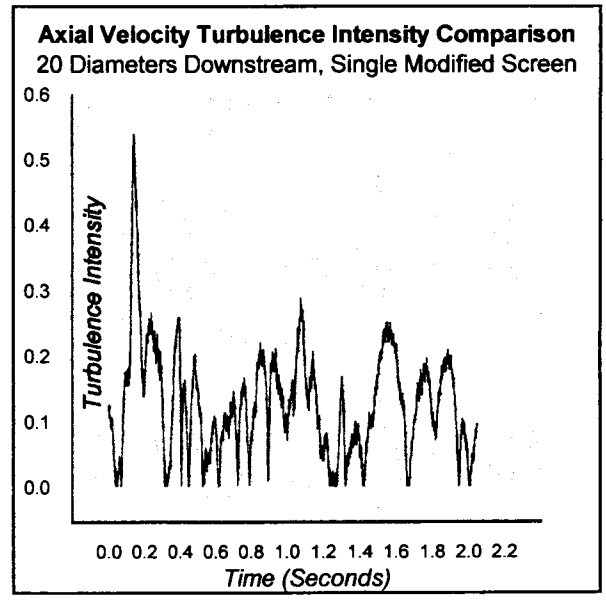
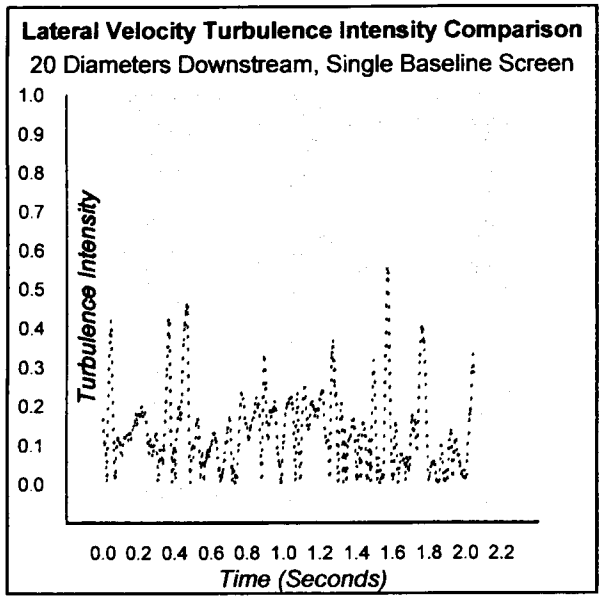


Figure D-14. Single Screen, Location 04, 20 Diameters Downsteam
Axial and Lateral Turbulence Intensity Plots

20 Diameters Downstream, Location 05, Re=600







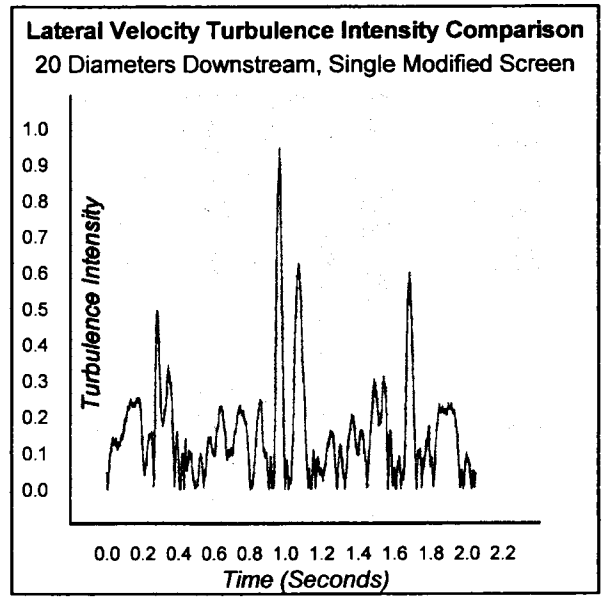


Figure D-15. Single Screen, Location 05, 20 Diameters Downsteam
Axial and Lateral Turbulence Intensity Plots

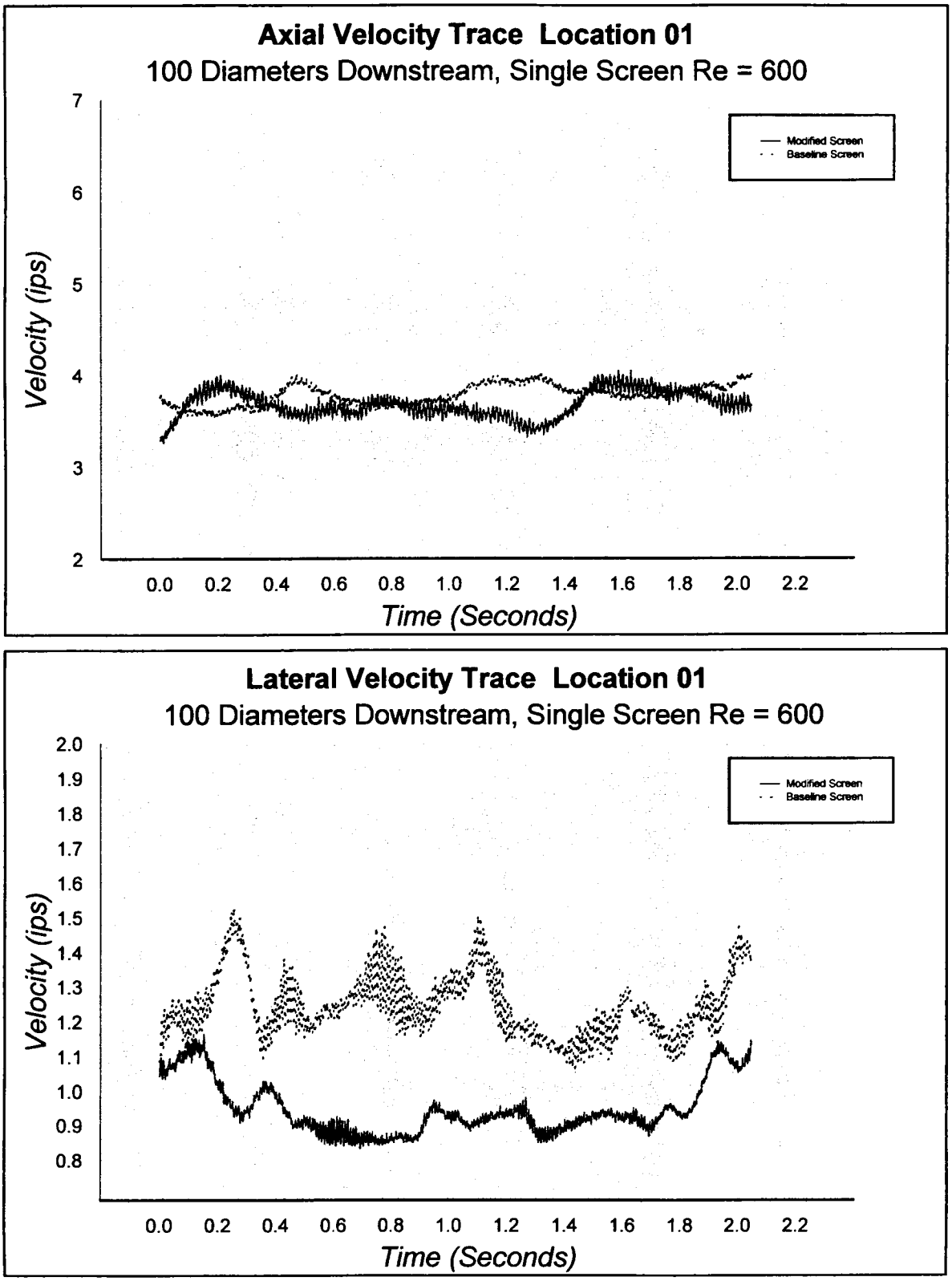


Figure D-16. Single Screen Location 01, 100 Diameters Downsteam

Axial and Lateral Velocity Plots

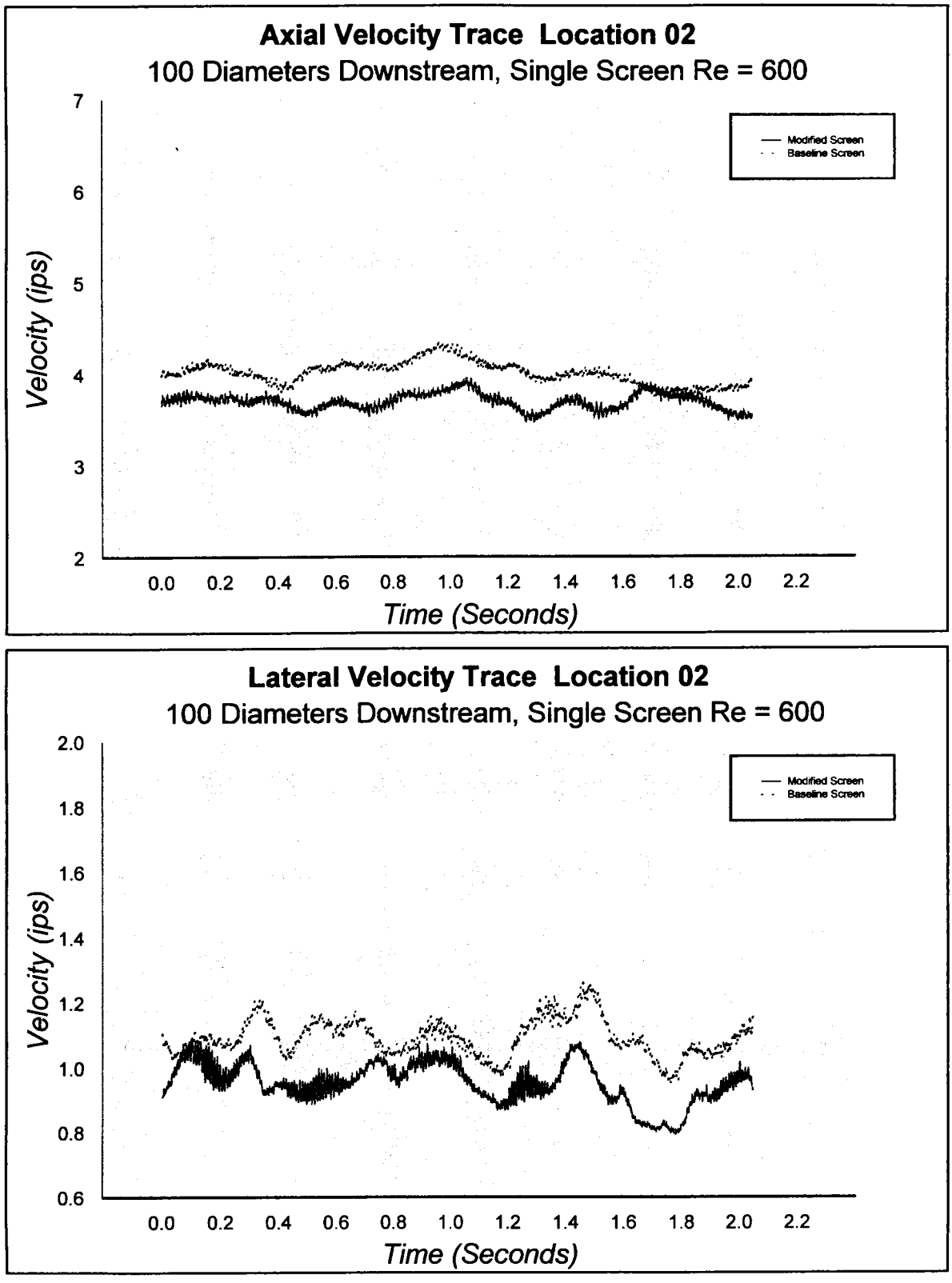


Figure D-17. Single Screen Location 02, 100 Diameters Downsteam

Axial and Lateral Velocity Plots

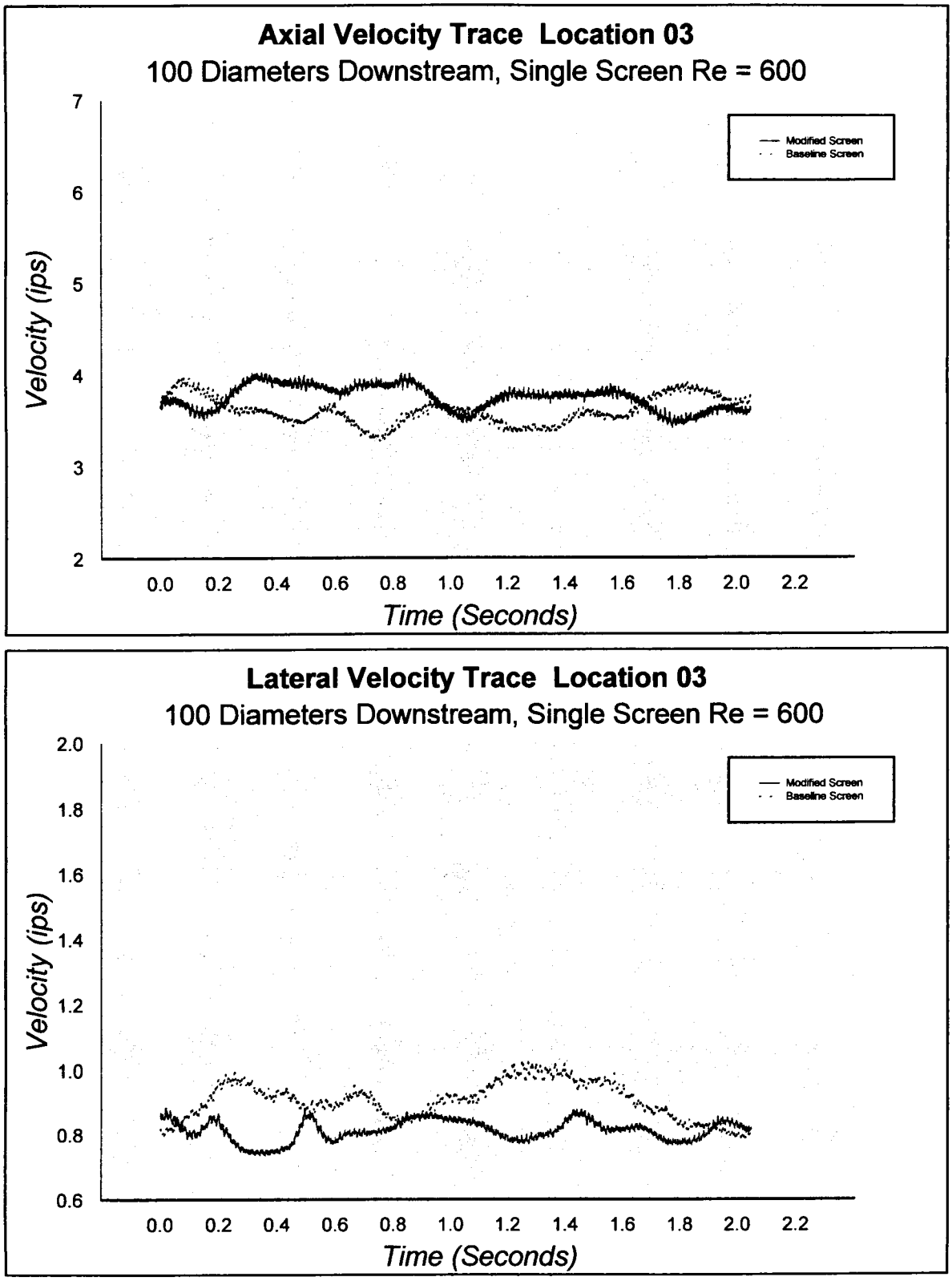


Figure D-18. Single Screen Location 03, 100 Diameters Downsteam

Axial and Lateral Velocity Plots

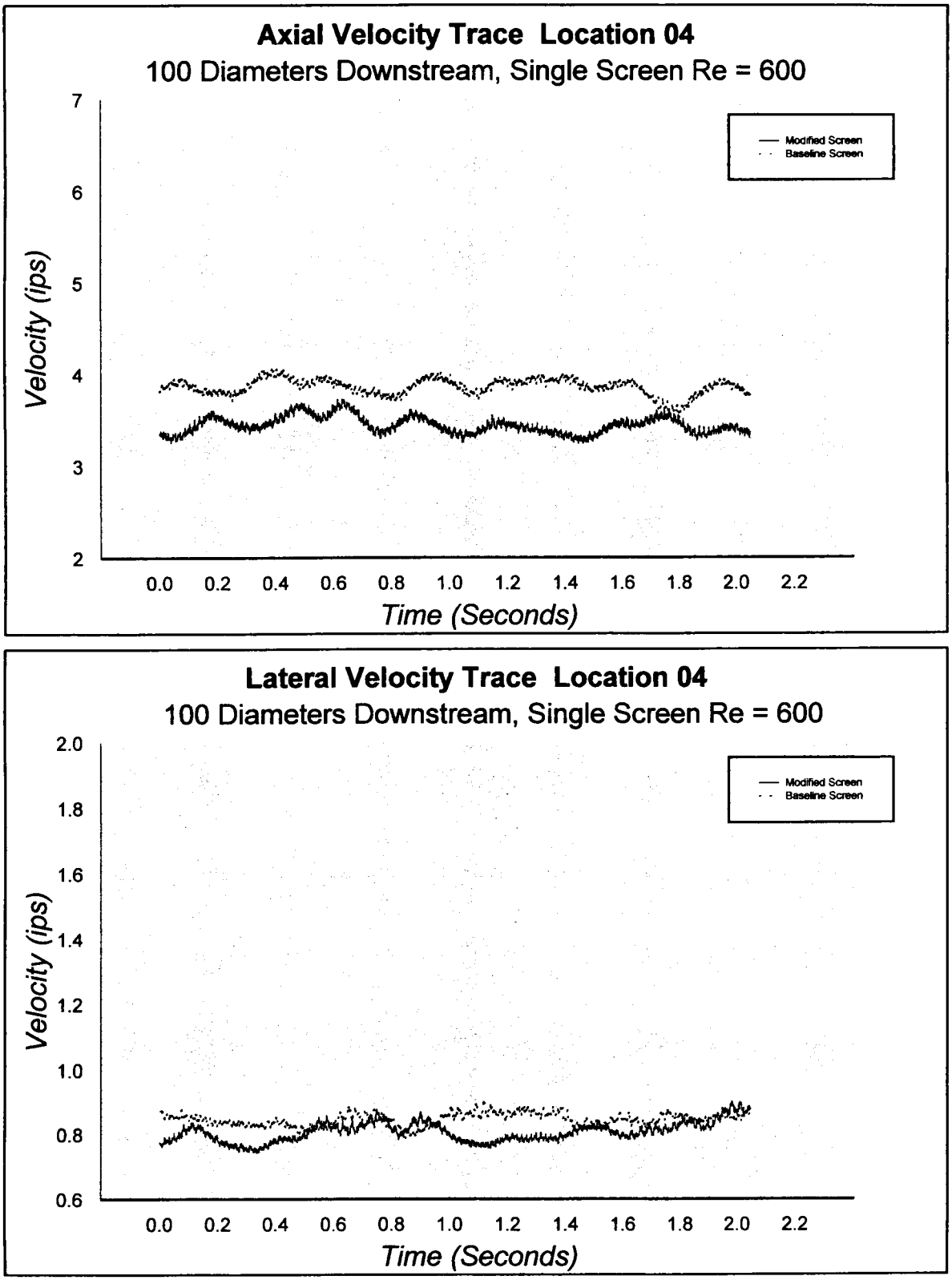


Figure D-19. Single Screen Location 04, 100 Diameters Downsteam

Axial and Lateral Velocity Plots

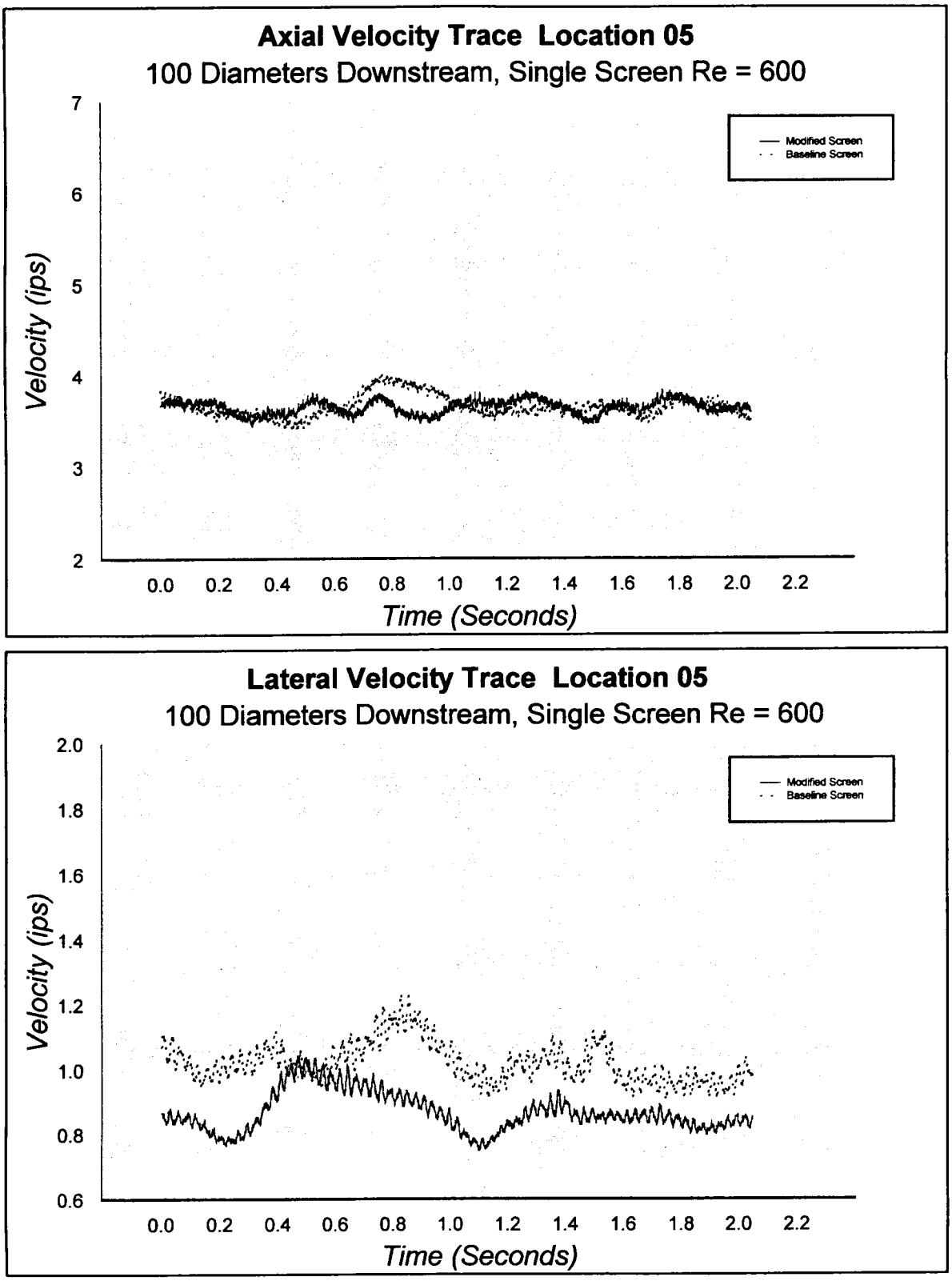


Figure D-20. Single Screen Location 05, 100 Diameters Downsteam

Axial and Lateral Velocity Plots

100 Diameters Downstream, Location 01, Re=600

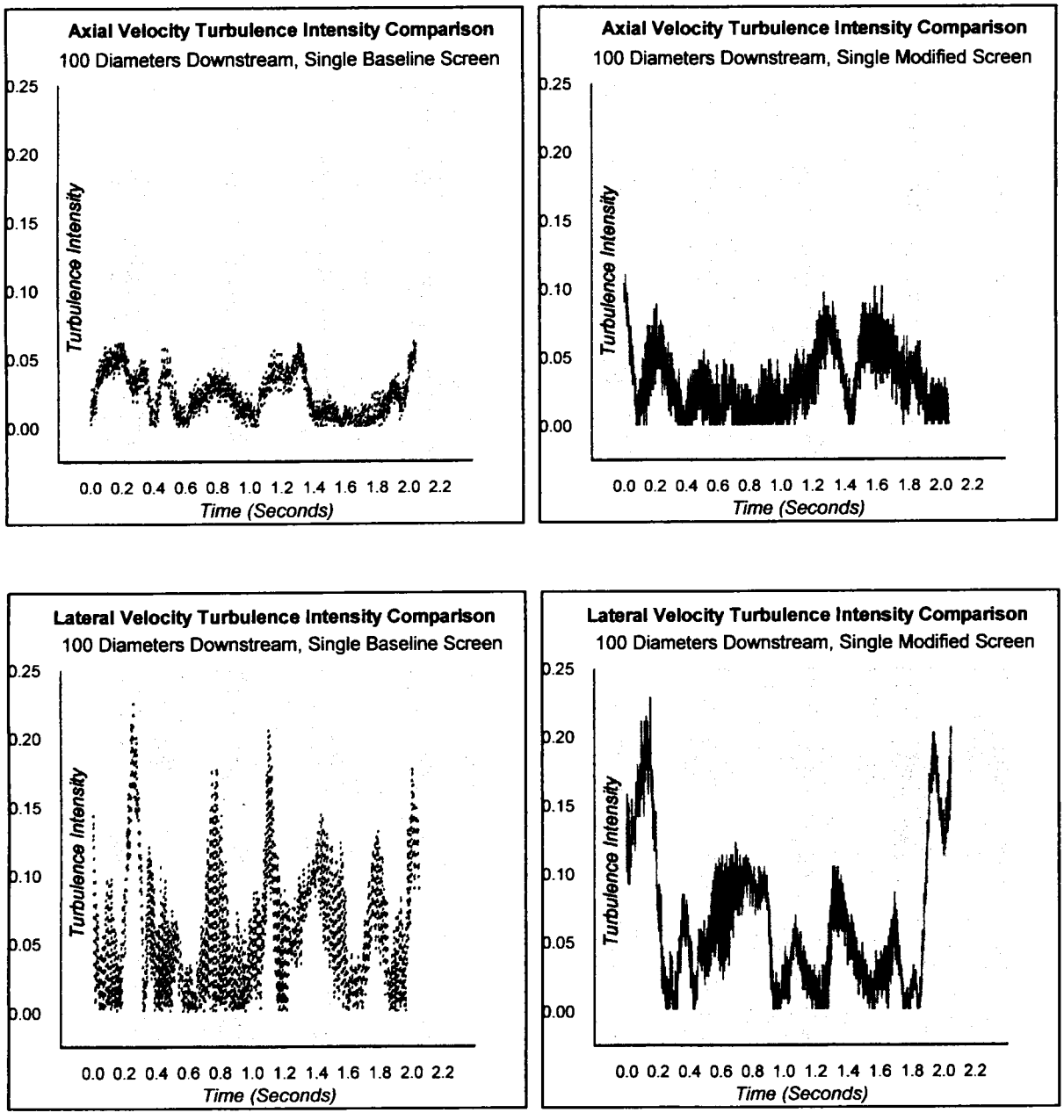


Figure D-21. Single Screen, Location 01, 100 Diameters Downsteam
Axial and Lateral Turbulence Intensity Plots

100 Diameters Downstream, Location 02, Re=600

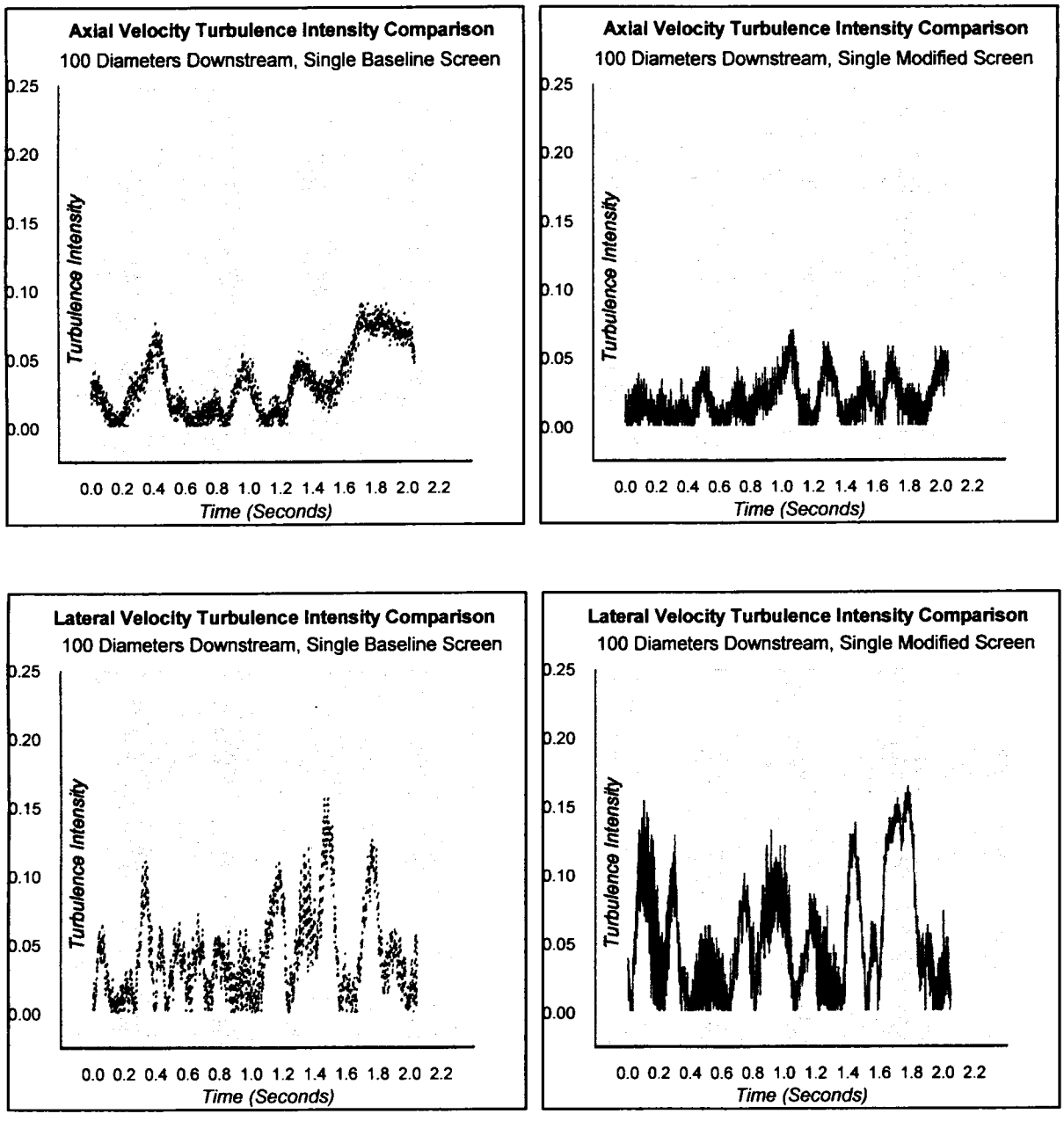


Figure D-22. Single Screen, Location 02, 100 Diameters Downsteam
Axial and Lateral Turbulence Intensity Plots

100 Diameters Downstream, Location 03, Re=600

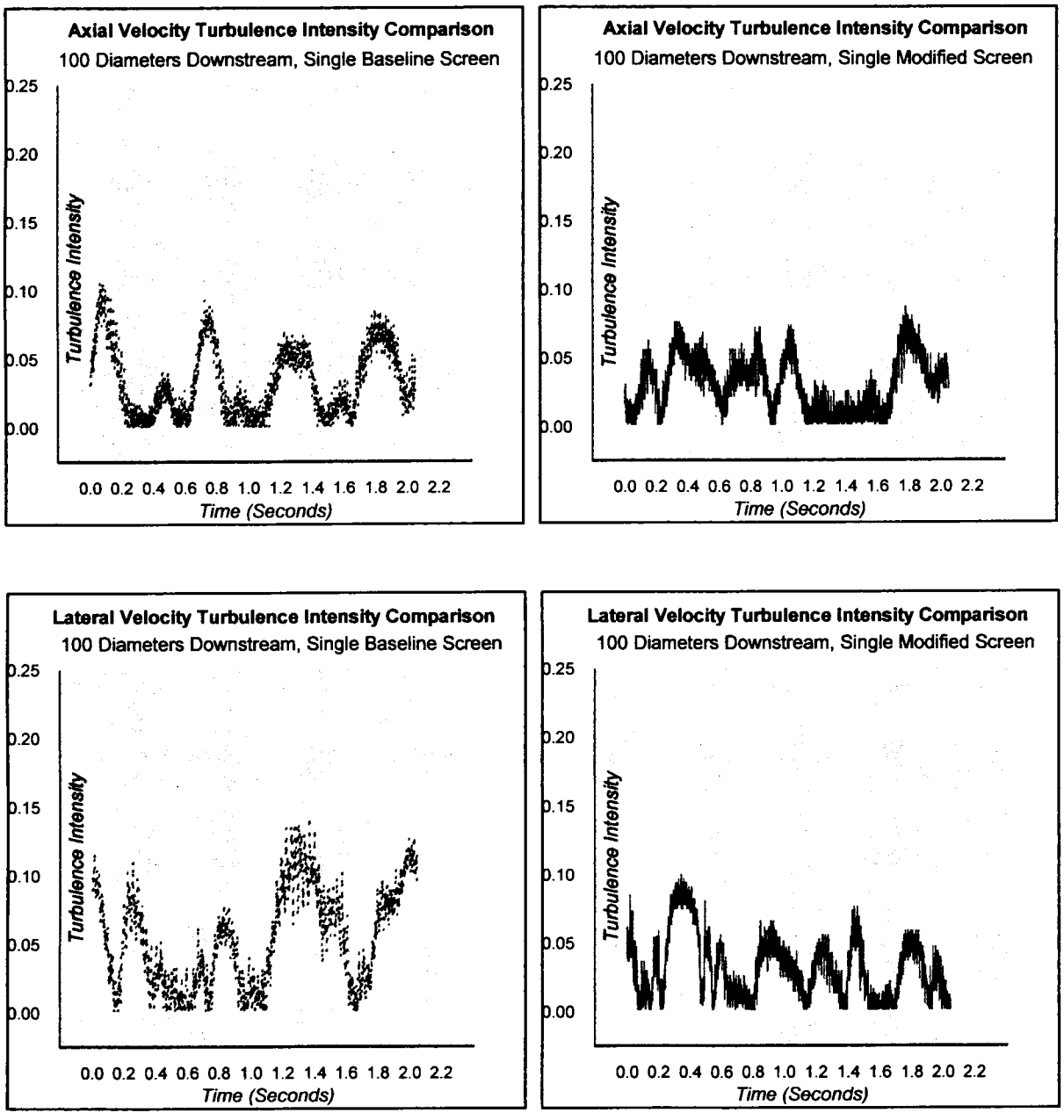


Figure D-23. Single Screen, Location 03, 100 Diameters Downsteam
Axial and Lateral Turbulence Intensity Plots

100 Diameters Downstream, Location 04, Re=600

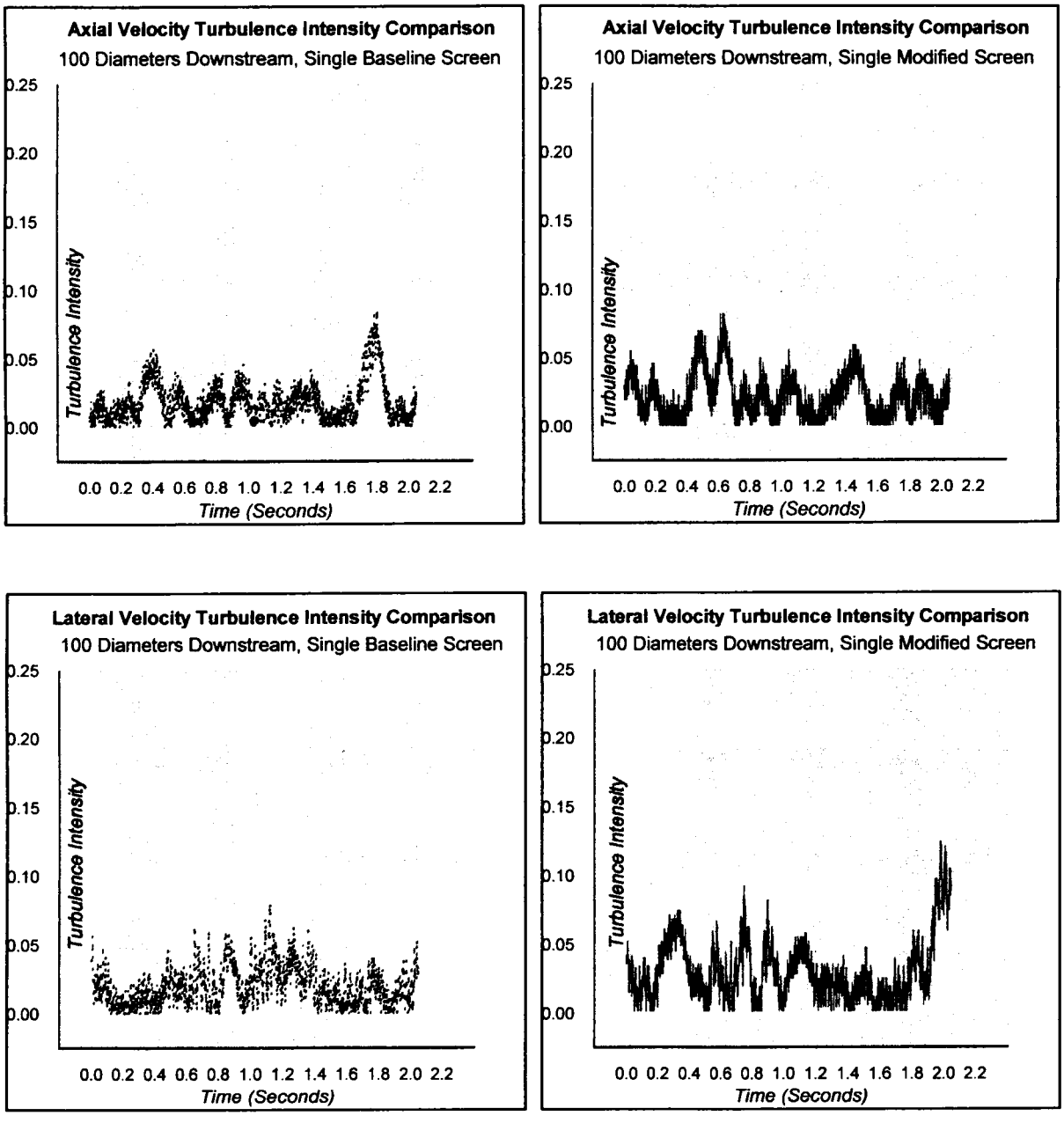


Figure D-24. Single Screen, Location 04, 100 Diameters Downsteam
Axial and Lateral Turbulence Intensity Plots

100 Diameters Downstream, Location 05, Re=600

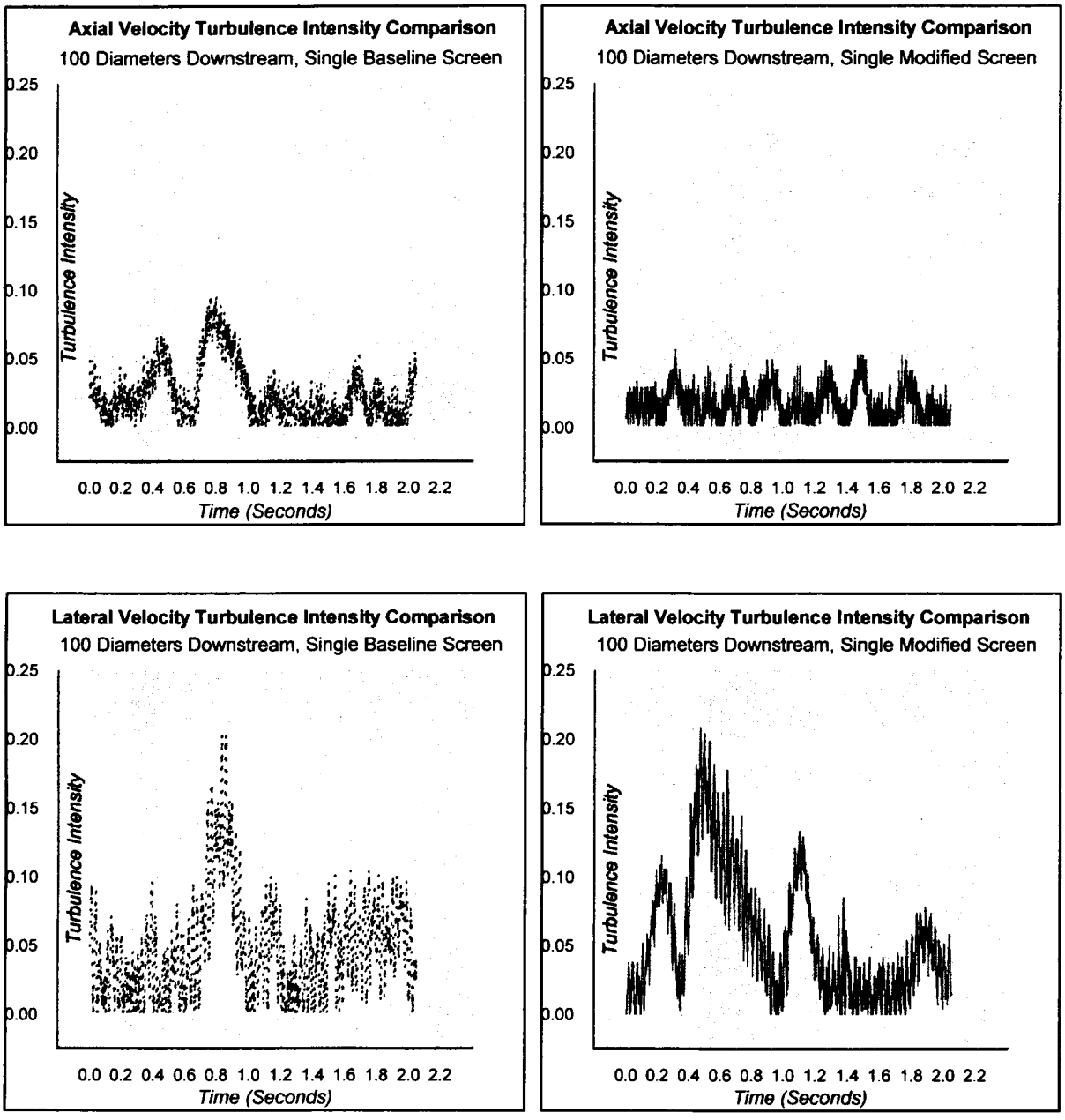


Figure D-25. Single Screen, Location 05, 100 Diameters Downsteam
Axial and Lateral Turbulence Intensity Plots

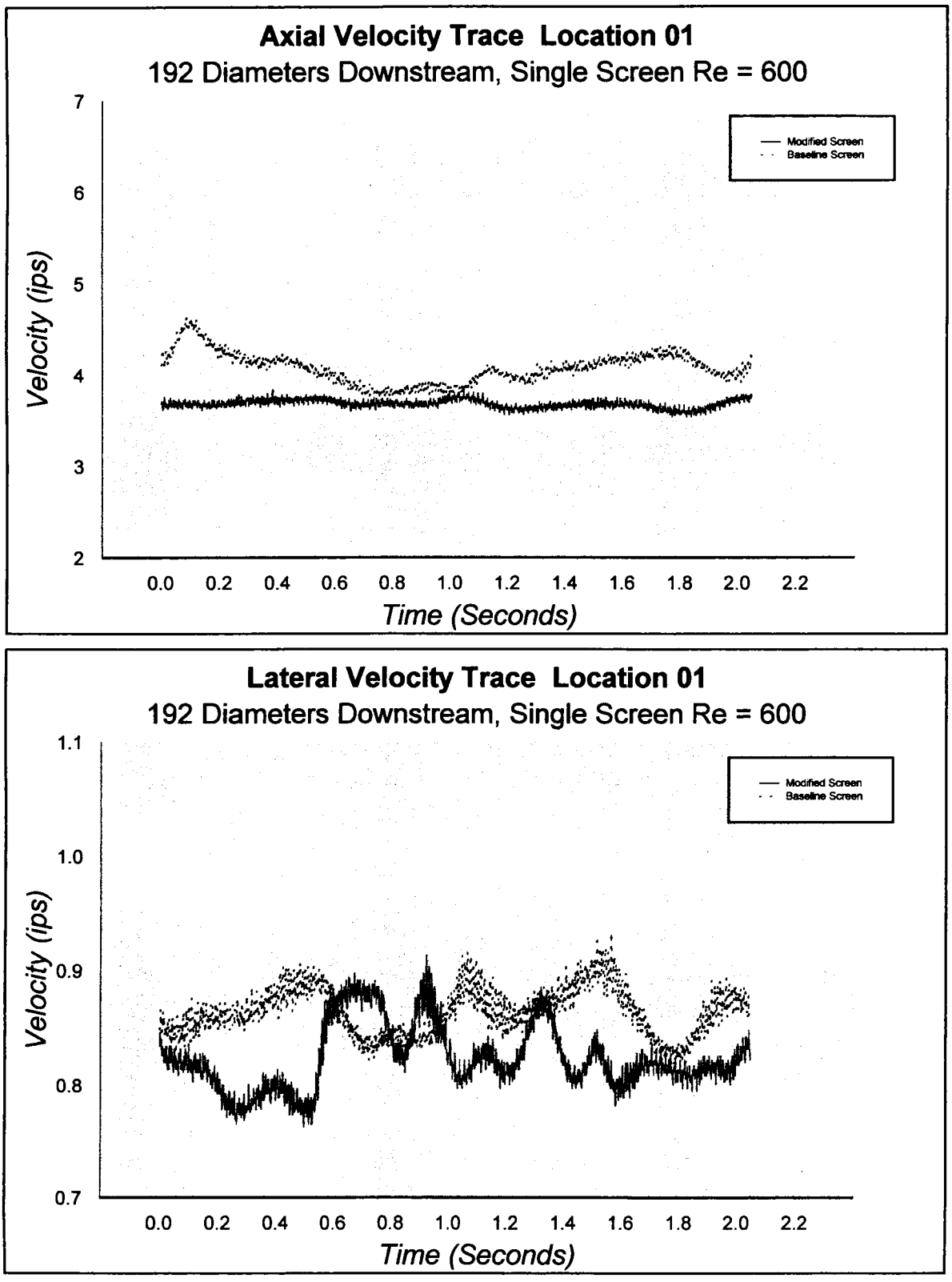
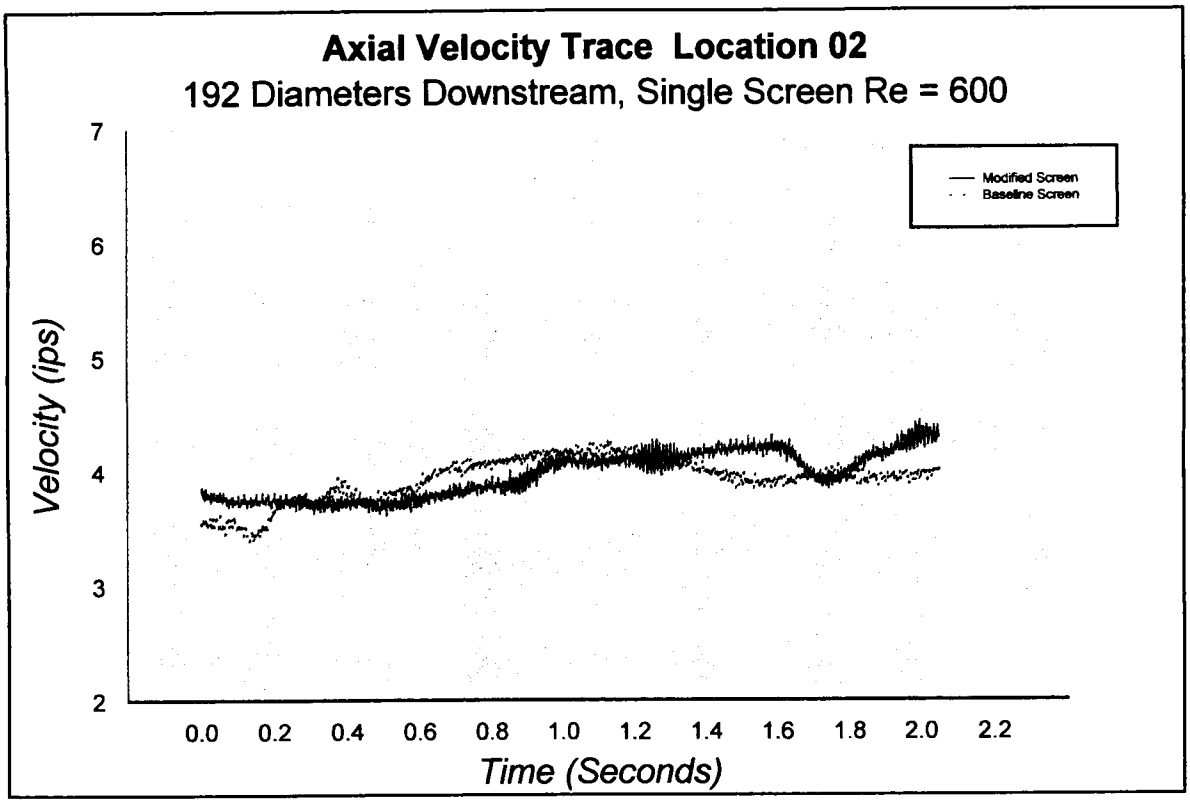


Figure D-26. Single Screen Location 01, 192 Diameters Downsteam

Axial and Lateral Velocity Plots



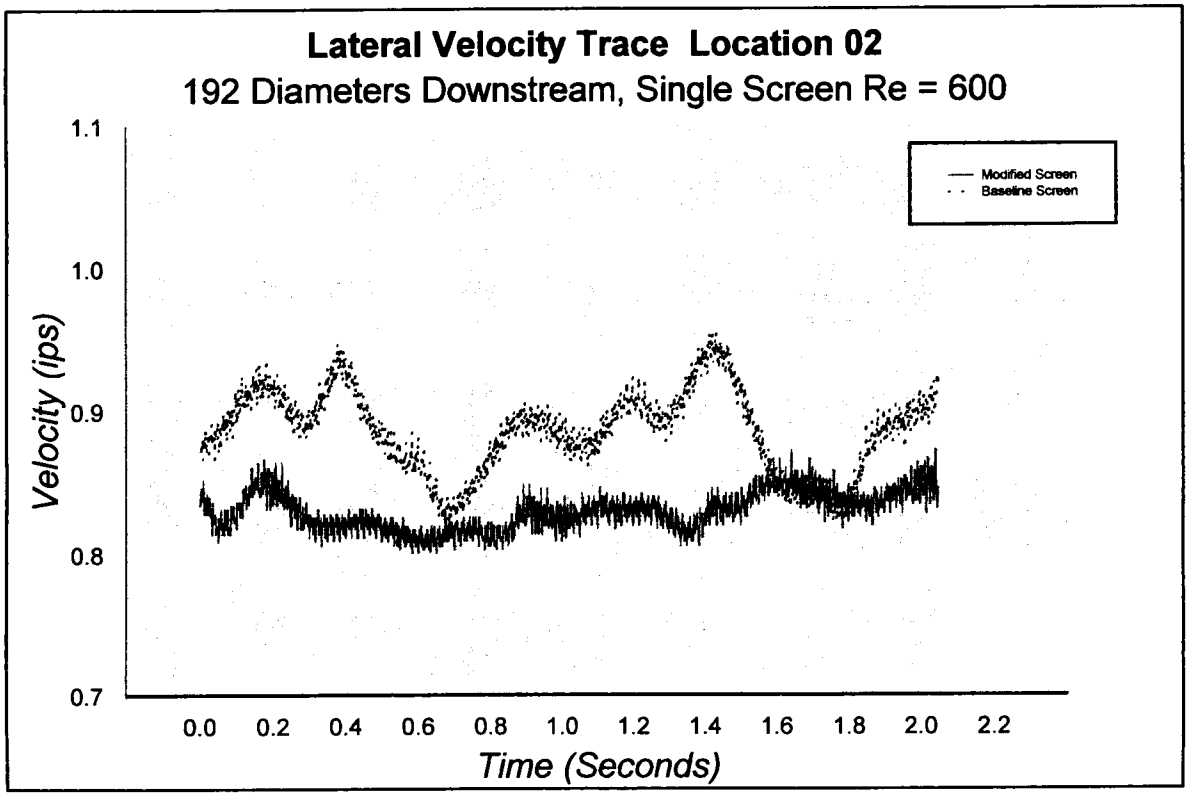


Figure D-27. Single Screen Location 02, 192 Diameters Downsteam

Axial and Lateral Velocity Plots

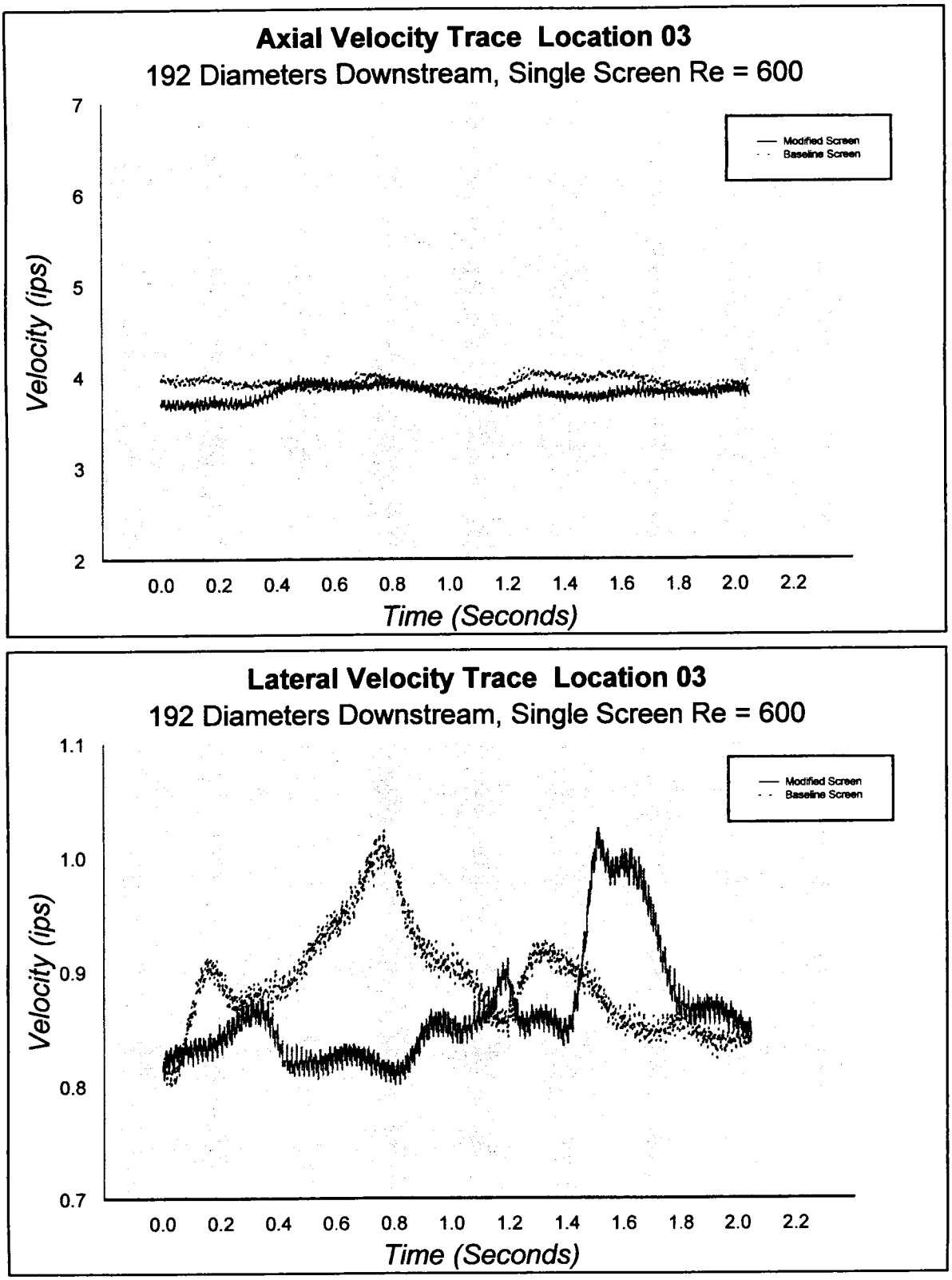
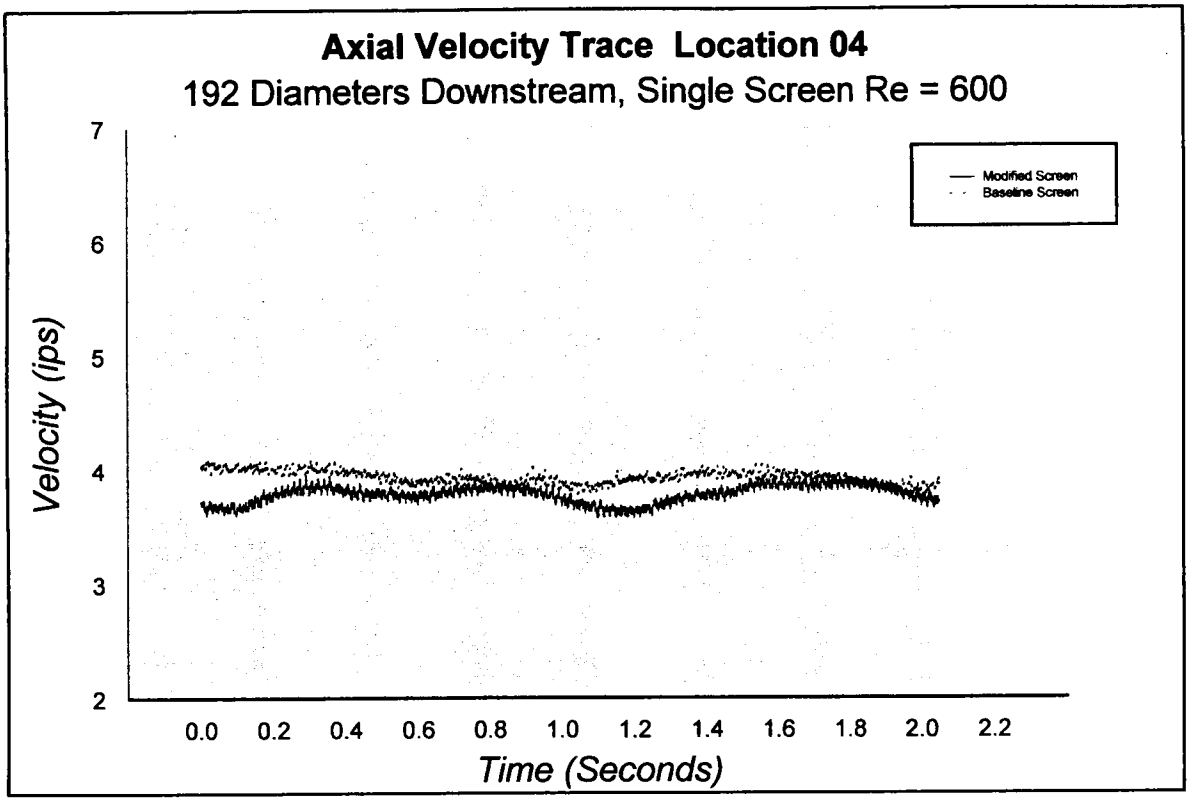


Figure D-28. Single Screen Location 03, 192 Diameters Downsteam

Axial and Lateral Velocity Plots



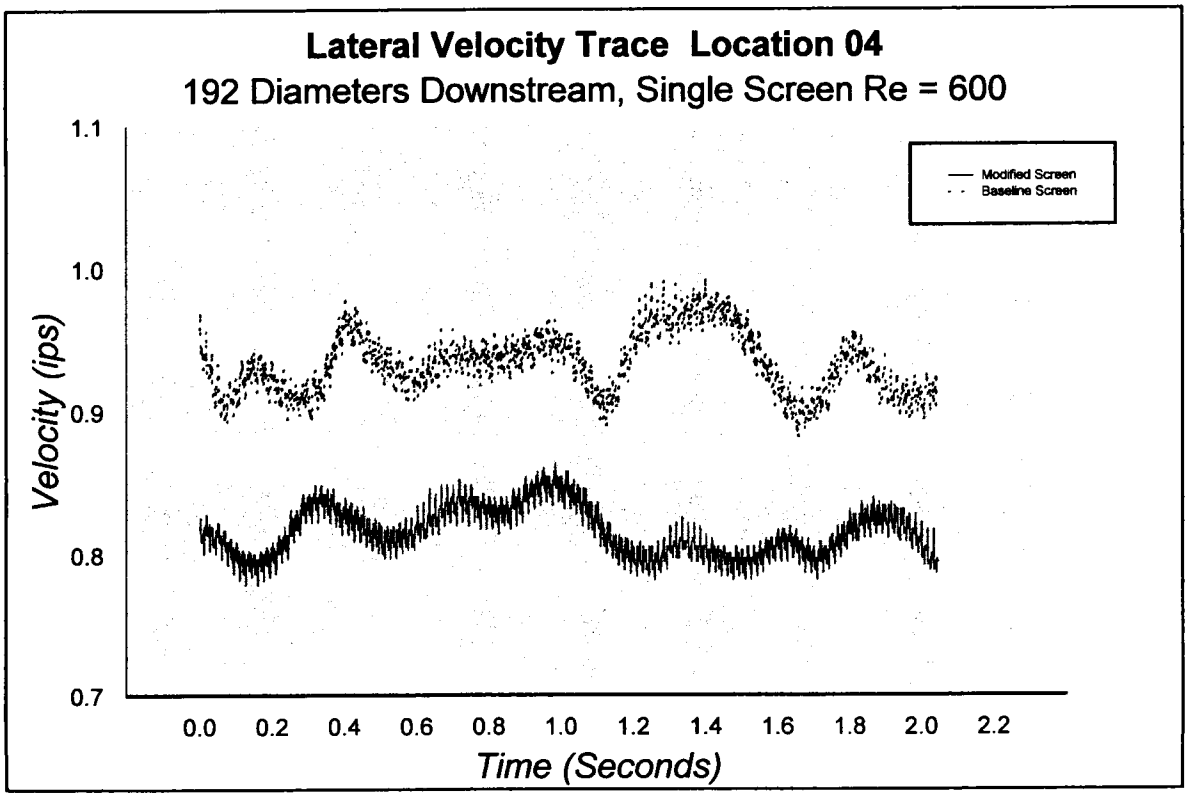
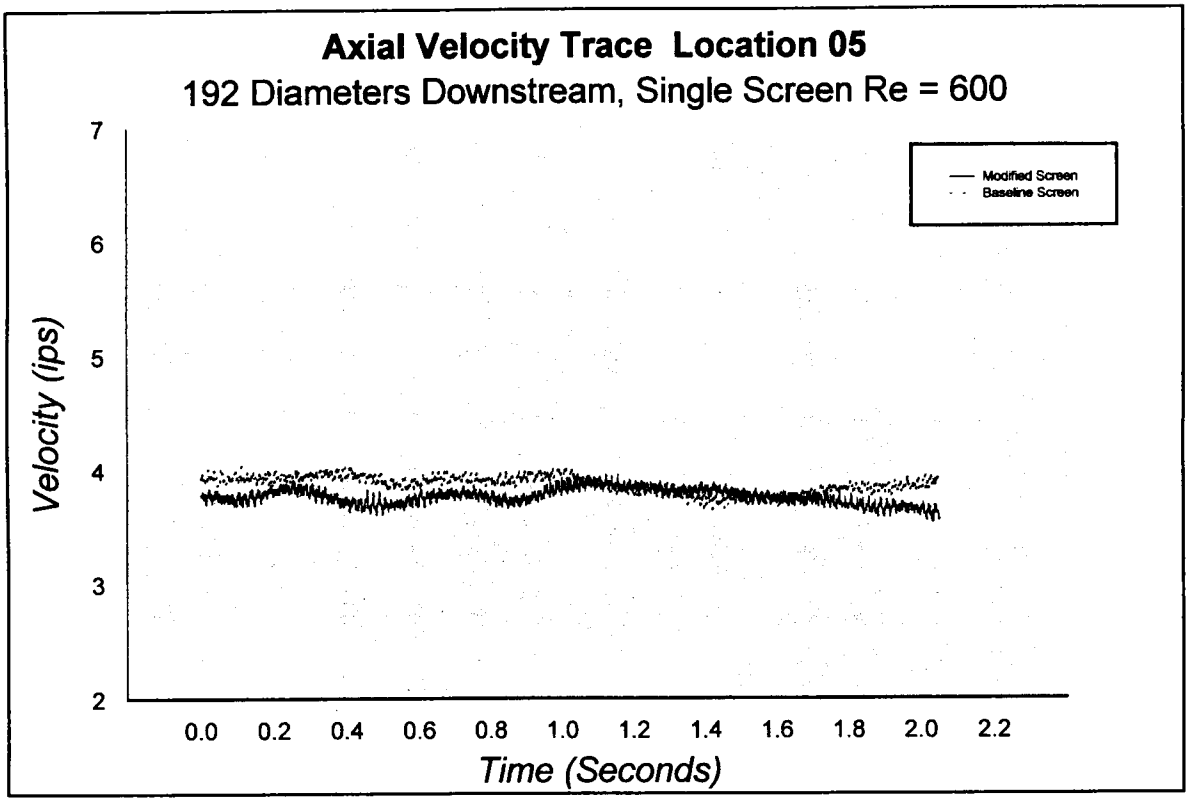


Figure D-29. Single Screen Location 04, 192 Diameters Downsteam

Axial and Lateral Velocity Plots



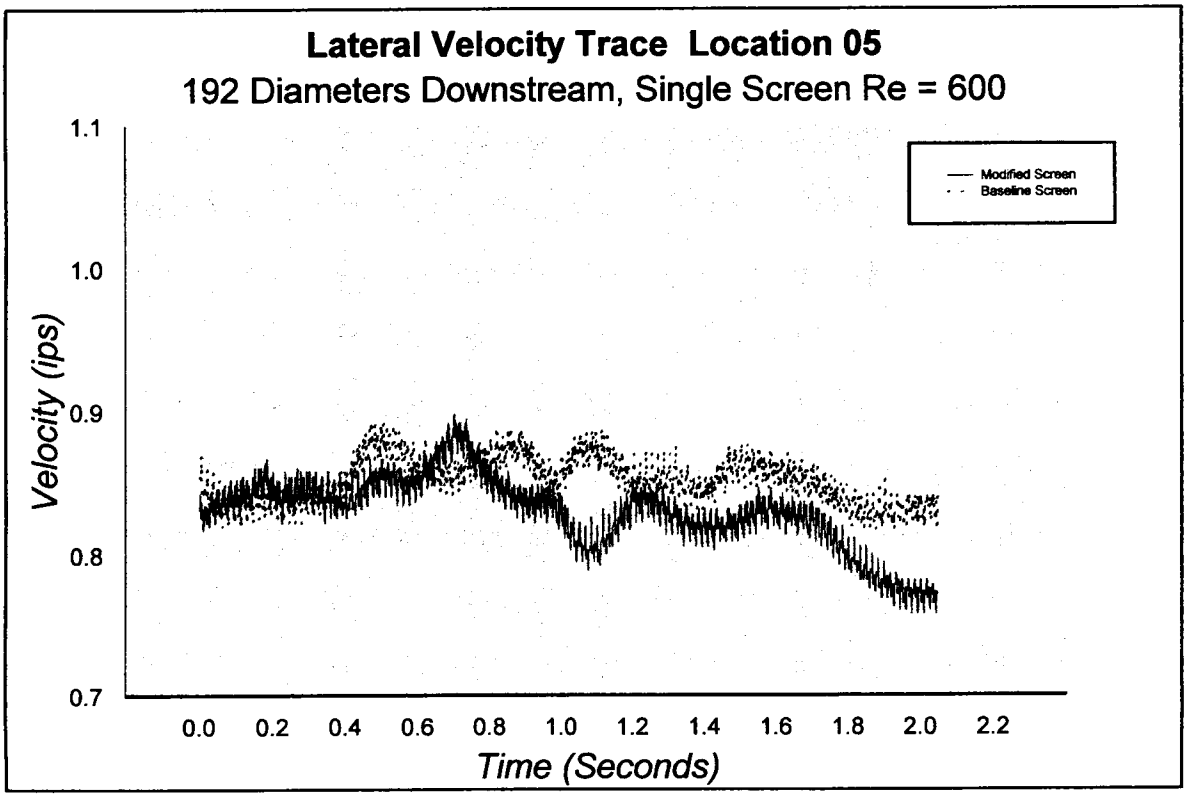


Figure D-30. Single Screen Location 05, 192 Diameters Downsteam

Axial and Lateral Velocity Plots

192 Diameters Downstream, Location 01, Re=600

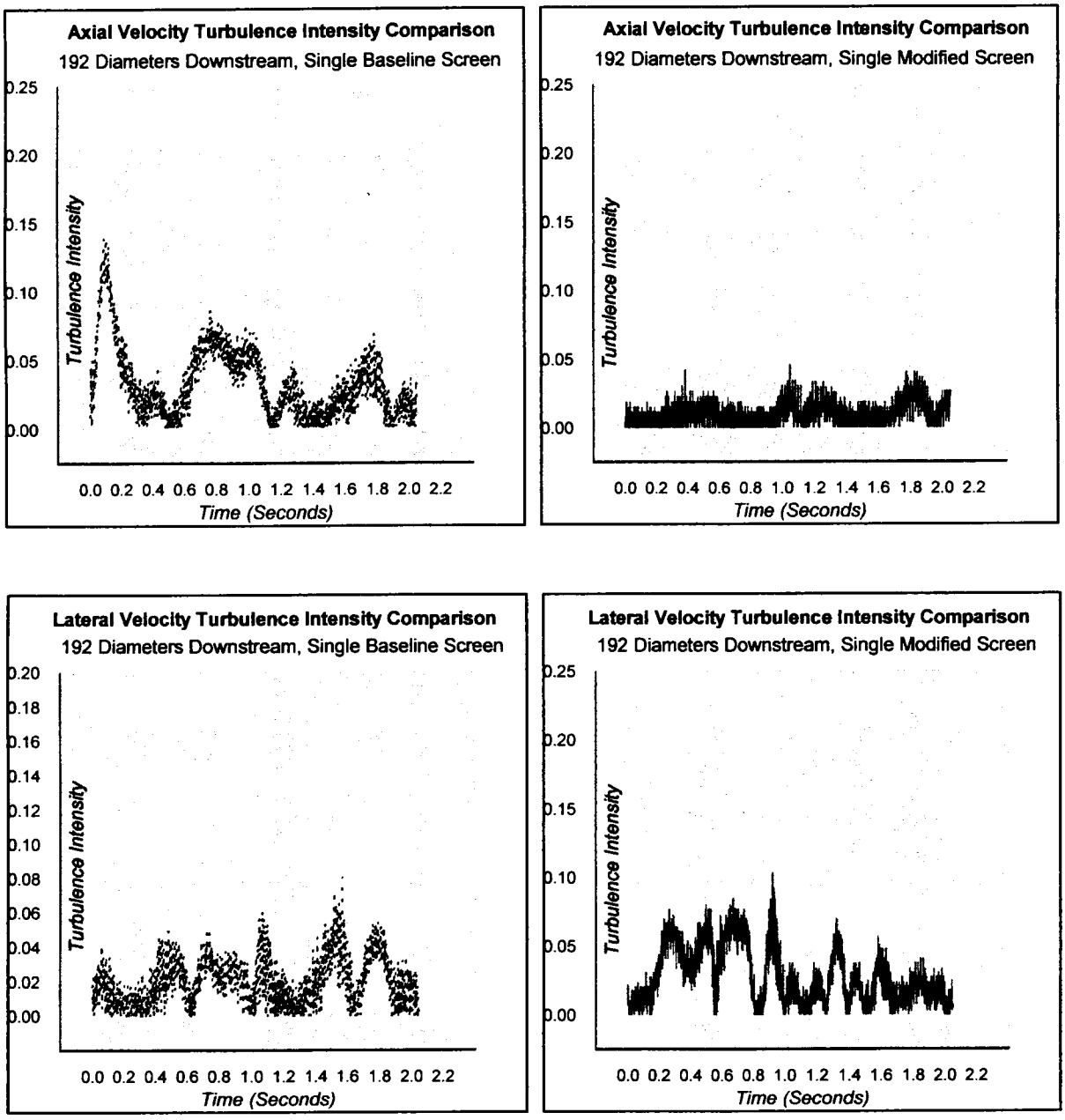


Figure D-31. Single Screen, Location 01, 192 Diameters Downsteam
Axial and Lateral Turbulence Intensity Plots

192 Diameters Downstream, Location 02, Re=600

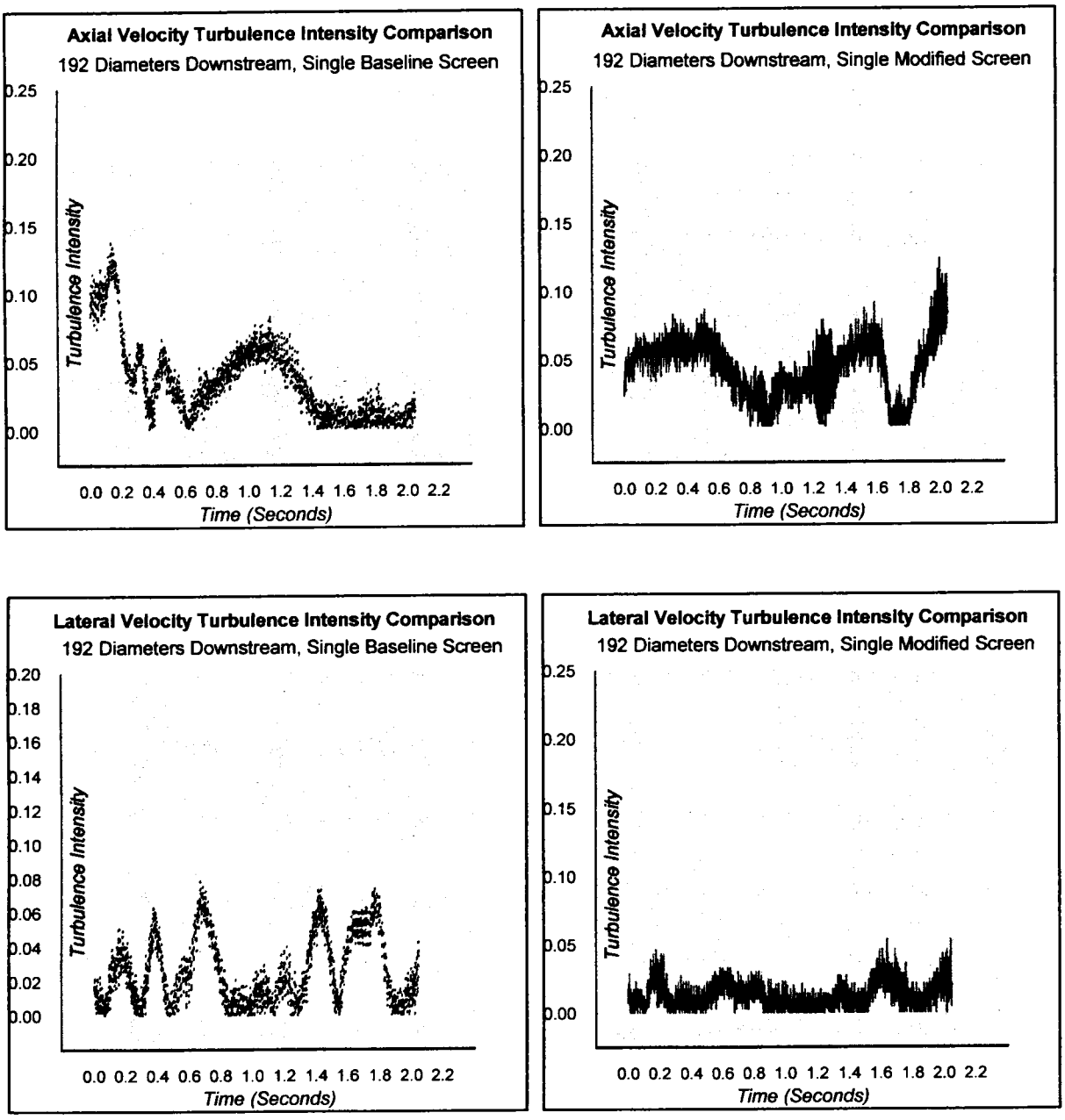


Figure D-32. Single Screen, Location 02, 192 Diameters Downsteam
Axial and Lateral Turbulence Intensity Plots

192 Diameters Downstream, Location 03, Re=600

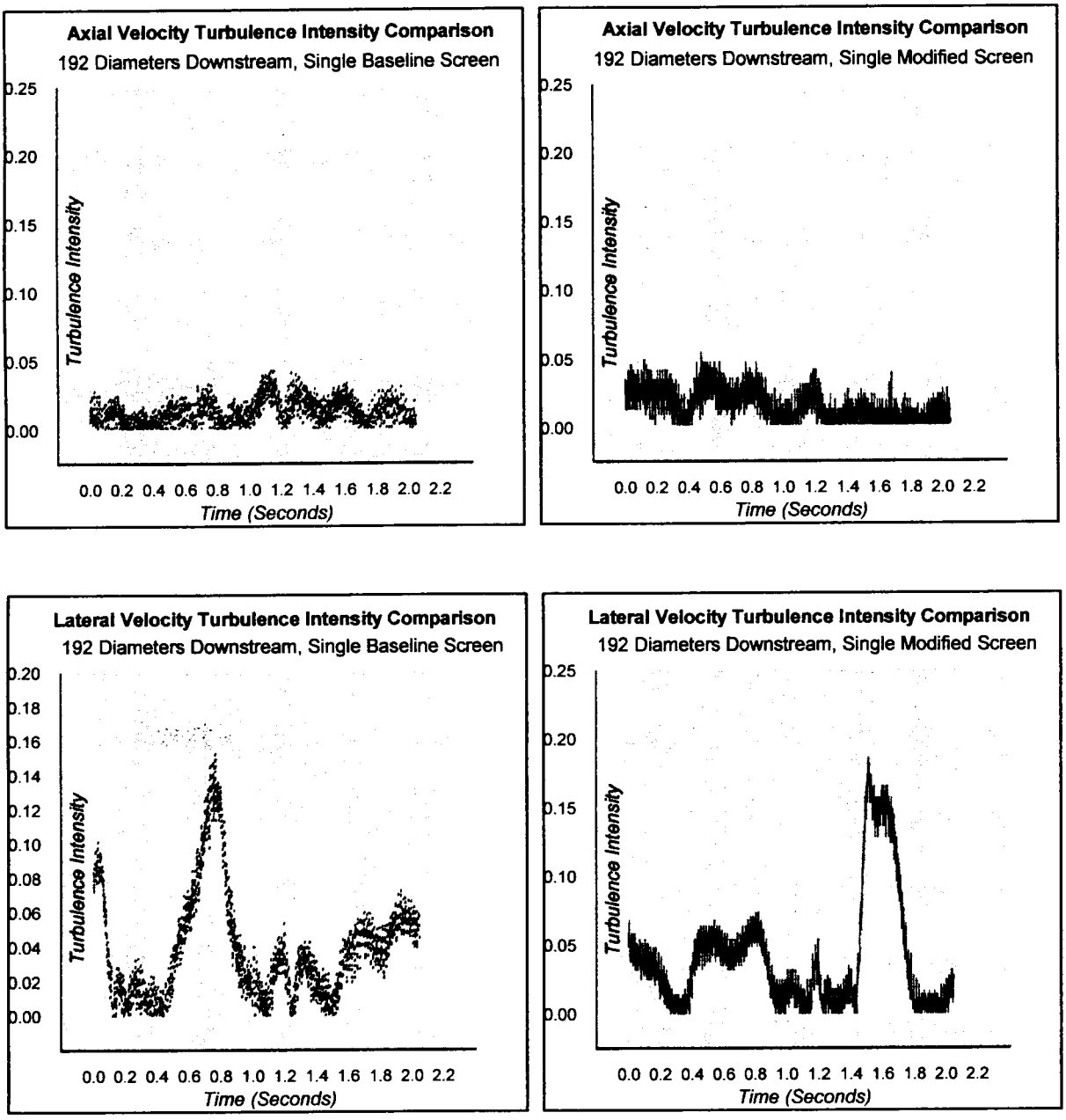


Figure D-33. Single Screen, Location 03, 192 Diameters Downsteam
Axial and Lateral Turbulence Intensity Plots

192 Diameters Downstream, Location 04, Re=600

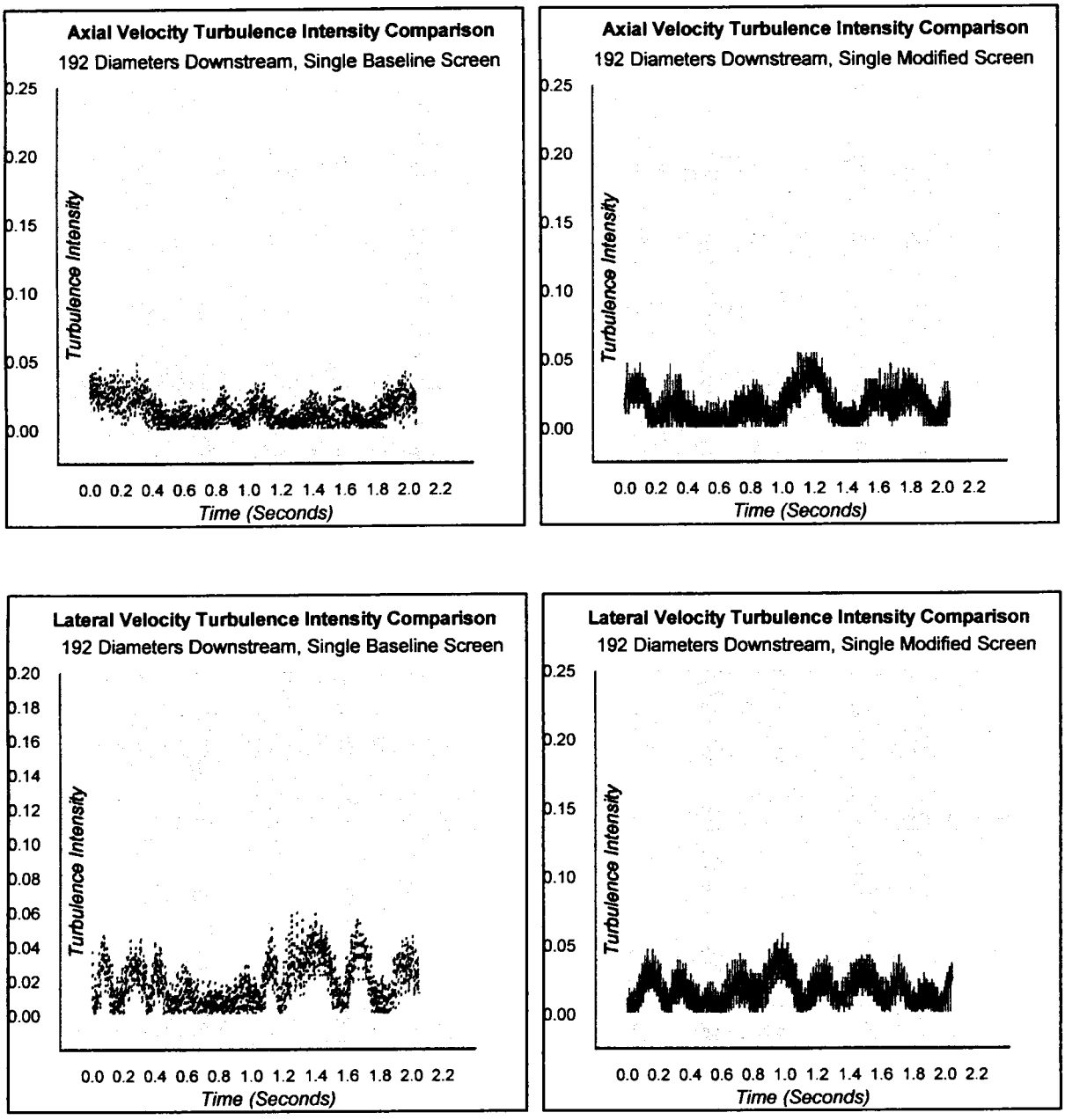


Figure D-34. Single Screen, Location 04, 192 Diameters Downsteam
Axial and Lateral Turbulence Intensity Plots

192 Diameters Downstream, Location 05, Re=600

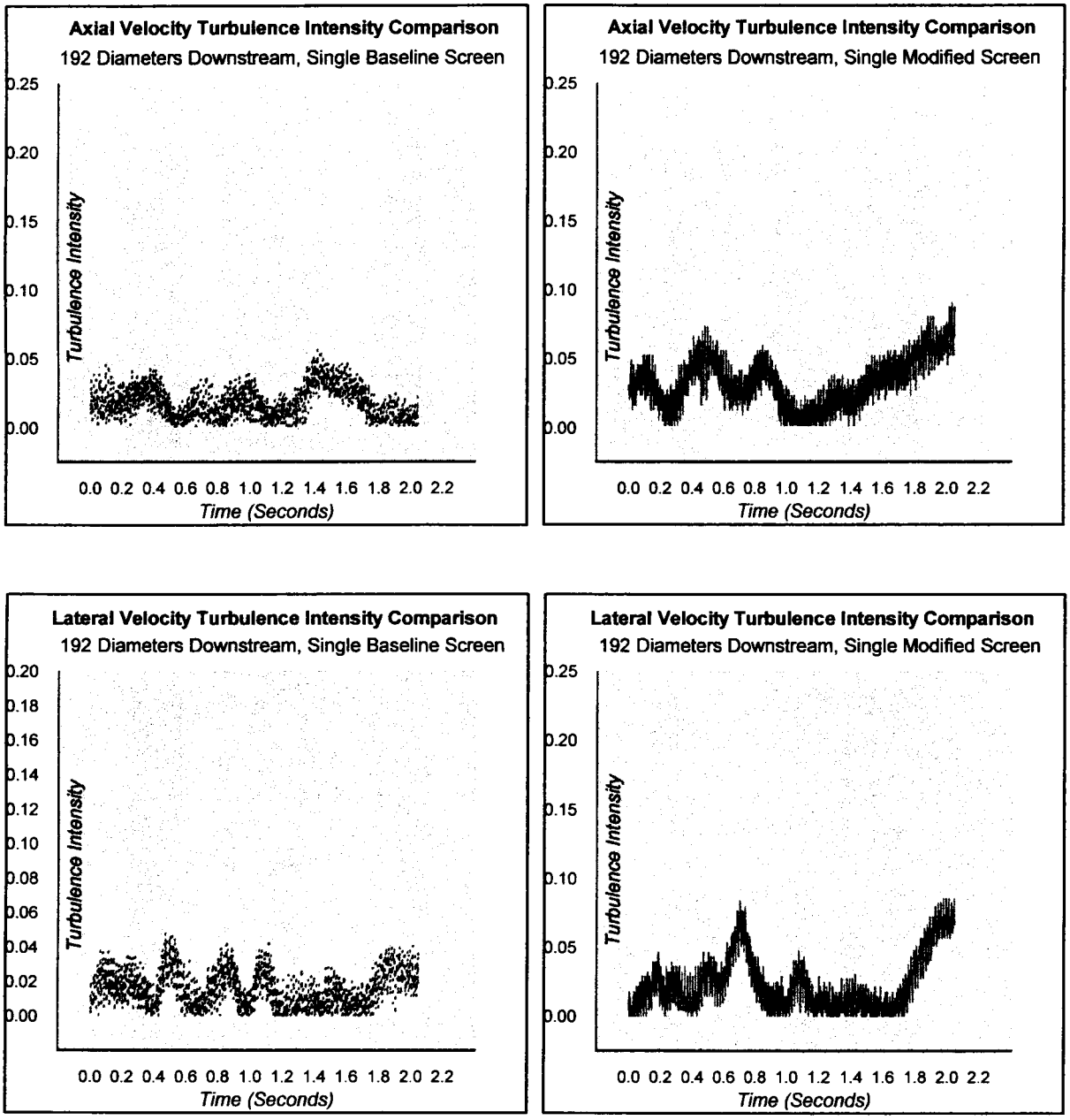


Figure D-35. Single Screen, Location 05, 192 Diameters Downsteam
Axial and Lateral Turbulence Intensity Plots

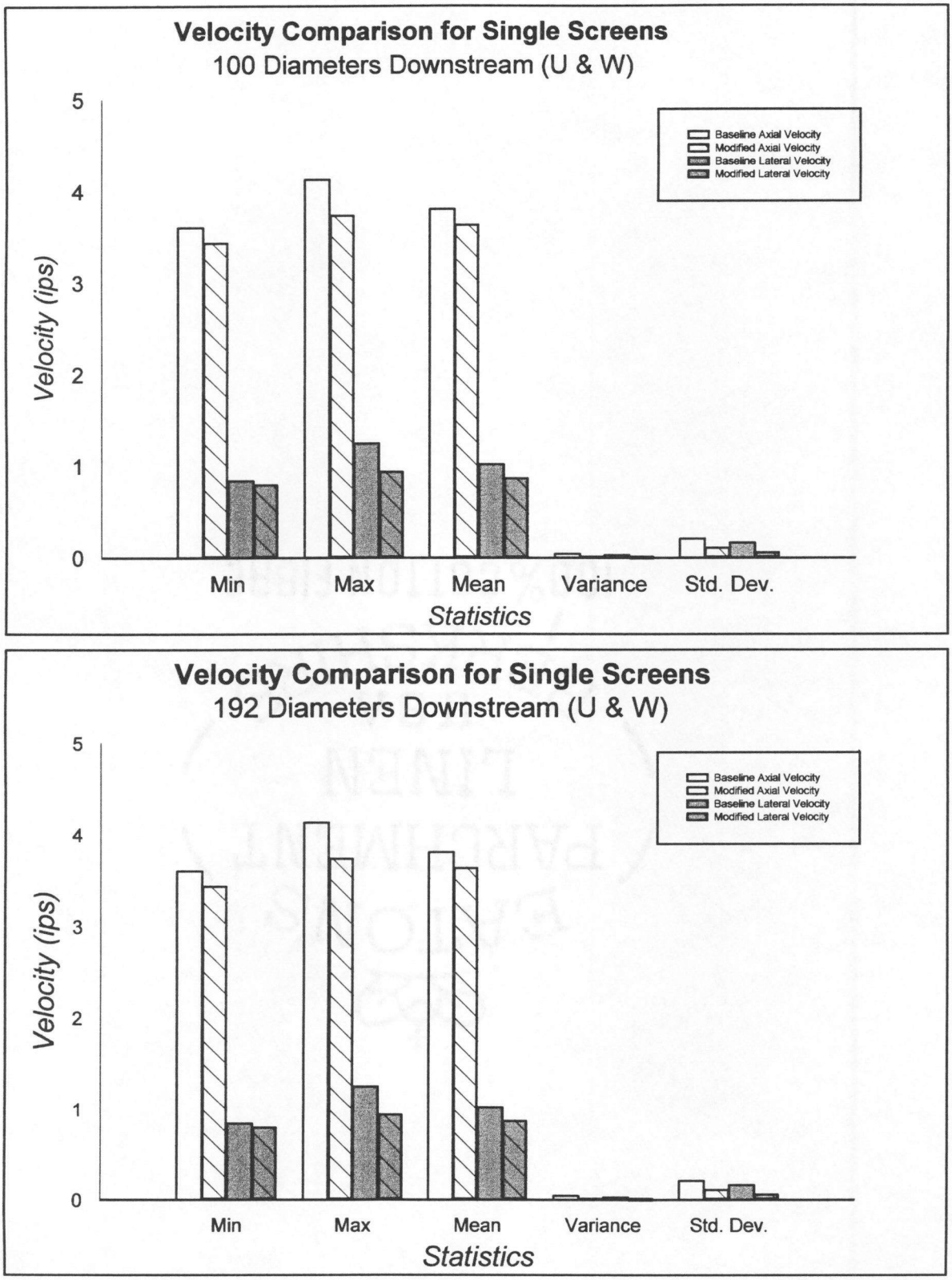


Figure D-36. Single Screen 100 and 192 Diameters Downsteam

Axial and Lateral Velocity Statistics

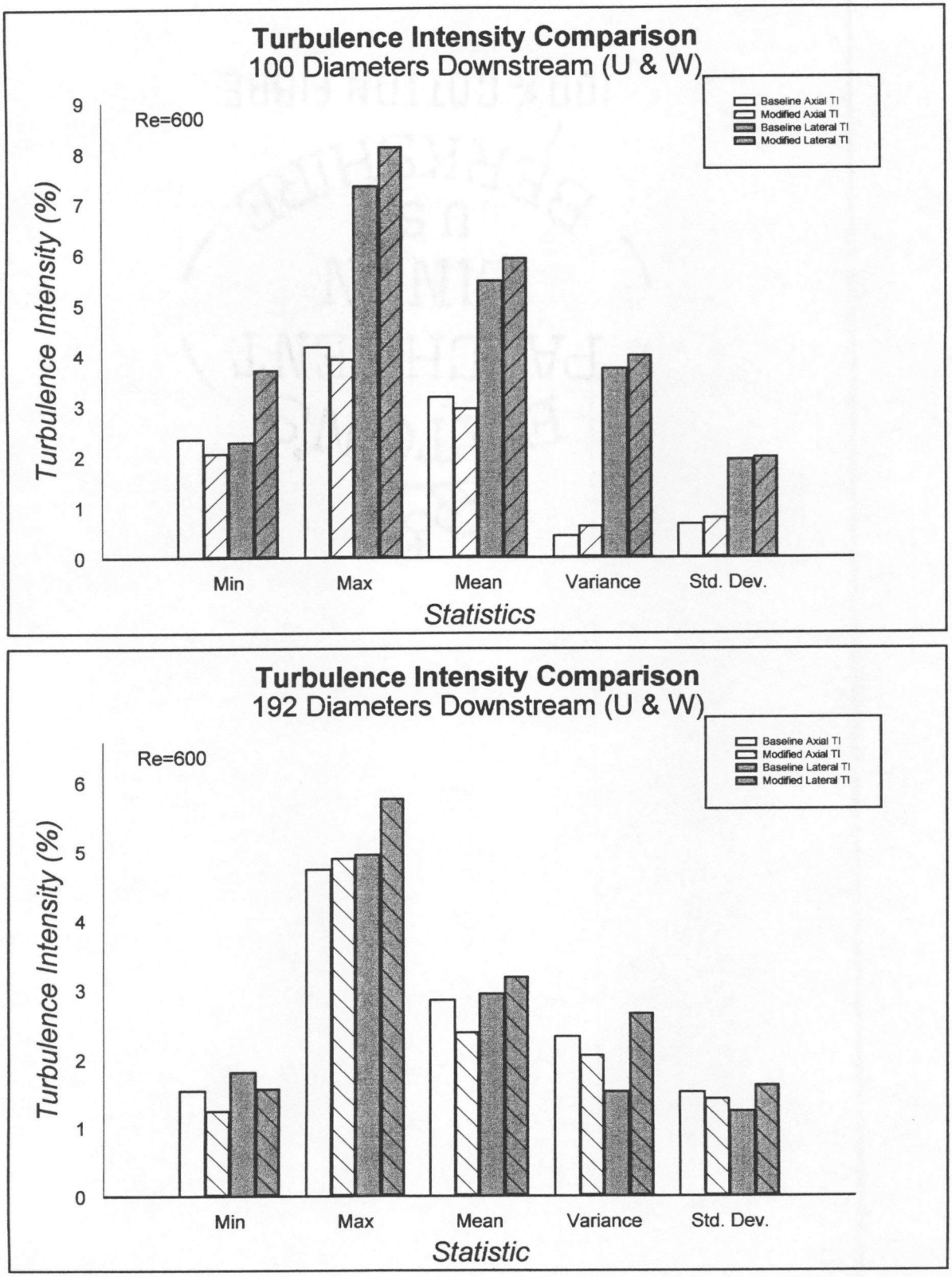


Figure D-37. Single Screen 100 and 192 Diameters Downsteam Axial and Lateral Velocity Turbulence Intensity Statistics

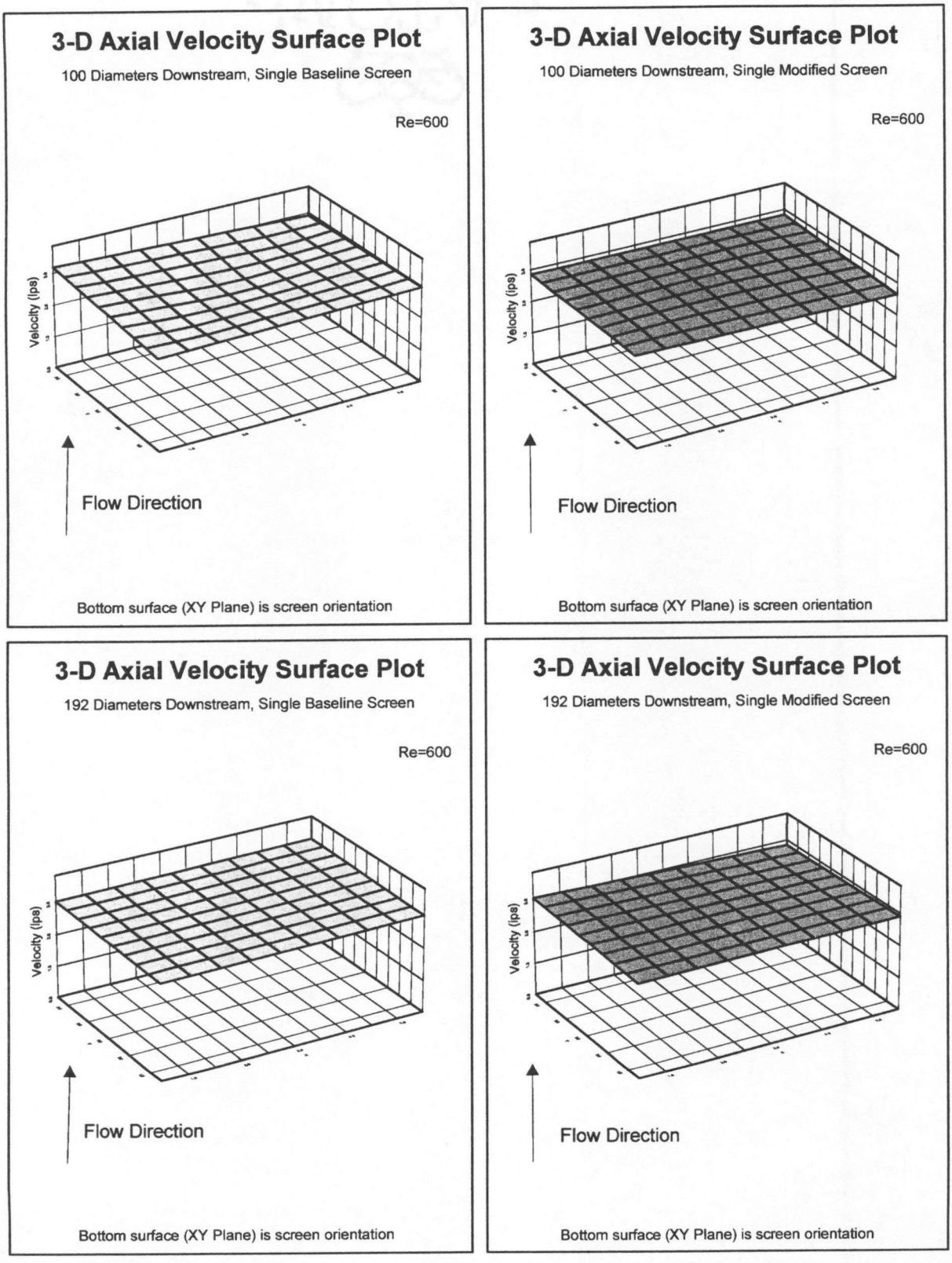


Figure D-38. Single Screen, 100 (top) and 192 (bottom) Diameters Downsteam Axial Velocity Surface Plots

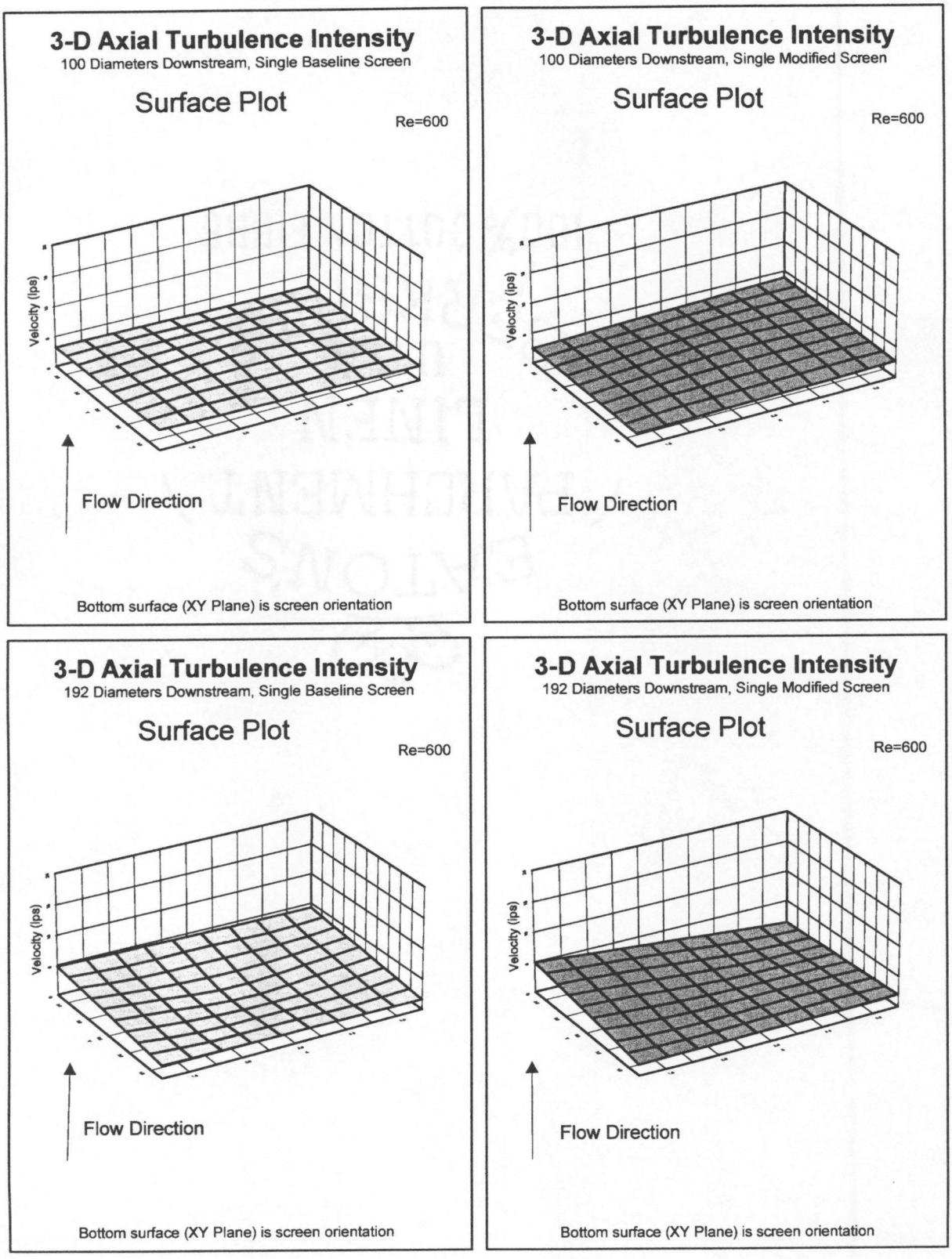


Figure D-39. Single Screen, 100 (top) and 192 (bottom) Diameters Downsteam Axial Velocity Turbulence Intensity Surface Plots

VITA

Bradley James McKeage was born on 10 March, 1962, in Ottawa, Ontario, Canada. As a military dependent, he attended numerous public schools in various geographic locations including Baden-Baden, West Germany, Cold Lake, Alberta, St. Albert Alberta and Ottawa, Ontario. In June 1980, he graduated from Cairine Wilson High School in Orleans, Ontario and then immediately joined the Canadian Armed Forces which had selected him for fully sponsored undergraduate training at the Royal Military College (RMC) of Canada in Kingston Ontario. In May 1984, 2nd Lieutenant McKeage graduated from RMC with a Bachelor's Degree in Mechanical Engineering. After the completion of occupational training as an Aerospace Engineering Officer, Lieutenant McKeage completed a tour as the Project Manager for various Anti-Submarine Warfare Research and Development Projects. Captain McKeage then completed an Operational posting as a Squadron Maintenance Officer with 412 VIP Squadron in Ottawa Ontario. He was then selected to undergo Flight Test Engineering (FTE) training at the USAF Test Pilot School (TPS)at Edwards AFB. In June 1991, he graduated as a Qualified Flight Test Engineer and proceeded to Canada's Aerospace Engineering Test Establishment in Cold Lake, Alberta where he was employed in the Fighter Evaluation Section. He was subsequently selected by the Canadian Armed Forces for post graduate training at UTSI where he completed a Masters of Science degree in Aerospace Engineering in May 1997 and a Masters of Science degree in Aviation Systems in August 1997.